

PONTIFICIA UNIVERSIDAD CATÓLICA DEL PERÚ

FACULTAD DE CIENCIAS E INGENIERÍA



**$^{40}\text{Ar}/^{39}\text{Ar}$ GEOCHRONOLOGY OF THE LITHIUM-RICH TUFF IN THE
MACUSANI VOLCANIC FIELD, ORIENTAL CORDILLERA, PERU**

Tesis para obtener el título profesional de Ingeniera Geóloga

AUTORA:

MERCY KASSANDRA SANANDRES FLORES

ASESOR:

Dr. LISARD TORRÓ I ABAT

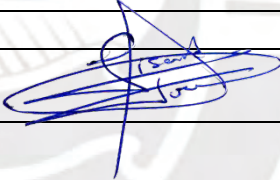
Lima, agosto de 2024

INFORME DE SIMILITUD

Yo, Lisard Torr3 i Abat, docente de la Facultad de Ciencias e Ingenier3a de la Pontificia Universidad Cat3lica del Per3, asesor de la tesis titulada “ $^{40}\text{Ar}/^{39}\text{Ar}$ geochronology of the Lithium-rich Tuff in the Macusani Volcanic Field, Oriental Cordillera, Peru”, de la autora Mercy Kassandra Sanandres Flores, dejo constancia de lo siguiente:

- El mencionado documento tiene un 3ndice de puntuaci3n de similitud de 30 %. As3 lo consigna el reporte de similitud emitido por el software *Turnitin* el 20/08/2024.
- He revisado con detalle dicho reporte y la Tesis y no se advierten indicios de plagio.
- El porcentaje relativamente elevado en el reporte de similitud se debe en gran medida a i) textos en el apartado de metodolog3a, que son est3ndares para metodolog3as espec3ficas y laboratorios anal3ticos concretos y que por lo tanto han sido replicados en multitud de trabajos cient3ficos previos; y ii) la identificaci3n de unidades geol3gicas, incluyendo de manera destacada “Lithium-rich Tuff” y “Macusani Volcanic Field” entre otras, que representan nombres propios que no pueden ser alterados.
- Las citas a otros autores y sus respectivas referencias cumplen escrupulosamente con las pautas acad3micas. No existe ning3n texto ni idea en la tesis que sea derivado de un trabajo previo que no haya sido citado adecuadamente.

Lugar y fecha: Lima a 23 de agosto de 2024

Apellidos y nombre del asesor: Torr3 i Abat, Lisard	
CE: 001833851	Firma 
ORCID: 0000-0002-3557-8334	

RESUMEN

Descubierto en 2017 en el Campo Volcánico Macusani, Puno, SE Perú, el Proyecto de Litio Falchani contiene recursos inferidos e indicados de 5,53 Mt de carbonato de litio equivalentes. El recurso de litio está alojado mayormente en una unidad llamada *Lithium-rich Tuff*. Esta unidad comprende principalmente lodolitas tufáceas y ha sido correlacionada estratigráficamente con la Formación Macusani, depositada entre ca. 10 y 6.5 Ma. En esta tesis presento las primeras dataciones radiométricas en *Lithium-rich Tuff* y tobas brechificadas coespaciales para evaluar su adscripción estratigráfica y contextualización de este evento magmático dentro de la evolución Neógena de los Andes Centrales. Las edades, obtenidas mediante el método $^{40}\text{Ar}/^{39}\text{Ar}$ en cristaloclastos de mica, están comprendidas entre 8.978 ± 73 ka y 8.717 ± 44 ka. Las muestras de toba brechificada arrojaron edades comprendidas en un estrecho rango entre 8.823 ± 9 ka y 8.815 ± 16 ka, que se encuentra dentro del intervalo de edad definido por las muestras de *Lithium-rich Tuff*. Las edades obtenidas representan edades de cristalización o enfriamiento de las micas y reflejan edades máximas de sedimentación. De acuerdo a estos datos, los cristaloclastos de mica se formaron o fueron expulsados durante un breve periodo de ca. 261 kyr (entre 144 kyr y 379 kyr considerando errores analíticos). Las edades obtenidas coinciden con el lapso de tiempo comprendido entre los dos ciclos eruptivos a 10 ± 1 Ma y 7 ± 1 Ma registrados para la Formación Macusani. En base a una exhaustiva recopilación de dataciones geocronológicas previas en la Cordillera Oriental de los Andes en el SE de Perú se demuestra que no existen unidades intrusivas, volcánicas o volcanoclásticas de edad equivalente. Por lo tanto, se concluye que el evento asociado a la formación o enfriamiento de las micas en la *Lithium-rich Tuff* ocurrió durante un periodo de muy baja o nula actividad magmática en la región.

ABSTRACT

The Falchani Lithium Project was discovered in 2017 in the Macusani Volcanic Field, Puno, SE Peru. The inferred and indicated resources of the project total 5.53 Mt of lithium carbonate equivalent. The lithium resource is hosted mostly in a unit called Lithium-rich Tuff. This unit is composed primarily of tuffaceous mudstone and has been stratigraphically correlated with the Macusani Formation, which was deposited between ca. 10 and 6.5 Ma. In this thesis, I present the first radiometric dating on Lithium-rich Tuff and cospatial brecciated tuff to evaluate their stratigraphic ascription and the contextualization of the associated magmatic event within the Neogene evolution of the Central Andes. The dates obtained by the $^{40}\text{Ar}/^{39}\text{Ar}$ method on mica crystal clasts in Lithium-rich Tuff range from $8,979 \pm 73$ ka to $8,717 \pm 44$ ka. The brecciated tuff samples yielded dates within a narrow range between $8,823 \pm 9$ ka and $8,815 \pm 16$ ka, which is within the age interval defined by the Lithium-rich Tuff samples. The dates obtained represent crystallization or cooling ages of the micas and reflect maximum sedimentation ages. The data indicate that the mica crystal clasts formed or were ejected during a relatively brief period of ca. 261 kyr (between 144 kyr and 379 kyr, considering analytical errors). The obtained dates align with the temporal span between the two eruptive cycles at 10 ± 1 Ma and 7 ± 1 Ma recorded by the Macusani Formation. A comprehensive review of previous geochronological studies in the Eastern Cordillera of the Andes in southeastern Peru reveals the absence of intrusive, volcanic, or volcanoclastic units of comparable age. This suggests that the event related to the formation or cooling of the mica crystal clasts in the Lithium-rich Tuff occurred during a period of very low or nil magmatic activity in the region.

Acknowledgments

I would like to express my gratitude to God for granting me patience and wisdom throughout my academic and professional journey.

I am also grateful to my parents and family for their unwavering support and hard work. Additionally, I would like to thank Lisard for entrusting me with this project, for his patience and for being an exceptional human being and professional.

I would like to acknowledge Dr. Silvia Rosas for her guidance and teaching, which have been instrumental in shaping me into the professional I am today.

I am also grateful to my classmates, now colleagues, with whom I shared many hours of study and company at the Pontificia Universidad Católica del Perú.

I extend my greetings to:

Johan Ramírez for insightful discussion about the geology of the Eastern Cordillera; Mariana Segovia More for being an excellent partner in this research;

Jean Vallance and Patrice Baby for their participation in the field campaign in the Macusani area during which the rocks studied in this thesis were sampled;

Jean Vallance and Cesar Muñoz, members of the dissertation panel, for the detailed and constructive comments;

Macusani Yellowcake – American Lithium, Dr. Ulises Solís and geologists Gabriel Tasayco, Miguel Cavani, Roher Huaricallo, and Henry Mamani for continued support to develop this research; and

Kathleen Zanetti (Nevada Isotope Geochronology Laboratory, University of Nevada, Las Vegas) for the excellent $^{40}\text{Ar}/^{39}\text{Ar}$ dates she provided.

This study was economically supported by the Peruvian PROCIENCIA-FONDECYT project 122-2020 E041-2020-01-01.

Table of contents

1. INTRODUCTION	1
1.1. K-Ar geochronology: the $^{40}\text{Ar}/^{39}\text{Ar}$ method	1
1.2. Previous radiometric dating in the Macusani Structural Zone.....	6
1.3. The discovery of the Falchani deposit	21
1.4. Conundrum	24
1.5. Objectives	24
1.6. Hypothesis.....	25
1.7. Justification.....	25
2. METHODOLOGY	26
2.1. Sampling	26
2.2. $^{40}\text{Ar}/^{39}\text{Ar}$ geochronology.....	28
3. GEOLOGICAL SETTING	29
3.1. Geology of the Central Andes in southern Peru: The Oriental Cordillera.....	29
3.2. Regional geology of the Macusani Structural Zone and Cordillera de Carabaya....	33
3.3. Geology of the Macusani Volcanic Field	37
4. RESULTS	44
4.1. Textural description of the dated rock samples	44
4.2. $^{40}\text{Ar}/^{39}\text{Ar}$ results	46
5. DISCUSSION.....	52
5.1. Deposition duration and rate of the Lithium-rich Tuff.....	52
5.2. Stratigraphic and tectono-magmatic contextualization of the Lithium-rich Tuff....	54
7. REFERENCES	58

List of figures

- Figure 1.** Ar-Ar step heating profiles. (a) A ‘plateau age’ indicates a uniform age and that the sample remained a closed system. (b) Ar loss grain boundaries indicates ‘young ages’ in lower temperatures and a ‘plateau age’ in the center of the grain, where there was no Ar loss. (c) Different events of Ar loss recording an ancient Ar loss and an ‘original age’ in the center grain (modified from Schaefer 2016).....4
- Figure 2.** Inverse Isochron diagram for Ar isotopes. The age of the sample is calculated from the $^{39}\text{Ar}/^{40}\text{Ar}$ value at the intercept with the x-axis (modified from Schaefer 2016).....5
- Figure 3.** Simplified geological map of the Macusani Structural Zone and contiguous morphostructural domains adapted from 50k sheets of INGEMMET (2023). The location of the map within the Peruvian territory is shown in the top-right inset. The dashed black lines indicate the locations of the geological maps showing compiled geochronological data in Figures 4 to 8. Age brackets for intrusive rocks are based on Clark et al. (1983), Kontak (1984), Bonhomme et al. (1985a, b, 1988), Kontak et al. (1986, 1987, 1990a, b), Laubacher et al. (1988), Pichavant et al. (1988), Cheilletz et al. (1992), Sandeman et al. (1997), Mišković et al. (2009), Spikings et al. (2016), and Harlaux et al (2021, 2023). Morphostructural provinces in upper-right inset are after Benavides-Cáceres (1999). Key: Western Cordillera (WC); Eastern Cordillera (EC); Sub-Andean Zone (SAZ).....8
- Figure 4.** Simplified geological map with previous radiometric dates on intrusive (white boxes) and volcanic (yellow boxes) rocks (see location of the area in Fig. 3). Geological mapping at 50k scale from INGEMMET (2023). Color code of the geological map as in Figure 3.9
- Figure 5.** Simplified geological map with previous radiometric dates on intrusive rocks (see location of the area in Fig. 3). Geological mapping at 50k scale was extracted from INGEMMET (2023). Color code of the geological map as in Figure 3.10
- Figure 6.** Simplified geological map with previous radiometric dates on volcanic rocks (see location of the area in Fig. 3). Geological mapping at 50k scale was extracted from INGEMMET (2023). Color code of the geological map as in Figure 3.11
- Figure 7.** Simplified geological map with previous radiometric dates on plutonic (white boxes) and volcanic (yellow boxes) rocks (see location of the area in Fig. 3). Geological mapping at 50k scale from INGEMMET (2023). Color code of the geological map as in Figure 3.14
- Figure 8.** Generalized stratigraphic column traced across the Macusani Structural Zone and contiguous morphotectonic provinces including previous radiometric dating of plutonic rocks. Labels on geochronological data refer to the name of dated samples in the respective original articles. The temporary extension of the Famatinian, Gondwanide, and Andean orogenic cycles in the Central Andes has been delimited after Laubacher (1978), López-Gamundí and Rosello (1993), Chew et al. (2016), and Carrillo et al. (2021). The ages of the stratigraphic units are after Laubacher (1978), Cheilletz et al. (1992), Sandeman et al. (1997), Spikings et al. (2016), and Rodríguez et al. (2021). References for compiled radiometric dates: (1) Evernden and Kistler (1970), (2) Stewart et al. (1974), (3) Lancelot et al. (1978), (4) Clark et al. (1983), (5) Kontak (1984), (6) Bonhomme et al. (1985b), (7) Kontak et al. (1986), (8) Kontak et al. (1987), (9) Kontak et al. (1990a), (10) Kontak et al. (1990b), (11) Cheilletz et al. (1992), (12) Sandeman et al. (1997), (13) Mišković et al. (2009), (14) Spikings et al. (2016), (15) Harlaux et al. (2021), and (16) Harlaux et al. (2023).19
- Figure 9.** Generalized stratigraphic column traced across the Macusani Structural Zone and contiguous morphotectonic provinces including previous radiometric dating of volcanic rocks. The labels on geochronological data refer to the name used for dated samples in the respective original articles. Stratigraphic units according to Sandeman et al. (1997). The references for compiled radiometric dates are provided in the figure.20

Figure 10. Location of the Falchani and Ocasasa 4 concessions (Falchani Lithium Project) and other concessions owned by Macusani Yellowcake S.A.C. and other companies and individuals in the Macusani Volcanic Field. Delimitation of exploration concessions according to SIDEMCAT (2024).....	22
Figure 11. Location of samples selected for $^{40}\text{Ar}/^{39}\text{Ar}$ dating in the Macusani Volcanic Field. Delimitation of exploration concessions according to SIDEMCAT (2024).....	27
Figure 12. Morphotectonics units of the Central Andes across Peru after Wörner et al. (2018) and geological cross-section of the Andes at 20°S after Baby et al. (1997) and Rochat et al. (1998).....	31
Figure 13. Volcano-stratigraphic correlation chart and $^{40}\text{Ar}/^{39}\text{Ar}$ dates on Macusani Volcanics (Francis, 1959) (equivalent to the later defined Macusani Formation) in Chapi, Chilcuno North, Huiquiza, and Orcoyo sections. Modified from Cheilletz et al. (1992).....	39
Figure 14. Schematic stratigraphic columns of Neogene volcanic and sedimentary rocks in the Macusani Volcanic Field according to descriptions of Sandeman et al. (1997), Cheilletz et al. (1992), López (1996), and Li (2016).	42
Figure 15. Dated samples of Lithium-rich Tuff (a-e) and brecciated tuff (f-h) from the Falchani Lithium Project and of white tuff from the former San Vicente White concession (i) in the Macusani Volcanic Field.	45
Figure 16. $^{40}\text{Ar}/^{39}\text{Ar}$ step heating profiles and inverse isochron diagrams for Lithium-rich Tuff samples from the Macusani Volcanic Field.....	48
Figure 17. $^{40}\text{Ar}/^{39}\text{Ar}$ step heating profiles and inverse isochron diagrams for brecciated tuff samples from the Macusani Volcanic Field.....	50
Figure 18. $^{40}\text{Ar}/^{39}\text{Ar}$ step heating profile and inverse isochron diagram for the white tuff from the former San Vicente White concession in the Macusani Volcanic Field.....	51
Figure 19. Geochronological chart of $^{40}\text{Ar}/^{39}\text{Ar}$ plateau dates on mica separates from the Macusani Volcanic Field analyzed in this thesis sorted according to their sampling elevation.	51
Figure 20. Stratigraphic and geochronological relationships of the volcanic and intrusive rocks in the Quenamari, Antauta, Cayconi, and Picotani fields (modified from Sandeman et al. 1997). The Lithium-rich Tuff has been included in the Macusani Volcanic Field, according to the new dates of 8.8-8.7 Ma.....	55
Figure 21. Geochronologic chart of Cenozoic rocks in the Macusani Structural Zone and Cordillera de Carabaya, including the new $^{40}\text{Ar}/^{39}\text{Ar}$ mica dates on Lithium-rich Tuff from the Falchani Lithium Project in the Macusani Volcanic Field.	56
Figure 22. Location of the dated samples of Lithium-rich Tuff and brecciated tuff (this study) and other samples dated by previous authors in the Macusani Volcanic Field. White boxes contain dates on intrusive rocks, and yellow boxes, on volcanic rocks.....	57

List of tables

Table 1. Mineral resources estimate for the Falchani Project in October 2023.	23
Table 2. $^{40}\text{Ar}/^{39}\text{Ar}$ analytical data for micas separate on Lithium-rich Tuffs, Macusani Volcanic Field, Oriental Cordillera, Peru	47



1. INTRODUCTION

1.1. K-Ar geochronology: the $^{40}\text{Ar}/^{39}\text{Ar}$ method

Geochronology is the discipline responsible to quantitatively measure the age of earth materials, the Earth, the Sun, and the Solar System, as well as providing the temporal framework of geological events (e.g., formation of mineral systems; see Stein 2014), and tracing the origins of the civilization, the species, and life (White 2015; Schaefer 2016). Rutherford and Soddy (1903) introduced the concept of radiometric dating, which is based on the process of radioactive decay of radioactive to radiogenic isotopes. They showed that the process of radioactive decay is exponential and independent of chemical or physical condition such as pressure and temperature. Thus, the speed of radioactive decay is constant since it depends only on the stability of the radioactive nucleus, hence the use of radioactive decay systems to measuring geological time (Jäger 1979; Rollinson 1993). The radioactive decay velocity of a particular isotope is described by the decay constant (λ), which is the probability that a single atom will disintegrate in a given unit of time. The decay constant is correlated with the half-life ($T_{1/2}$), which is the period of time that it will take for half of a mass of radioactive material to decay away (Jäger 1979; Schaefer 2016). The half-life is linked to the decay constant as shown in Eq. 1. Also important is the concept of closure temperature (T_c), which is defined as the temperature at which a mineral begins to accumulate radiogenic isotopes, and therefore, the geochronological clock begins to tick (Schaefer 2016). Above this temperature no age information is preserved since the radiogenic isotope is able to diffuse out the mineral structure (Schaefer 2016).

$$T_{1/2} = \frac{\ln 2}{\lambda} \quad (\text{Eq. 1})$$

The K-Ar system is one of the first dating methods used in geochronology (Reiners et al. 2017). In the following lines, details on the K-Ar system and its application for geochronological purposes will be mostly based on Lee (2015), Schaefer (2016), and Reiners et al. (2017).

Potassium has three natural isotopes with the following natural abundances: ^{39}K (93.2581 %), ^{40}K (0.0117 %), and ^{41}K (6.7302 %). Of these three, only ^{40}K is radioactive with a half-life of 1.248×10^9 years. The decay of ^{40}K is through a branched scheme to radiogenic ^{40}Ca (by β^- emission; 89.1 % of the ^{40}K decay events) and ^{40}Ar (by electron capture with a contribution from β^+ decay; 10.9 % of the ^{40}K decay events). K-Ar dating in particular is based on the natural decay of the ^{40}K radioactive isotope to the stable daughter isotope ^{40}Ar . The age of a sample (t) can be calculated following Eq. 2.

$$t = \frac{1}{\lambda} \ln \left[\frac{{}^{40}\text{Ar}^*}{{}^{40}\text{K}} \left(\frac{\lambda}{\lambda_e} \right) + 1 \right] \quad (\text{Eq 2.})$$

where λ is the total decay constant for ^{40}K ($5.549 \times 10^{-10} \text{ yr}^{-1}$) and λ_e is the decay constant specific to the production of $^{40}\text{Ar}^*$ ($0.575 \times 10^{-10} \text{ yr}^{-1}$). Note that the asterisk in $^{40}\text{Ar}^*$ is used to denote only radiogenic ^{40}Ar (i.e., derived from the radioactive decay of ^{40}K in the same sample), as there are other sources of ^{40}Ar such as the atmosphere or excess Ar from the Earth's crust or mantle, often denoted as $^{40}\text{Ar}_a$ and $^{40}\text{Ar}_E$, respectively.

This method relies on two key assumptions: i) that all ^{40}Ar measured within a mineral is produced by radioactive decay of ^{40}K , and ii) that the sample remained a closed system. The first assumption is often not fulfilled due to the contamination of samples with ^{40}Ar from xenolithic material entrained during magmatism, atmospheric contamination, or incomplete degassing of magmas. The second assumption is also commonly violated due to the fact that

$^{40}\text{Ar}^*$ is prone to migration by diffusion when it is subjected to temperature changes causing Ar loss or resetting of the system. Because of the unlikelihood in the fulfillment of both assumptions, the K-Ar dating method has been overcome by the $^{40}\text{Ar}/^{39}\text{Ar}$ dating method.

The $^{40}\text{Ar}/^{39}\text{Ar}$ dating method is a variant of the K-Ar method whereby a parent isotope (^{39}K) is converted to a daughter isotope (^{39}Ar) through neutron irradiation in a nuclear reactor following the $^{39}\text{K} + \text{n} \rightarrow ^{39}\text{Ar} + \text{p}$ scheme. ^{39}Ar has a half-life of only 269 years and does not occur naturally. Such conversion allows the measurement of both parent (though by proxy) and daughter isotopes as well as the analysis of all three Ar isotopes (^{40}Ar , ^{39}Ar , and ^{36}Ar) simultaneously. An atmospheric correction must be made to subtract the $^{40}\text{Ar}_a$ (atmospheric component) from the total amount of ^{40}Ar measured. To carry out this correction, it is necessary to use the ^{36}Ar isotope, which is measured in the mass spectrometer and assumed to be either atmospheric contamination or inherited from the sample. Since the atmospheric ratio ($^{40}\text{Ar}/^{36}\text{Ar}$)_a is 295.5, thus the atmospheric component can be calculated as $^{40}\text{Ar}_a = 295.5 \times ^{36}\text{Ar}$. Therefore, with the amount of $^{40}\text{Ar}_a$ calculated, it is possible to give only the radiogenic component ($^{40}\text{Ar}^*$). Consequently, from the measured concentrations, the atmospheric correction made, and assuming a neutron fluence of the irradiation ($J = 5.549 \times 10^{-10} \text{ yr}^{-1}$), the age of a sample (t) can be calculated directly following Eq. 3.

$$t = \frac{1}{\lambda} \ln \left[\frac{^{40}\text{Ar}^*}{^{39}\text{Ar}} J + 1 \right] \quad (\text{Eq. 3})$$

The method $^{40}\text{Ar}/^{39}\text{Ar}$ enables to release argon incrementally from a sample of interest by heating in steps of increasing temperature. The argon released in each heating step is then isotopically analyzed in order to calculate a date. Heating of samples may be carried out by furnaces based on electrical resistance or radiofrequency induction, or by continuous wave lasers.

The incremental heating or step heating data are depicted by the age spectrum (Fig. 1). There are different interpretation cases. In the simplest case, uniform $^{40}\text{Ar}/^{39}\text{Ar}$ ratios within the region of the mineral grain(s) sampled by heating steps will return a ‘plateau age’, which indicates a uniform age irrespective of the temperature at which the Ar was released (Fig. 1a). If a mineral has undergone Ar loss from the grain boundaries due to reheating or slow regional cooling, the $^{40}\text{Ar}/^{39}\text{Ar}$ ratios of Ar liberated at lower temperatures will be spurious whereas the $^{40}\text{Ar}/^{39}\text{Ar}$ ratios of Ar liberated at higher temperatures (i.e., Ar liberated from the center of the grain) will become more consistent, eventually reaching a plateau (Fig. 1b). In special cases, a first small plateau may indicate closed system behavior and subsequent re-accumulation of radiogenic Ar after the diffusive loss (Fig. 1c).

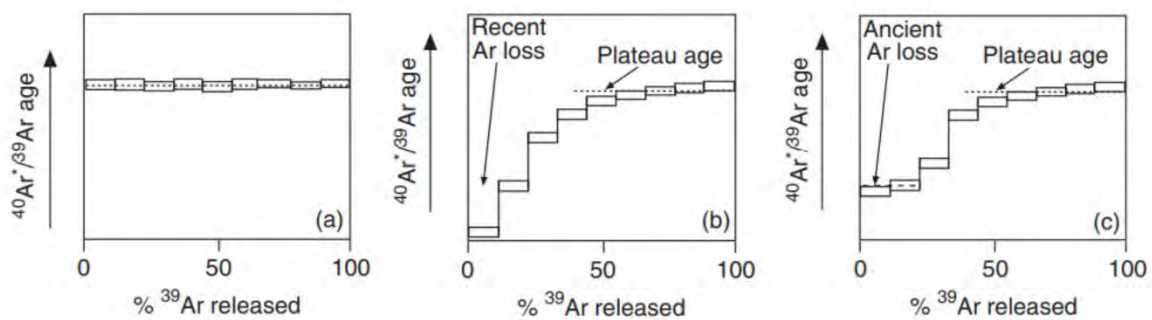


Figure 1. Ar-Ar step heating profiles. (a) A ‘plateau age’ indicates a uniform age and that the sample remained a closed system. (b) Ar loss grain boundaries indicates ‘young ages’ in lower temperatures and a ‘plateau age’ in the center of the grain, where there was no Ar loss. (c) Different events of Ar loss recording an ancient Ar loss and an ‘original age’ in the center grain (modified from Schaefer 2016).

In addition to Ar loss, the system can be subject to contamination from extraneous Ar due to the diffusion of ^{40}Ar from external environment into mineral grains. Such ^{40}Ar , which is not associated with the *in situ* decay of ^{40}K , is termed excess Ar ($^{40}\text{Ar}_E$). This excess of Ar can be incorporated in a mineral when it crystallizes in an Ar-rich environment (such ^{40}Ar is referred to as inherited Ar) or due to diffusion out of a crystal lattice into an adjacent grain during metamorphic or thermal events. Since each heating step is an independent measurement of the Ar isotope composition, the data could be considered analogously to a conventional

isochron. However, the x -axis of an isochron diagram plots $^{39}\text{Ar}/^{36}\text{Ar}$ instead of $^{39}\text{K}/^{36}\text{Ar}$, since the parent isotope is being measured by proxy via ^{39}Ar . Nonetheless, because the ^{36}Ar is present on both axes of such plots and occurs in very small amounts in many samples, errors in its measurement can introduce correlations that mimic isochrons. Hence, it is better to use ‘inverse’ isochron plots in which $^{36}\text{Ar}/^{40}\text{Ar}$ is represented on the y -axis and $^{39}\text{Ar}/^{40}\text{Ar}$, on the x -axis (Figure 2). Since all ^{36}Ar is non-radiogenic, the age of the sample can be calculated from the $^{39}\text{Ar}/^{40}\text{Ar}$ value at the intercept of the inverse isochrone with the x -axis since in this point $^{36}\text{Ar} = 0$. The y -intercept corresponds to the inherited or trapped Ar. The inverse isochron is a robust alternative because the determined age does not change with additional excess Ar, since it depends only on the $^{39}\text{Ar}/^{40}\text{Ar}$ when $^{36}\text{Ar}/^{40}\text{Ar} = 0$, and is independent of the slope of the inverse isochron.

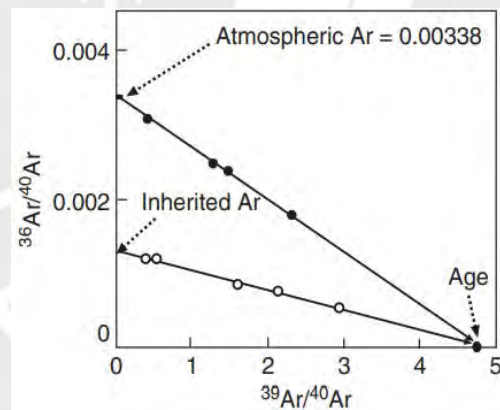


Figure 2. Inverse Isochron diagram for Ar isotopes. The age of the sample is calculated from the $^{39}\text{Ar}/^{40}\text{Ar}$ value at the intercept with the x -axis (modified from Schaefer 2016).

There are diverse advantages in the use of Ar-Ar method. Since all measurements are made in the same sample and equipment and only ratios ($^{40}\text{Ar}/^{39}\text{Ar}$) are needed, problems with inhomogeneity and differing machine calibrations are eliminated. Further, this method can achieve routine analytical uncertainties less than $\pm 0.5\%$ and little sample is required for analysis. However, since a nuclear reactor is required, the samples irradiated are radioactive and must be appropriately handled and stored.

Because of the fact that K is commonly a major or minor element in many minerals in diverse rock types, coupled with strong temperature dependence of Ar diffusion in minerals, the Ar-Ar method has a widespread geological application. This method can be applied for the refinement of time-scale boundaries due to its accuracy and precision. It can also be applied to study sedimentary basin evolution and detrital provenance. Since $^{40}\text{Ar}/^{39}\text{Ar}$ dating records higher-temperature processes, it may also help solve timing of metasomatism (e.g., hydrothermal alteration) and metamorphism by dating K-bearing phases formed during these processes and hence, indirectly, the timing of associated mineralization and deformational events. Since Ar is a noble gas particularly sensitive to temperature, this method is also useful in thermochronology.

1.2. Previous radiometric dating in the Macusani Structural Zone

The Macusani structural zone has captured the attention of geoscientists for decades due to a number of peculiarities. As described in more detail in the Geological Setting of this thesis, it records important examples of strongly peraluminous magmatism, including some highly improbable volcanic manifestations due to the high viscosity of these magmas that commonly favor their crystallization at depth in the form of batholiths (Sandeman et al. 1997; Pichavant et al. 1988; 2024a, b). Among the volcanic products, the existence of the so-called macusanite stands out. Macusanite is a rare obsidian glass with extreme enrichment in incompatible lithophile elements (Li, Rb, Cs, Sn, U, B, and F; Linck 1926; French and Meyer 1970; French et al. 1978; Noble et al. 1984; Pichavant et al. 1987, 1988a) notably used as a geochemical reference material for the analysis of Li-Cs-Ta (LCT) pegmatites (e.g., London 2015). The Macusani Structural Zone has also received attention because of the rich variety of mineral resources. Notably, it hosts the northern extension of the Central Andean Tin Belt into Peruvian territory, which includes the world-class Sn-Cu San Rafael deposit and a series of other smaller Sn-W-polymetallic deposits, occurrences, and mineral showings (Clark et al. 1983, 1990;

Mlynarczyk and Williams-Jones 2005). It also hosts what is to become the world's largest Ag producer, the Ag-Pb-Zn Corani deposit (Swarthout et al. 2010; Ausenco 2019), upon the beginning of its exploitation planned by the end of this year (Bear Creek Mining Corporation 2024; IIMP 2024). The Macusani Structural Zone, and in particular the Macusani Volcanic Field within it, is also host to energy metal resources, namely Li and U.

Probably because of these particularities and geological riches, the Macusani Structural Zone has received a lot of attention from a geochronological perspective, with abundant radiometric dates available in the literature. A compilation of available radiometric dates on rocks from the Macusani Structural Zone and nearby areas in contiguous geologic domains (i.e., Cordillera de Carabaya and Central Andean Backthrust Belt—cf. Geological Setting and Fig. 3) is presented in Appendices A-B. The location of the dated samples as provided in the compiled database is shown in Figures 4-7 and their contextualization in general stratigraphic columns is presented in Figures 8-9.

The first radiometric dating of rocks from the Macusani Structural Zone was performed in macusanite. Fleischer and Price (1964), who identified such glasses as “tektites” (i.e., natural glass formed from terrestrial material ejected during meteorite impacts), reported a fission track date of 4.3 ± 0.4 Ma. Six years later, Barnes et al. (1970) reported K-Ar dates for macusanite and biotite in ‘sillar’ (i.e., local name for ignimbrite), which yielded 4.2 ± 1.5 Ma and 4.1 ± 1.0 Ma, respectively. The authors highlighted the good agreement between their K-Ar date in macusanite with the fission track date recorded by Fleischer and Price (1964). Renewed efforts to date macusanite arrived in the 1990s. Cheilletz et al. (1992) obtained two $^{40}\text{Ar}/^{39}\text{Ar}$ whole-rock dates on macusanite from Chilcuno North of 3.5 ± 0.6 Ma and 3.3 ± 1.7 Ma; however, the step-heating spectra revealed extensive Ar loss. Poupeau et al. (1992) performed K-Ar and fission track analyses on macusanite and the respective results were in a range between $5.72 \pm$

0.12 Ma and 5.44 ± 0.06 Ma, and between 7.79 ± 0.11 Ma and 4.82 ± 0.12 Ma. Shortly after, Poupeau et al. (1993) revisited and refined fission-track dates on macusanite contributing 71 additional analyses, which led the authors to construe three eruptive periods of macusanite at around 7 ± 1 Ma, between 5.7 Ma and 5.3 Ma, and around 4.8 ± 0.2 Ma.

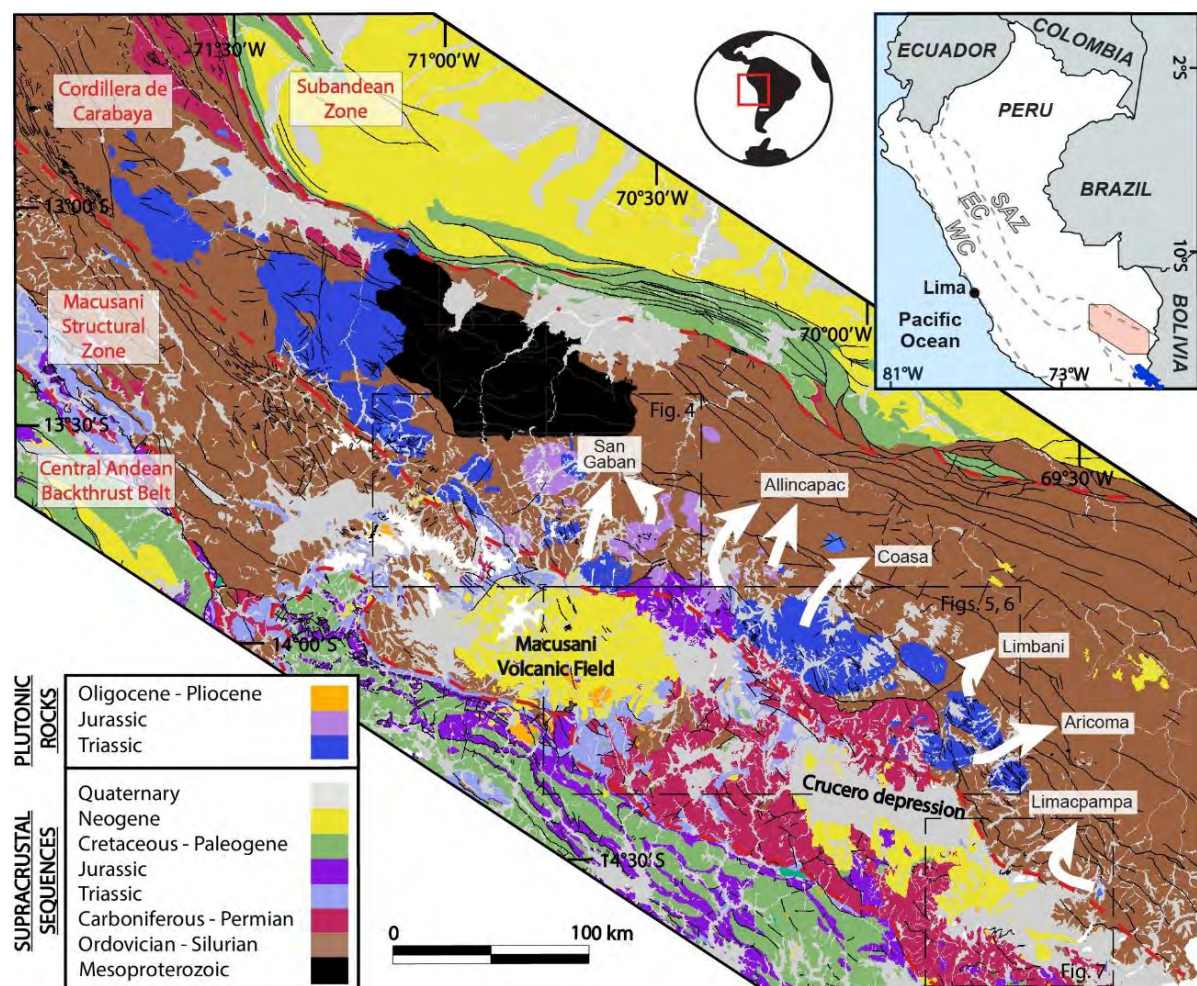


Figure 3. Simplified geological map of the Macusani Structural Zone and contiguous morphostructural domains adapted from 50k sheets of INGEMMET (2023). The location of the map within the Peruvian territory is shown in the top-right inset. The dashed black lines indicate the locations of the geological maps showing compiled geochronological data in Figures 4 to 8. Age brackets for intrusive rocks are based on Clark et al. (1983), Kontak (1984), Bonhomme et al. (1985a, b, 1988), Kontak et al. (1986, 1987, 1990a, b), Laubacher et al. (1988), Pichavant et al. (1988), Cheilletz et al. (1992), Sandeman et al. (1997), Mišković et al. (2009), Spikings et al. (2016), and Harlaux et al. (2021, 2023). Morphostructural provinces in upper-right inset are after Benavides-Cáceres (1999). Key: Western Cordillera (WC); Eastern Cordillera (EC); Sub-Andean Zone (SAZ).

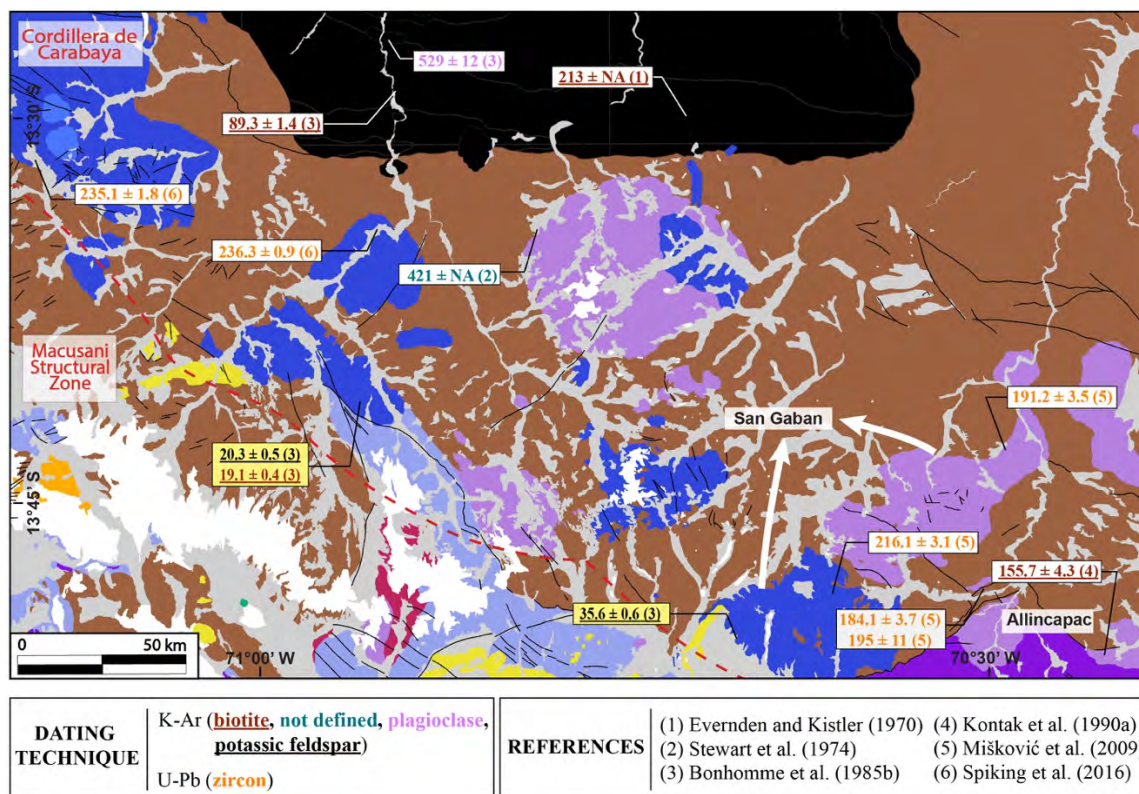


Figure 4. Simplified geological map with previous radiometric dates on intrusive (white boxes) and volcanic (yellow boxes) rocks (see location of the area in Fig. 3). Geological mapping at 50k scale from INGEMMET (2023). Color code of the geological map as in Figure 3.

Radiometric dating of plutonic rocks from the Cordillera de Carabaya have also received ample attention. Evernden and Kistler (1970) provided three K-Ar biotite dates for a diorite hosted in the Iscaybamba Complex (213 Ma), a porphyritic granite from the Coasa pluton (207 Ma), and a syenite from the Allincapac complex (180 Ma). Stewart et al. (1974) published three further K-Ar dates for granitic rocks from the Cordillera de Carabaya of 421 Ma (granite located NW of San Gaban), 164 Ma, and 40 Ma (granodiorites in the Limbani pluton). Lancelot et al. (1978) published a U-Pb zircon date of 238 ± 11 Ma for a granite from the Coasa pluton.

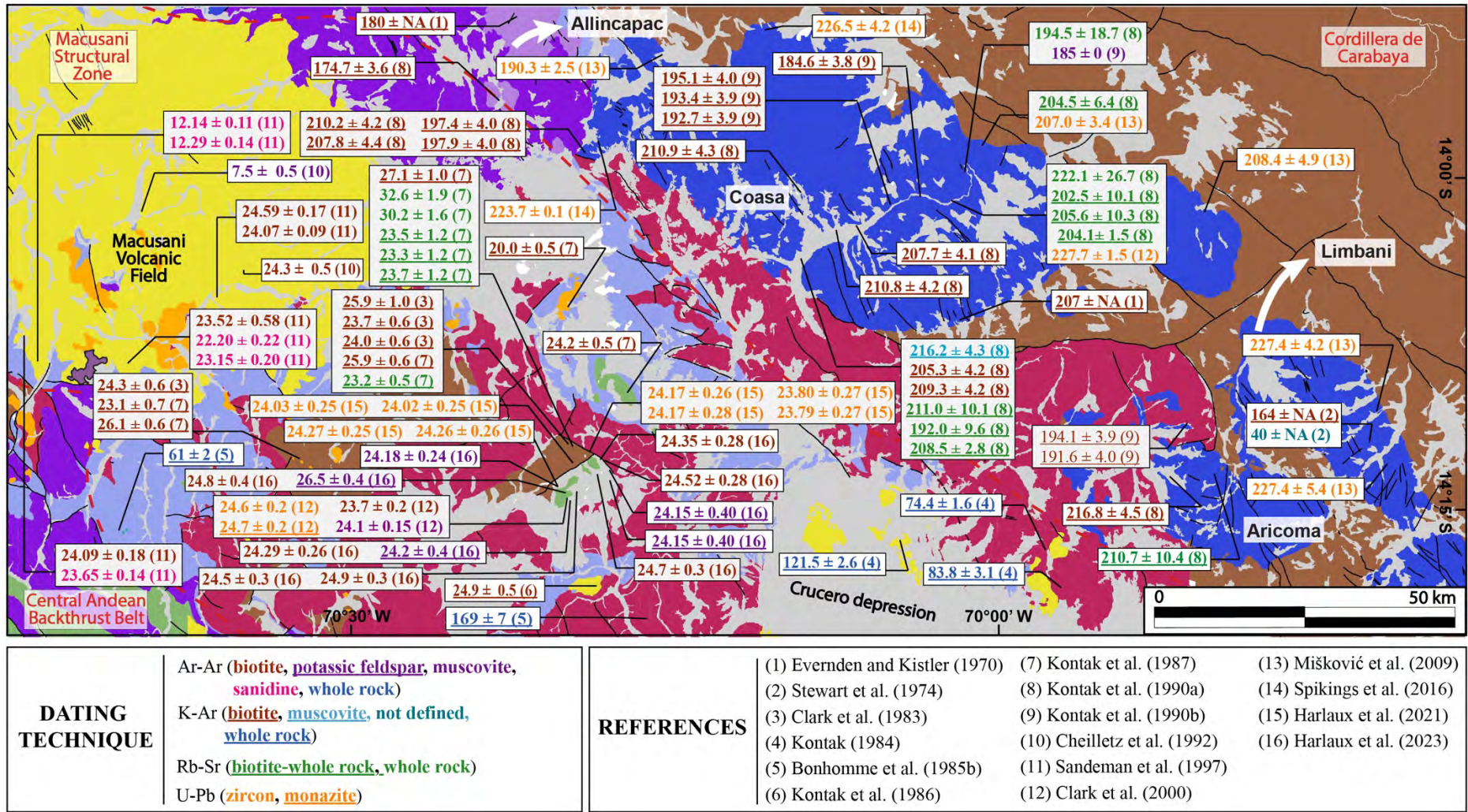


Figure 5. Simplified geological map with previous radiometric dates on intrusive rocks (see location of the area in Fig. 3). Geological mapping at 50k scale was extracted from INGEMMET (2023). Color code of the geological map as in Figure 3.

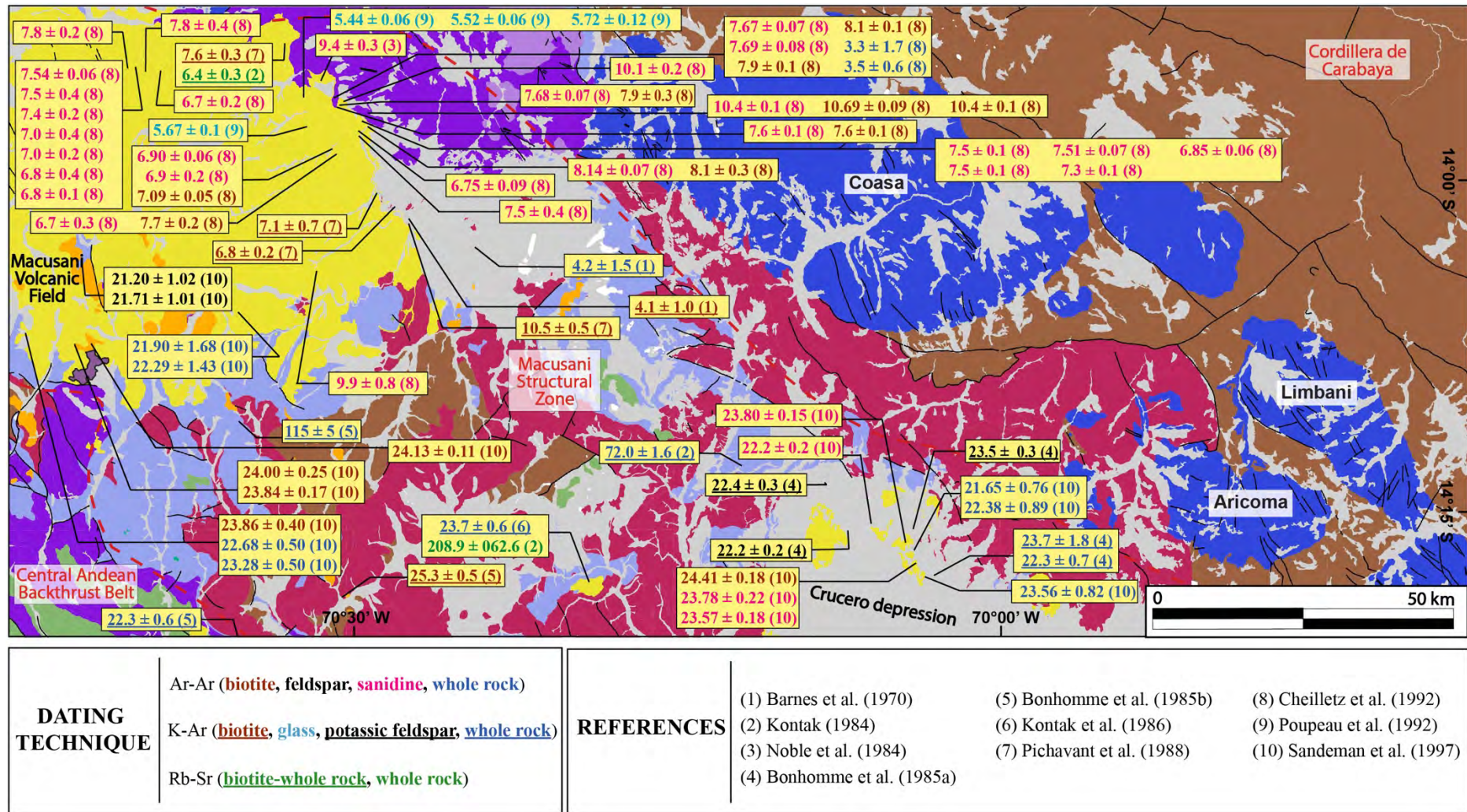


Figure 6. Simplified geological map with previous radiometric dates on volcanic rocks (see location of the area in Fig. 3). Geological mapping at 50k scale was extracted from INGEMMET (2023). Color code of the geological map as in Figure 3.

Some years later, Kontak et al. (1990a) published geochronological data on diverse upper Paleozoic to Jurassic igneous suites exposed in the Cordillera de Carabaya. For the Coasa Pluton, these workers obtained Rb-Sr whole-rock dates between 222.1 ± 26.7 Ma and 194.5 ± 18.7 Ma and Rb-Sr whole-rock-biotite dates between 208.5 ± 2.6 Ma and 192 ± 9.6 Ma. The reported K-Ar biotite dates range between ca. 211 and 203 Ma, and K-Ar muscovite dates were of 216.2 ± 4.3 Ma and 212.7 ± 4.3 Ma. Younger radiometric dates on rocks from the Coasa Pluton were interpreted by the authors to reflect partial resetting, particularly in the Northern area. Syenite samples from the Allincapac Complex yielded a Rb-Sr whole-rock regressed date of 206 ± 70.8 Ma, and biotite K-Ar dates of ca. 175 and 155 Ma. Samples from the Limacpampa and Aricoma plutons yielded a Rb-Sr muscovite date of 199.0 ± 10 Ma and a Rb-Sr whole rock-biotite date of 210 ± 10.4 Ma. In addition, samples from the Aricoma Pluton yielded K-Ar muscovite and biotite dates of 225.0 ± 14.8 Ma (quartz vein) and 216.8 ± 4.5 Ma, respectively. The Rb-Sr and K-Ar dating performed by Kontak et al. (1990a) thus depicted a major episode of batholith emplacement in the Late Triassic.

Much more recently, Mišković et al. (2009) performed zircon U-Pb dating of intrusive rocks from the Cordillera de Carabaya. Two samples of (monzo)syenitic intrusives of the southern Allincapac volcano-plutonic complex yielded dates of 195 ± 11 and 184.1 ± 3.7 Ma (i.e., Early Jurassic), which are slightly younger or coeval to those obtained for (monzo)granites from the central and northern Cordillera de Carabaya areas including those from the Coasa (227.7 ± 5.6 Ma, 208.4 ± 4.9 Ma, and 207.0 ± 3.4 Ma), Ayapata (190.3 ± 2.5 Ma), San Gaban (216.4 ± 3.1 Ma and 191.2 ± 3.5 Ma), and Limbani (227.4 ± 5.4 Ma and 227.4 ± 4.2 Ma) plutons. Spikings et al. (2016) also dated intrusive rocks from the Cordillera de Carabaya by the same method. Granitic rocks from the Coasa pluton yielded dates between 235.1 ± 1.8 Ma and 223.7 ± 0.1 Ma.

Later tectono-thermal events recorded in igneous rocks from the northeastern flanks of the Cordillera de Carabaya were investigated in more detail by Kontak et al. (1990b) through K-Ar, $^{40}\text{Ar}/^{39}\text{Ar}$, and fission-track analyses. Analyzed rocks were collected along four transects: Coasa Pluton, San Gaban-Ollachea, Ananea-Limacpampa, and Aricoma-Limbani. Discordant K-Ar analyses on rocks from all four transects show a decrease in the obtained dates from the southwest to the northeast from concordant dates at ca. 210 Ma to discordant dates as young as ca. 36 Ma. In addition, five $^{40}\text{Ar}/^{39}\text{Ar}$ step heating analyses showed disturbed age spectra in three transects and fission-track analysis on apatite mostly clustered around ca. 18 Ma (Coasa, Aricoma-Limbani, and Ananea-Limacpampa). These data led Kontak et al. (1990b) to identify two separated thermal disturbance events: one major tectono-thermal event at ca. 37 Ma (Eocene-Oligocene boundary), and a younger Miocene event at ca. 18 Ma.

Tertiary volcanic and volcanogenic deposits found within different volcanic fields along the Macusani Structural Zone, and coeval and cogenetic sub-volcanic intrusives, have also been extensively dated. In his doctoral dissertation, Kontak (1984) obtained K-Ar, $^{40}\text{Ar}/^{39}\text{Ar}$, and Rb-Sr dates on rocks from the Macusani Structural Zone and the Cordillera de Carabaya. Most of these dates were later published in Kontak et al. (1986, 1987, 1990a, b) and Pichavant et al. (1988) and will be disclosed below. The only exceptions include K-Ar dates for rocks from the Crucero Depression (83.8 ± 3.1 Ma and 74.4 ± 1.6 Ma in granodiorites; 121.50 ± 2.60 Ma in a dolerite), and Rb-Sr dates for a shoshonite from the Picotani Group (208.9 ± 62.6 Ma) and a tuff from the Macusani Formation (6.4 ± 0.3 Ma).

Noble et al. (1984) reported a K-Ar sanidine date of 9.4 ± 0.3 Ma for an ash-flow tuff in the Macusani Volcanic Field. One year later, twelve K-Ar dates on igneous rocks from the Macusani Structural Zone were reported by Bonhomme et al. (1985a), who established two age ranges in the Crucero basin: 25 to 22 Ma for samples from the Cayconi Formation (Picotani

Group), and ca. 12 Ma for a subvolcanic rhyolite intrusion known as the Pucaorco Stock (Quenamari Group). These dates were interpreted as evidence of late Oligocene to early Miocene and mid to late Miocene volcanic pulses. Bonhomme et al. (1985b) recorded dates between 35 and 20 Ma for “ignimbritic dikes” within Paleozoic strata in the Oriental Cordillera. Kontak et al. (1986) published K-Ar dates on a shoshonite (whole rock; 23.7 ± 0.6 Ma) and a monzogranite dyke with content of shoshonitic rocks (biotite from the Antauta dyke; 24.9 ± 0.5 Ma).

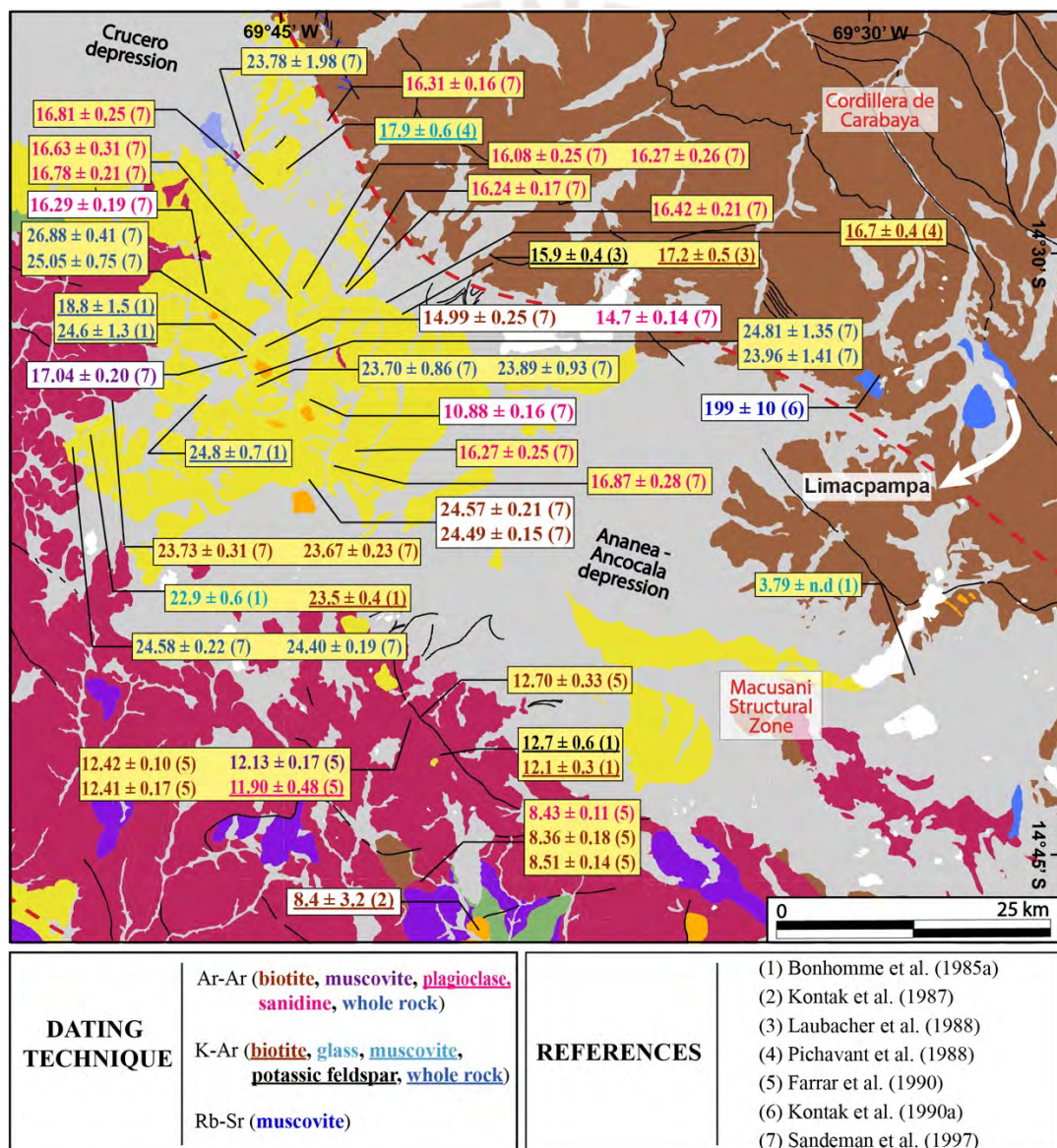


Figure 7. Simplified geological map with previous radiometric dates on plutonic (white boxes) and volcanic (yellow boxes) rocks (see location of the area in Fig. 3). Geological mapping at 50k scale from INGEMMET (2023). Color code of the geological map as in Figure 3.

Laubacher et al. (1988) provided temporal constraints on the Crucero Basin (SE Macusani; Fig. 3). The authors reported K-Ar analyses—previously given by Bonhomme et al. (1985a)—on basic and silicic volcanic rocks interbedded with fanglomerate and lacustrine sediments of the Cayconi Formation. The dates were comprised in the range between ca. 25 and 22 Ma for the middle members, and between ca. 17 and 12 Ma for the upper members. These authors also provided two new dates on ignimbrites from the Picotani Field of 17.2 ± 0.5 Ma and 15.9 ± 0.4 Ma (Fig. 8). The same year, Pichavant et al. (1988) reported K-Ar mica analyses on tuff samples from the Picotani and Quenamari groups. Samples from the Picotani Group yielded dates of 17.9 ± 0.6 Ma and 16.7 ± 0.4 Ma, while samples from the Quenamari Group yielded dates in the range between 10.5 ± 0.5 Ma and 6.8 ± 0.2 Ma. This allowed the authors to consider a continuous or semi-continuous eruption of silicic magma over a period of ca. 6 M.yr.

A few years later, Cheilletz et al. (1992) presented a volcano-stratigraphic chart supported by 41 new $^{40}\text{Ar}/^{39}\text{Ar}$ dates on sanidine, and biotite from the “Macusani ignimbrite field”. In this investigation the authors studied ~1,400 m of ignimbritic ash-flow tuff distributed along five sections (Huiquiza, Chilcuno North, Chilcuno South, Chapi, and Pampa Orcoyo). The authors defined six volcanic cycles or fundamental cooling units at 10.0 ± 0.5 Ma, $7.8\text{-}8.0 \pm 0.1$ Ma, 7.5 ± 0.1 Ma, 7.3 ± 0.1 Ma, $6.8\text{-}7.0 \pm 0.1$ Ma, and 6.7 ± 0.1 Ma occurring during two brief eruption episodes at 10 ± 1 Ma and 7 ± 1 Ma. In addition, Cheilletz et al. (1992) obtained a plateau date of 24.3 ± 0.5 Ma on biotite from the Revancha Stock and a plateau date of 7.5 ± 0.5 on muscovite from the Chaccaconiza rhyolitic dome.

Sandeman et al. (1997) published 58 new $^{40}\text{Ar}/^{39}\text{Ar}$ dates on extrusive and hypabyssal rock units of the Crucero Supergroup and the Crucero Intrusive Supersuite, respectively (cf. Section 3.2). For the Crucero Supergroup, the authors contributed new dates for rocks from

both the Picotani and Quenamari groups. Dated units of the Picotani Group included the Cerro Queuta, Cerro Huancahuancane, Suratira, Pachachaca, Jama Jama, Cerro Cancahuine, Cerro Sumpiruni, Pucalacaya, Lago Perhuacarca, and Cerro Moromomoroni formations, which yielded dates mostly between ca. 26 and 21 Ma ($n = 30$). For the Quenamari Group, tuff from the Huacchane and Quebrada Escalera formations yielded dates at around 16 Ma ($n = 10$). Intrusive rocks of the Picotani Intrusive Suite yielded dates between ca. 24.5 Ma and 22 Ma ($n = 11$), while plutonic rocks of the Quenamari Intrusive Suite yielded dates in a range between ca. 17 and 11 Ma ($n = 7$).

A number of works focused on mineral deposits found along the Macusani Structural Zone including geochronological data have been published. Many of them are centered on Sn(\pm W \pm polymetallic) deposits in the Peruvian segment of the Central Andean Tin Belt, chiefly in the San Rafael deposit. Clark et al. (1983) provided K-Ar dates of magmatic biotite from three monzogranites from the San Rafael deposit. The obtained dates were 25.9 ± 1.0 Ma, 24.0 ± 0.6 Ma, and 23.7 ± 0.6 Ma. A fourth K-Ar biotite date of 24.3 ± 0.6 Ma was obtained for a monzogranite from the Santo Domingo deposit. In both deposits, these dates were interpreted as intrusion ages and allowed the authors to suggest contemporaneous emplacement. Kontak et al. (1987) performed K-Ar dating of a so-called Quenamari epizonal intrusion (biotite; 27.1 ± 1.0 Ma and 25.9 ± 0.6 Ma), intrusive rocks in the Santo Domingo deposit area (biotite; 26.1 ± 0.6 Ma and 23.1 ± 0.7 Ma), and the Antauta dike (biotite; 24.9 ± 0.5 Ma); in addition, these authors dated greisen alteration in the San Rafael intrusive complex (muscovite; 23.6 ± 0.6 Ma) and reported two K-Ar biotite dates on unmineralized stocks in the southeastern sector of the Macusani Volcanic Field of 24.2 ± 0.5 Ma and 20.0 ± 0.5 Ma. Considerably younger was the K-Ar biotite date that these authors obtained for the Corimpata microgranite stock, located southeast of the Macusani Volcanic Field, of 8.4 ± 0.2 Ma. Rocks from the San Rafael and Quenamari intrusive complexes (whole rock, biotite, and alkali feldspar) reported by Kontak

et al. (1987) yield a Rb-Sr isochrone date of 23.5 ± 0.2 Ma. Farrar et al. (1990) performed $^{40}\text{Ar}/^{39}\text{Ar}$ feldspar and mica dating on subvolcanic granitic intrusions (Corimpata and Pucaorco) and a mineralized vein in the Palca 11 deposit area. Rhyolite of the Corimpata Stock yielded dates between 8.51 ± 0.14 Ma and 8.36 ± 0.18 Ma, and rhyolite of the Pucaorco subvolcanic intrusion, between 12.42 ± 0.10 Ma and 11.90 ± 0.48 Ma. As for the mineralized vein, biotite yielded two $^{40}\text{Ar}/^{39}\text{Ar}$ dates of 24.96 ± 0.13 Ma and 24.82 ± 0.15 Ma and a sample of adularia yielded an $^{40}\text{Ar}/^{39}\text{Ar}$ date of 22.60 ± 0.12 Ma, hence demonstrating that the mineralization at Palca 11 was not related to the emplacement of the Pucaorco Stock (Farrar et al. 1990).

Clark et al. (2000; later recounted in Kontak and Clark 2002) reported further geochronological dates for the San Rafael tin deposit including single zircon and monazite U-Pb dates on a cordierite-biotite monzogranite stock of $24.6 - 24.7 \pm 0.2$ Ma, identified as the age of emplacement; an $^{39}\text{Ar}/^{40}\text{Ar}$ biotite plateau date of 24.1 ± 0.15 Ma for the same stock was interpreted as the cooling age. According to the authors, an $^{39}\text{Ar}/^{40}\text{Ar}$ plateau date of 22.4 ± 0.7 Ma on muscovite from barren tourmaline-quartz veins indicates the age of “retrograde boiling” at 24.1 ± 0.15 Ma while a $^{39}\text{Ar}/^{40}\text{Ar}$ plateau date of 22.4 ± 0.7 Ma on hydrothermal sericite from Veta San Rafael and an $^{39}\text{Ar}/^{40}\text{Ar}$ plateau date of $21.9 - 22.0 \pm 0.2$ Ma on adularia from the nearby Veta Jorge would constrain the age of mineralization. A recent geochronological investigation performed by Harlaux et al. (2021) focused on U-Pb dating of zircons in granitic rocks from the upper Oligocene San Rafael intrusive complex, which yielded dates in the range between ca. 24 and 23 Ma. A lamprophyre dike dated by Harlaux et al. (2021) yielded a similar date of 23.80 ± 0.27 Ma. Harlaux et al. (2023) dated igneous and alteration minerals in granitic rocks from the San Rafael intrusive complex through the $^{40}\text{Ar}/^{39}\text{Ar}$ dating method. Igneous minerals yielded dates narrowly ranging between 26.5 ± 0.40 Ma and 24.1 ± 0.24 Ma. Greisen was dated at 24.24 ± 0.24 Ma (hydrothermal muscovite average plateau date). Furthermore,

these authors performed in situ U-Pb dating of cassiterite in veins constraining the main Sn ore stage between 24.10 ± 0.37 and 23.47 ± 0.53 Ma. Finally, the polymetallic sulfide mineralization formed between 22.72 ± 0.11 and 22.29 ± 0.24 Ma according to $^{40}\text{Ar}/^{39}\text{Ar}$ plateau dates on hydrothermal adularia provided by these workers.

For the Corani Ag-Pb-Zn deposit in the southwest part of the Macusani Volcanic Field, an unpublished report submitted to Bear Creek Mining by Ullrich (2006) gives an $^{40}\text{Ar}/^{39}\text{Ar}$ biotite plateau date of 10.357 ± 0.080 Ma.

With regard to the energy metals, Li (2016) conducted in situ U-Pb-Pa geochronology on supergene meta-autunite found in the SE region of the Macusani Volcanic Field. The obtained dates indicate that the main supergene U mineralization events took place at 69 ka, 130 ka, and 314-317 ka. In contrast, no prior data are available for the lithium mineralization at the Falchani Lithium Project within the Macusani Volcanic Field. The data presented in this thesis therefore represent the first available radiometric dates on tuffaceous units associated with the volcanogenic lithium mineralization in the region.

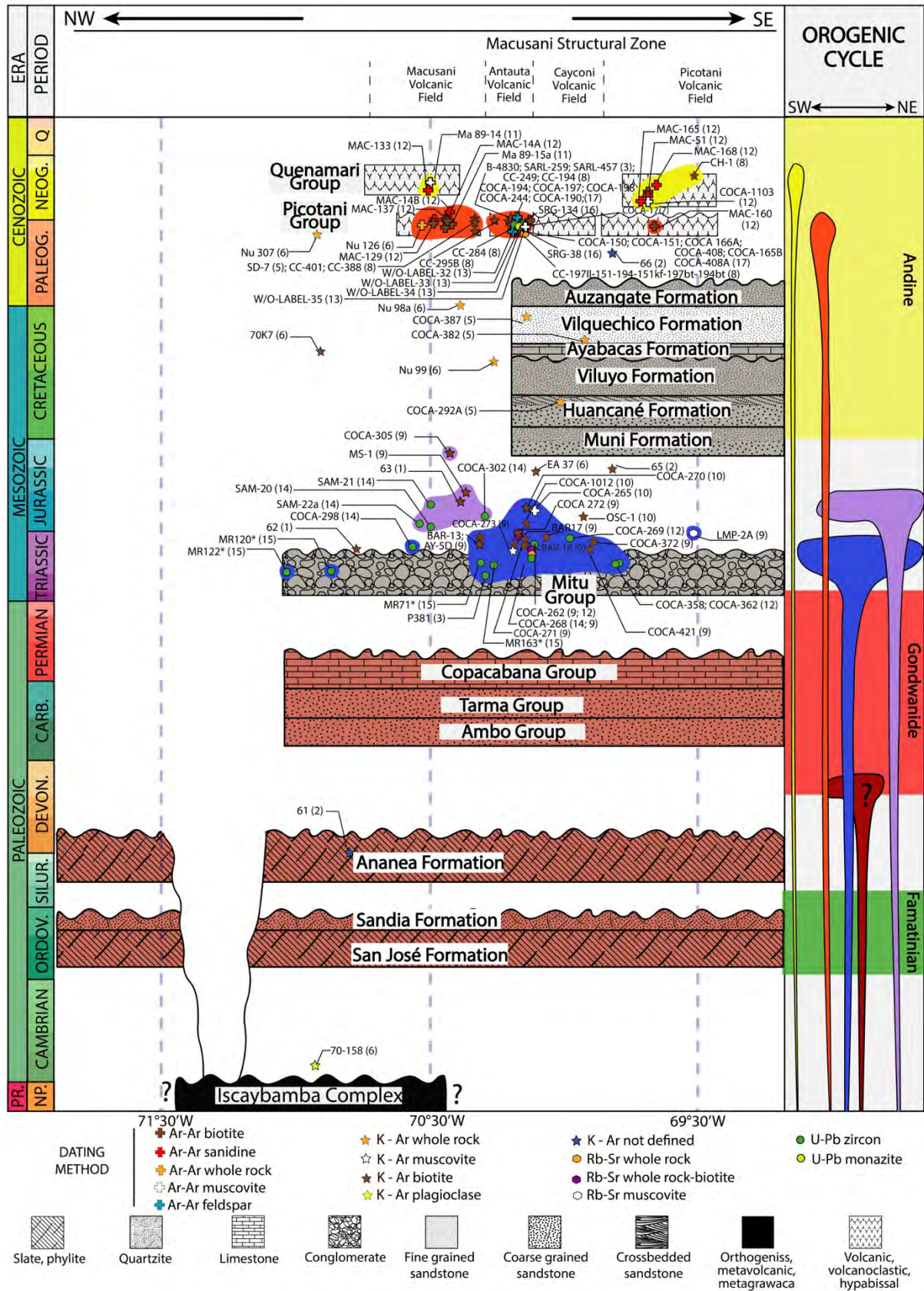


Figure 8. Generalized stratigraphic column traced across the Macusani Structural Zone and contiguous morphotectonic provinces including previous radiometric dating of plutonic rocks. Labels on geochronological data refer to the name of dated samples in the respective original articles. The temporary extension of the Famatinian, Gondwanide, and Andean orogenic cycles in the Central Andes

has been delimited after Laubacher (1978), López-Gamundí and Rosello (1993), Chew et al. (2016), and Carrillo et al. (2021). The ages of the stratigraphic units are after Laubacher (1978), Cheilletz et al. (1992), Sandeman et al. (1997), Spikings et al. (2016), and Rodríguez et al. (2021). References for compiled radiometric dates: (1) Evernden and Kistler (1970), (2) Stewart et al. (1974), (3) Lancelot et al. (1978), (4) Clark et al. (1983), (5) Kontak (1984), (6) Bonhomme et al. (1985b), (7) Kontak et al. (1986), (8) Kontak et al. (1987), (9) Kontak et al. (1990a), (10) Kontak et al. (1990b), (11) Cheilletz et al. (1992), (12) Sandeman et al. (1997), (13) Clark et al. (2000), (14) Mišković et al. (2009), (15) Spikings et al. (2016), (16) Harlaux et al. (2021), and (17) Harlaux et al. (2023).

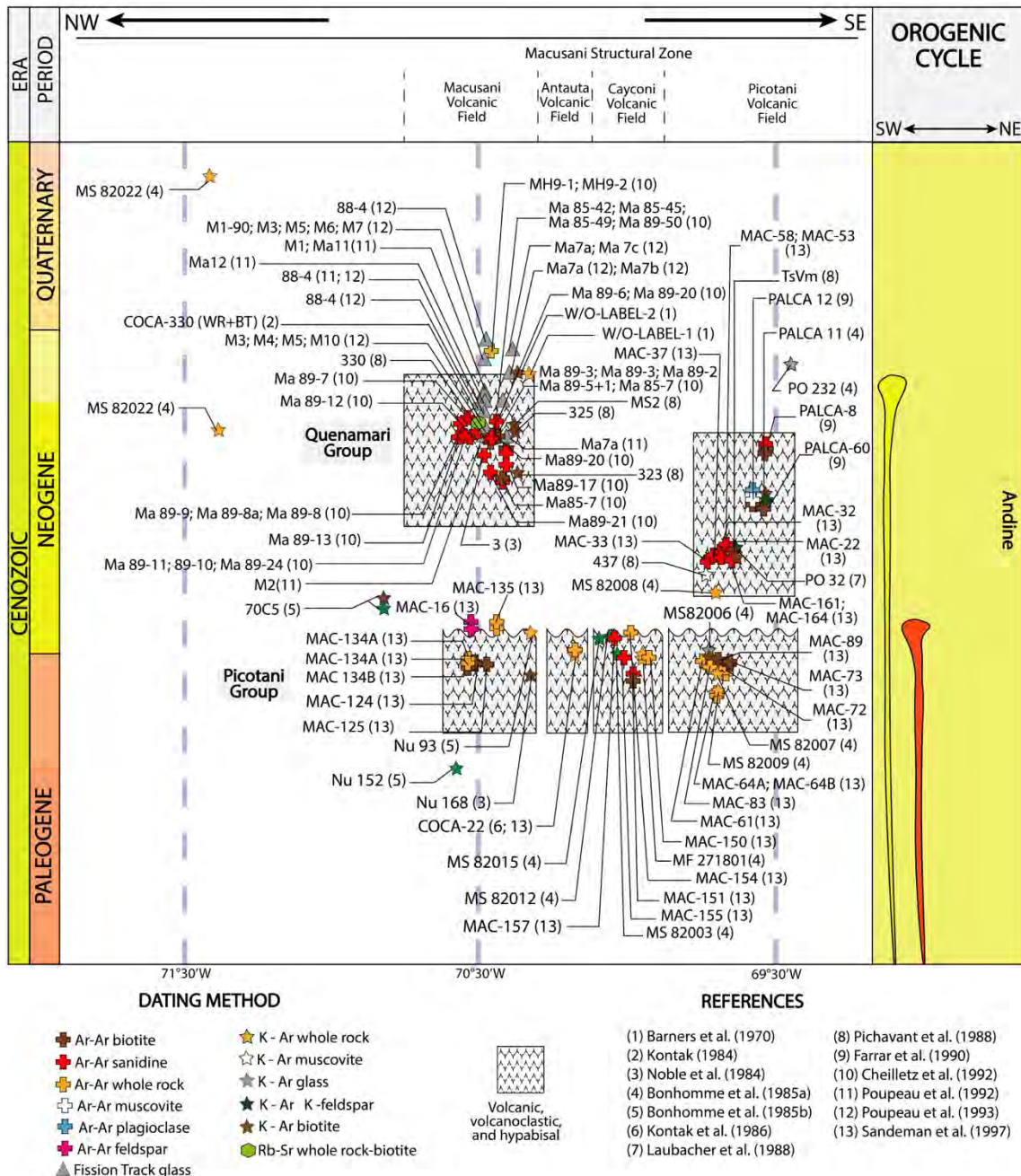


Figure 9. Generalized stratigraphic column traced across the Macusani Structural Zone and contiguous morphotectonic provinces including previous radiometric dating of volcanic rocks. The labels on geochronological data refer to the name used for dated samples in the respective original articles. Stratigraphic units according to Sandeman et al. (1997). The references for compiled radiometric dates are provided in the figure.

1.3. The discovery of the Falchani deposit

In November 2017, the discovery of a major lithium resource in the Falchani Lithium Project in the Macusani Volcanic Field, Carabaya Province, Puno district, southeastern Peru (Fig. 10), was announced. This news was amply reported by national and international media. National newspapers, such as *Correo* and *Gestión*, reported that Macusani Yellowcake S.A.C., then subsidiary of Plateau Energy Metals, discovered 2.5 Mt of lithium carbonate equivalent and 124 million pounds of uranium (AFP Agencia 2018; *Correo* 2018). Likewise, media covering the discovery highlighted lithium contents between 3,500 and 4,000 ppm, which exceed the lithium concentrations in *salar* (i.e., salt flat) brines in hydromorphic lithium deposits hence classifying Falchani as a “*high-grade lithium deposit*” (*Correo* 2018).

Details on the discovery were narrated by the CEO of Macusani Yellowcake, Ulises Solis, in an interview: “*prospecting was being carried out since 2007, and only 8,000 hectares of the 92,000 hectares owned by the company had been explored on the date of the discovery; it is projected that Falchani will become the largest lithium mine, and the production is expected to begin in 2020*” (AFP Agencia 2018; *Correo* 2018). In May 2021, Plateau Energy Metals became “*a wholly owned subsidiary of American Lithium Corp.*” (Saldarriaga, 2021). In a more recent interview in June 2023 for *Gestión* newspaper (Redacción *Gestión* 2023), Simon Clarke, CEO of American Lithium Corp., explained that the planned production would begin as soon as 2026.

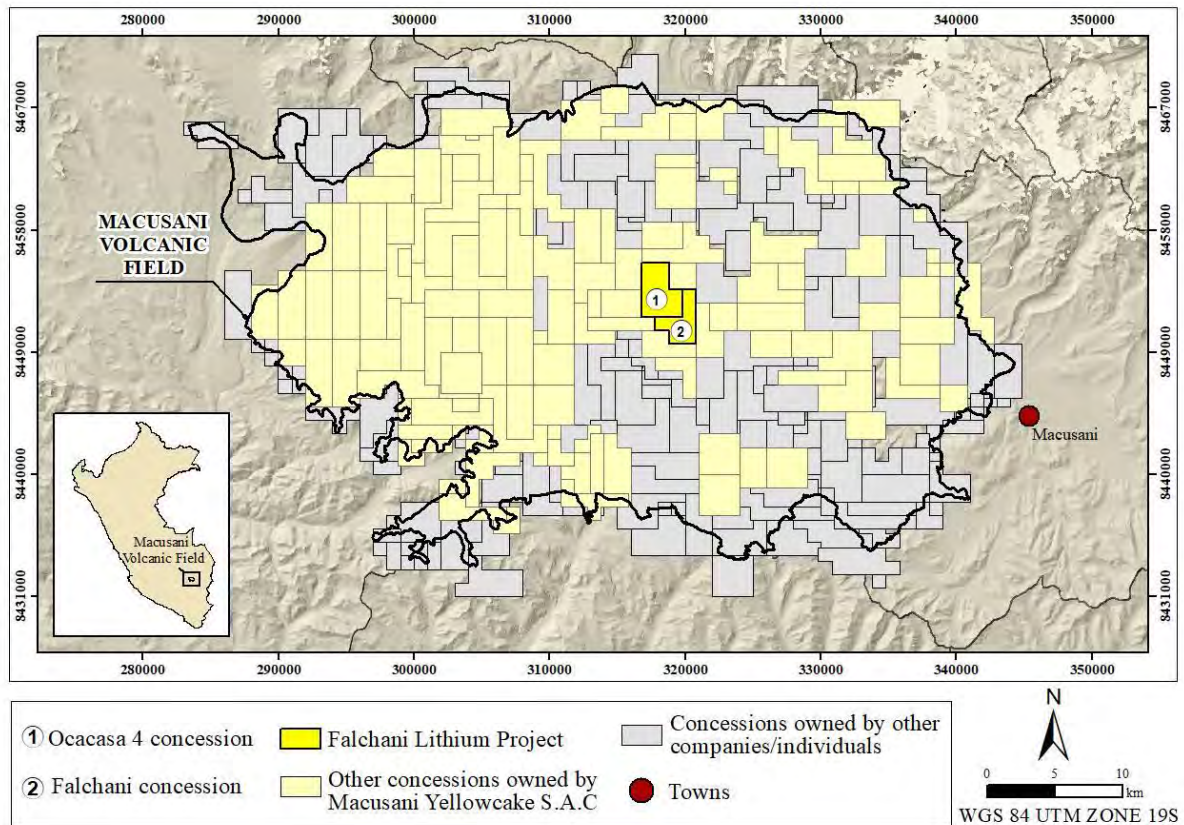


Figure 10. Location of the Falchani and Ocacasá 4 concessions (Falchani Lithium Project) and other concessions owned by Macusani Yellowcake S.A.C. and other companies and individuals in the Macusani Volcanic Field. Delimitation of exploration concessions according to SIDEMCAT (2024).

A technical report by The Mineral Corporation (2019) refers to the potential extension of the lithium mineralization to other areas such as Tres Hermanas, which is located to the south-west of the current mineral resource area. Besides, Vilca (2020) highlighted contents of 2,986 ppm Li in rocks exposed in the Quelcaya area, which is located 6 km west of the Falchani Lithium Project. This new finding was also reported in the newspaper *Gestión*, which explained that the new mineralized zone can extend at least 1.5 km from north to south (Condor 2019). In a more recent *press release* in August 2023, Simon Clarke informed that under the Environmental Impact Assessment (“EIA”) program at the Falchani Lithium project, drilling intersected samples with lithium content as high as 5,025 ppm and cesium contents up to 8,290 ppm—i.e., the highest grades recorded to date for both metals—in Falchani (American Lithium 2023a). At the time of writing these lines, American Lithium has just announced a 476 %

increase in Li resources from 0.96 Mt Li_2CO_3 in March 2019 to 5.53 Mt Lithium Carbonate Equivalent (LCE) in October 2023, adding K, Cs, and Rb to the block model (American Lithium 2023b). This includes a measured resource of 1.01 Mt LCE (69 Mt @ 2,792 ppm Li), an indicated resource of 4.52 Mt LCE (378 Mt @ 2,251 ppm Li), and an inferred resource of 3.99 Mt LCE (506 Mt @ 1,481 ppm Li; Table 1).

Table 1. Mineral resources estimate for the Falchani Project in October 2023.

Cut Off Li (ppm)	Volume (Mm ³)	Tonnes (Mt)	Li (ppm)	Million Tonnes (Mt)			Cs (ppm)	K (%)	Rb (ppm)
				Li	Li_2CO_3	$\text{LiOH}\cdot\text{H}_2\text{O}$			
Measured									
600	29	69	2,792	0.19	1.01	1.15	631	2.74	1,171
1,000	27	65	2,915	0.19	1.01	1.15	647	2.71	1,208
1,200	25	61	3,142	0.18	0.96	1.09	616	2.74	1,228
Indicated									
600	156	378	2,251	0.85	4.52	5.14	1,039	2.92	1,055
1,000	136	327	2,472	0.81	4.31	4.9	1,095	2.87	1,104
1,200	129	310	2,549	0.79	4.20	4.78	1,069	2.86	1,146
Measured + Indicated									
600	185	447	2,327	1.04	5.53	6.29	976	2.90	1,072
1,000	163	392	2,551	1.00	5.32	6.05	1,021	2.84	1,121
1,200	154	371	2,615	0.97	5.16	5.87	1,009	2.84	1,130
Inferred									
600	198	506	1,481	0.75	3.99	4.54	778	3.31	736
1,000	138	348	1,785	0.6	3.3	3.3	886	3.18	796
1,200	110	276	1,961	0.54	2.87	3.27	942	3.10	850

Note: Extracted from American Lithium (2023).

The Mineral Corporation (2019) reports that the lithium resource in the Falchani Lithium Project is associated with Pliocene and Miocene tuff, ignimbrite, and interbedded sedimentary rocks belonging to the Quenamari (a.k.a. Macusani) Formation. The mineralization is interpreted to be linked to glass-rich acidic volcanic tuff and transitional Li-rich breccia deposited subaerially in a crater lake volcano-sedimentary environment. In the aforementioned report, the local stratigraphy is divided into the following units: i) the Upper Rhyolite (URH), which is unmineralized; ii) the Upper Breccia (UBX), which is mineralized and has a thickness ranging from 10 m to 20 m; iii) the Lithium-rich Tuff, which hosts the highest Li grades and

has thicknesses from 50 to 140 m; iv) the Lower Breccia (LBX), which is mineralized and has a variable thickness up to 175 m; and v) the Lower Rhyolite (LRH), which is unmineralized.

1.4. Conundrum

In November 2017, the discovery of a major lithium resource in the Falchani Lithium Project, Carabaya Province, Puno district, was trumpeted. To date, 5.53 Mt LCE (lithium carbonate equivalent) measured and indicated resources have been announced (American Lithium 2023b). The lithium resource is located in the central area of the Macusani Volcanic Field and mostly hosted by the so-called Lithium-rich Tuff, a previously uncatalogued—and hence undated—unit ascribed to the Macusani (a.k.a. Quenamari) Formation (The Mineral Corporation 2019). The lack of geochronological data on the Lithium-rich Tuff precludes its correct temporal correlation with previously described volcanic and intrusive units of the exposed in the Macusani Volcanic Field and nearby domains. Due to its economic importance, the correct stratigraphic and tectono-magmatic contextualization of the Lithium-rich Tuff and associated prospective units will represent a powerful tool for enhanced regional exploration for lithium.

1.5. Objectives

General Objective:

To stratigraphically and tectono-magmatically contextualize the so-called Lithium-rich Tuff unit and associated ore units in the Macusani Volcanic Field within the Neogene evolution of the Central Andes.

Specific Objectives:

- a) To perform geochronological dating of igneous phases in the Lithium-rich Tuff and associated brecciated tuff through the $^{40}\text{Ar}/^{39}\text{Ar}$ method;

- b) To compare the obtained dates with previous radiometric dating on rocks from the Macusani Structural Zone and surrounding morphostructural domains;
- c) To contextualize the Lithium-rich Tuff within the local stratigraphy; and
- d) To discuss the tectono-magmatic setting of emplacement of the Lithium-rich Tuff.

1.6. Hypothesis

The Mineral Corporation (2019) describes the Lithium-rich Tuff as one of the youngest stratigraphic levels of the Neogene Quenamari (a.k.a. Macusani) Formation. According to previous geochronological data on intrusive and volcanic rocks in the Macusani Volcanic Field (e.g., Cheilletz et al. 1990, 1992; Sandeman et al. 1997), this would mean that the volcanic event that gave rise to the Lithium-rich Tuff probably took place between ca. 10 and 6.5 Ma.

1.7. Justification

Lithium, the lightest metal in the periodic table, has been cataloged as a critical raw material by the European Commission (2020) and the United States Geological Survey (2022). It is used in air treatment, glass and ceramics manufacturing, metallurgy, pharmaceuticals, polymers, and most importantly nowadays, the manufacture of rechargeable lithium-ion batteries (Bibienne et al. 2020). Lithium-ion batteries contribute to the reduction of the global warming by allowing the change from the current (oil) energy matrix to renewable energies.

Technical reports indicate that the Falchani Lithium Project contains indicated plus inferred resources of 5.53 Mt LCE (American Lithium 2023b), mostly hosted in a stratigraphic unit named by the companies prospecting in the area as Lithium-rich Tuff. This unit had not been documented in previous research works dealing with the volcano-sedimentary stratigraphy of the Macusani Volcanic Field and, despite its economic importance and likely continuity across the Macusani Volcanic Field, radiometric dating has not been previously

attempted. The radiometric dating performed in the present study seeks the stratigraphic ascription of the Lithium-rich Tuff and the contextualization of the associated volcanic event in the Neogene evolution of the Central Andes of southern Peru.

2. METHODOLOGY

2.1. Sampling

Nine rock samples were selected for $^{40}\text{Ar}/^{39}\text{Ar}$ dating. Eight of the samples are from the Falchani concession in the Falchani Lithium Project, and one sample is from the southernmost part of the Macusani Volcanic Field (former San Vicente White concession; Fig. 11). Of the samples from the Falchani concession, five correspond to Lithium-rich Tuff (2021-MAC-08A, 2021-MAC-11B, 2021-MAC-025, 2021-MAC-038, and 2021-MAC-048) and three correspond to brecciated tuff (2021-MAC-005, 2021-MAC-006, 2021-MAC-031). The sample from the former San Vicente White concession (2021-MAC-067) is a crystal-rich white tuff of unknown stratigraphic ascription. A list of the studied samples, their location, and brief textural and mineralogical descriptions are provided in Appendix C.

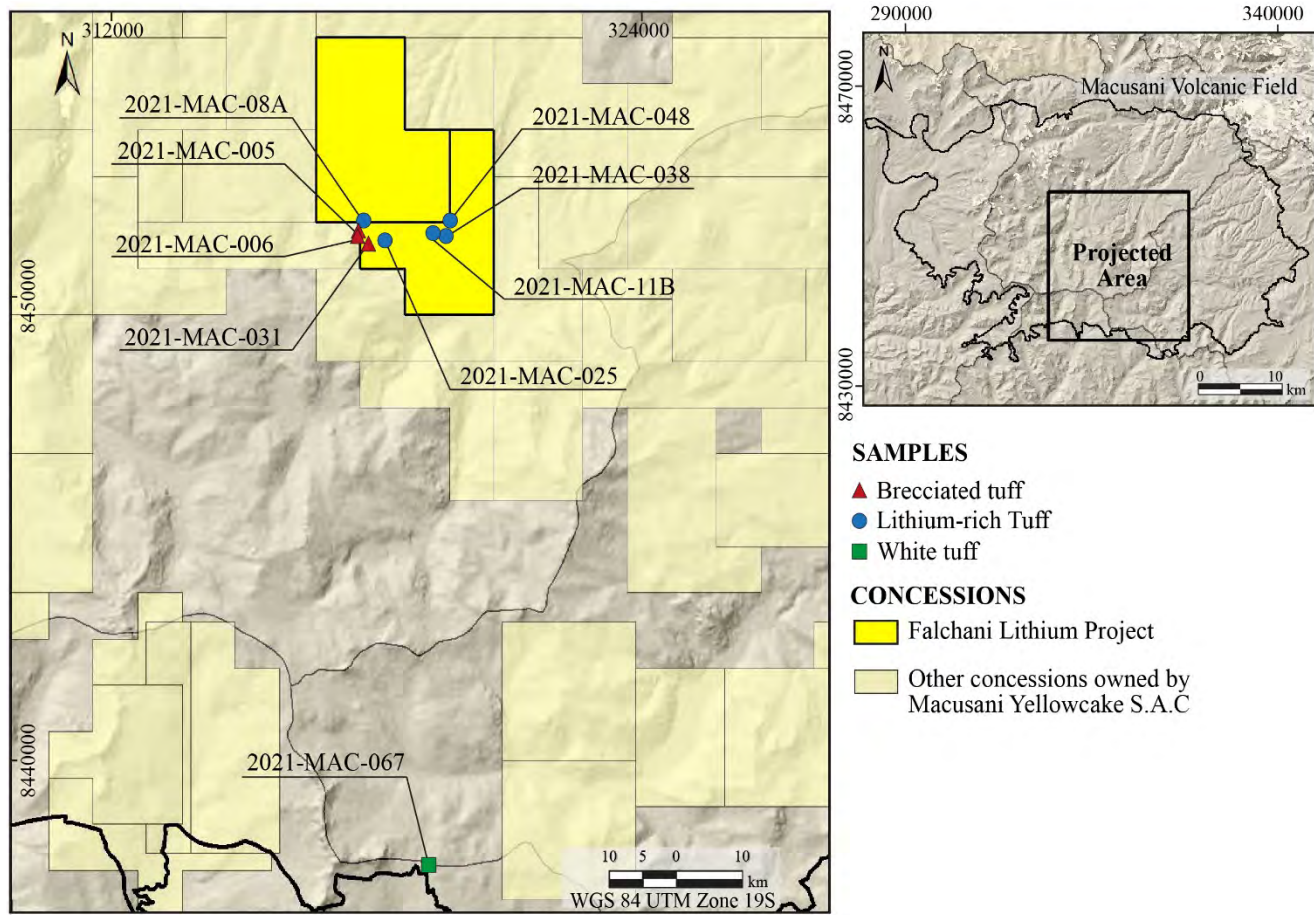


Figure 11. Location of samples selected for $^{40}\text{Ar}/^{39}\text{Ar}$ dating in the Macusani Volcanic Field. Delimitation of exploration concessions according to SIDEMCAT (2024).

2.2. $^{40}\text{Ar}/^{39}\text{Ar}$ geochronology

For mica separation, the nine selected rock samples were crushed and sieved, and individual mica crystals were handpicked under a binocular loupe. Micas separates were analyzed by the $^{40}\text{Ar}/^{39}\text{Ar}$ method at the University of Nevada in Las Vegas. To perform the irradiation, the samples were wrapped in Al foil and stacked in sealed fused silica tubes with internal diameter of 6 mm. Neutron fluence monitors (FC-2, Fish Canyon Tuff sanidine) were placed at the base, top, and between every three unknown samples in the tube. Additionally, to monitor neutron induced argon interferences from K and Ca, synthetic K-glass and optical grade CaF_2 were included in the irradiation packages. The loaded tubes were packed in an Al container and irradiated for six hours at the Oregon State TRIGA Reactor, Corvallis, Oregon. To determine the J factors, fusion of 6-10 individual crystals of neutron fluence monitors was carried out. The determined J values were used to fit a 2nd order error weighted polynomial curve and determine the J value for each unknown sample.

The irradiated FC-2 sanidine standards together with CaF_2 and K-glass fragments, were placed in a copper sample tray in a high vacuum extraction line and fused using a 20 W CO_2 laser. To perform the step heating method for analyzing the samples, a double vacuum resistance furnace was used. Additionally, reactive gases were removed by three GP-50 SAES getters before being admitted into an Isotopx NGX-600 multi-collector mass spectrometer. Faraday cups with ATONA amplifiers were used to measure peak intensities for m/z 40, 39, 38, and 37. The 36 m/z peak was measured using an ion counting discrete dynode electron multiplier. Mass discrimination factors (MDF) were monitored assuming an atmospheric $^{40}\text{Ar}/^{36}\text{Ar}$ value of 298.56 (Lee et al. 2006). Furnace blanks were analyzed at appropriate incrementally increasing temperatures. All age determinations and associated uncertainties were calculated using ArArCalc v.2.7.0 (Koppers 2002). The uncertainties are provided at a 2σ confidence level and include errors in data regression, baseline corrections, irradiation

constants, the J curve value, mass fractionation, blanks, and post irradiation decay of ^{37}Ar and ^{39}Ar . External uncertainties are also provided, which include additional propagated errors from natural element abundances, the decay constant, and fluence monitor age. An age of 28.201 Ma (Kuiper et al. 2008) was used for the Fish Canyon Tuff sanidine fluence monitor when calculating ages for the samples. Ages were calculated using the total ^{40}K decay constant of $5.530 \pm 0.097 \times 10^{-10} \text{ yr}^{-1}$ (Min et al. 2000).

For $^{40}\text{Ar}/^{39}\text{Ar}$ analyses a plateau segment consists of 3 or more contiguous gas fractions having analytically indistinguishable ages (i.e., all plateau steps overlap in age at $\pm 2\sigma$ analytical error) and comprising a significant portion of the total gas released (typically >50%). Total gas (integrated) ages were calculated by weighting by the amount of ^{39}Ar released, whereas plateau ages are weighted by the inverse of the variance. For each sample, inverse isochron diagrams are examined to check for the effects of excess argon. Reliable isochrons and plateaus are checked using a probability of fit factor wherein values greater than 5% indicate a concordant plateau or isochron within the 2σ certainty.

3. GEOLOGICAL SETTING

3.1. Geology of the Central Andes in southern Peru: The Oriental Cordillera

The Andes have an approximate extension of 7,000 km (from Venezuela to Patagonia) and are considered the longest subduction-related continental mountain range on Earth (Kay and Mpodozis 2021). This mountain belt is geographically divided into the Northern (0-15°S), Central (15-33°S), and Southern Andes (33-56°S). The study area is located within the Central Andes. At the latitudes of the Peruvian Territory, the Central Andes embrace six morphotectonic units, which from west to east are: the Coastal Cordillera, the Longitudinal Valley or Central Depression, the Occidental Cordillera, the Altiplano Plateau, the Oriental Cordillera, and the Subandean Ranges (Fig. 12; Wörner et al. 2018).

The Macusani Volcanic Field sits on the Oriental Cordillera. In southern Peru, the Oriental Cordillera is composed of three SE-oriented structural domains, each ~50-60 km wide, which are defined by abrupt changes in structural/stratigraphic exposure levels. From SW to NE, these include the Central Andean Backthrust Belt, the Macusani Structural Zone, and the Cordillera de Carabaya (Fig. 3; Perez et al. 2016). The Central Andean Backthrust Belt structural domain is a SW-verging system of thrust faults and folds also known as the Putina (Peru) or Huarina (Bolivia) fold-thrust belt (Sempere et al. 1990; McQuarrie and DeCelles 2001; Jiménez and López-Velásquez 2008). Exposed stratigraphic levels comprise mostly Jurassic and Cretaceous-Paleogene marine and non-marine clastic and carbonate rocks (Sempere et al. 2004; Rodríguez et al. 2021). The Macusani Structural Zone, formerly referred to as the Precordillera de Carabaya (Kontak et al. 1990b; Sandeman et al. 1997) or “a Late Hercynian fold domain” (Dalmayrac et al. 1977), is characterized by faults and folds that are oblique relative to the main Andean trends (Perez et al. 2016). In this domain, a thick succession of Carboniferous to Permian silico-calcareous marine deposits are exposed (Laubacher et al. 1988). In the Macusani Structural Zone, a series of intermontane basins including Macusani, Crucero, and Ananea-Ancocala, are spatially related to Oligocene to Pliocene volcanic fields (Sandeman et al. 1997; Fig. 3). Finally, the Cordillera de Carabaya structural domain (McBride et al. 1983; Clark et al. 1990; Sandeman et al. 1995) is dominated by a suite of Triassic-Jurassic plutons delineating the topographic crest of the Oriental Cordillera and emplaced mostly in Ordovician to Silurian metasedimentary strata (Kontak et al. 1990b; Mišković et al. 2009).

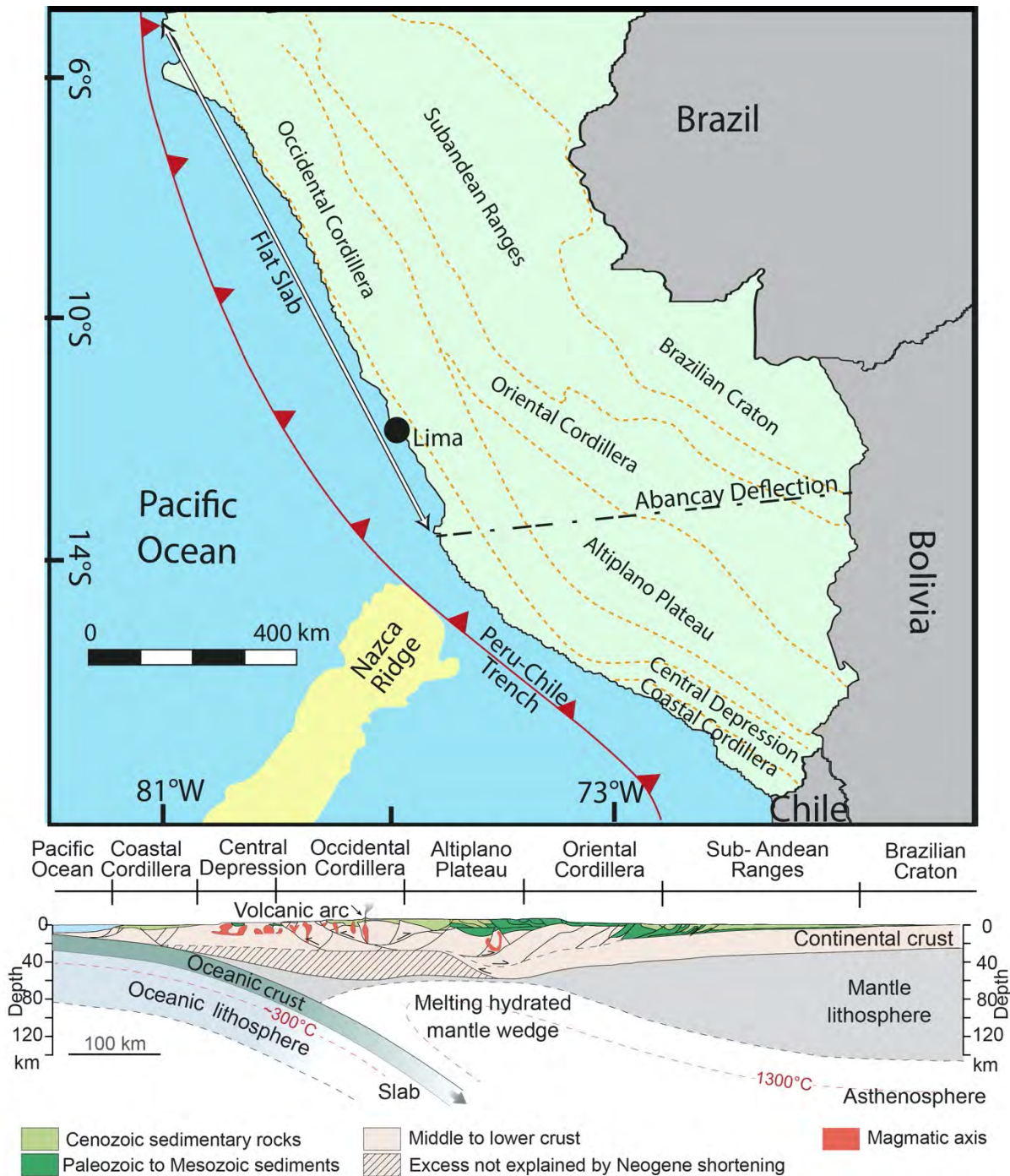


Figure 12. Morphotectonics units of the Central Andes across Peru after Wörner et al. (2018) and geological cross-section of the Andes at 20°S after Baby et al. (1997) and Rochat et al. (1998).

The geodynamic history of the Oriental Cordillera in southern Peru can be contextualized into several orogenies including the Famatinian (Devonian to Carboniferous), Early (ca. 315 Ma) and Late (ca. 260 Ma) Gondwanide, and Andean (since the late Cretaceous) orogenies (Boekhout et al. 2018; Ramos 2018). In southern Peru, the Famatinian orogeny has been correlated with the angular unconformity at the top of the Ananea Formation (Silurian) and the

absence of the Cabanillas Formation (Devonian; Laubacher 1978; Ramos 2018—see description of these and other units mentioned here in Section 3.2). During the Early Gondwanide orogeny, a relative basin deepening is marked by the transition from the Ambo to the Tarma groups (Boekhout et al. 2018). The Late Gondwanide orogeny would have generated the angular unconformity recorded in the top of the Copacabana Group (Sempere et al. 1995) and the onset of peraluminous plutonism (Mišković et al. 2009; Boekhout et al. 2018). However, such Permian peraluminous plutonism is absent south of the Abancay deflection, where the Macusani Structural Zone is located (Fig. 12; Mišković et al. 2009).

The end of the Gondwanide orogeny was followed by the rupture of Pangea (Ramos 2018). This was related to an extensional tectonic regimen, which in the western margin of Pangea translated in the development of a rift system—known as Mitu in Peru—in the Triassic (Spikings et al. 2016). Associated bimodal magmatism consisted of peraluminous plutons and volcanic rocks with continental rifting geochemical affinities (Spikings et al. 2016; Ramos 2018). The structural development of the rift system was influenced by inherited Mesoproterozoic lithospheric architecture (Ramos 2018). According to Spikings et al. (2016), a change in subduction dynamics explain the abortion of the Mitu rift and the re-start of arc magmatism in the Jurassic.

The first part of the Andean orogenic cycle in southern Peru is characterized by an extensional tectonic regimen, the development of an intra-arc basin, and a poorly evolved juvenile magmatism from the Late Jurassic to the Early Cretaceous (Boekhout et al. 2012, 2013). The onset of Andean tectonic compression in the Late Cretaceous was triggered by the separation of South America and Africa and the consequent drift of South America toward the Peruvian – Chilean trench (Benavides-Cáceres 1999; Callot et al. 2008). The growing of the Andean relief and crustal thickening began in the Western Cordillera, as inferred from

Paleocene–Eocene sedimentation record in the present-day Altiplano (Carlotto 2013) and upper Cretaceous–Eocene calc-alkaline batholiths in the Western Cordillera (Pitcher 1985; Mukasa 1986). Shortening-related exhumation in the Eastern Cordillera commenced at 45–38 Ma (Kontak et al. 1985; Allmendinger et al 1997; Gillis et al. 2006). The fact that the central axis of the Triassic rift system, which experienced a greater degree of lithospheric thinning, coincides with the axis of the Oriental Cordillera is interpreted by Sempere et al (2002) as a manifestation of tectonic inversion of pre-Cenozoic structures during the Andean orogenic cycle.

3.2. Regional geology of the Macusani Structural Zone and Cordillera de Carabaya

The Macusani Structural Zone is a SE-oriented morphostructural belt located in southeastern Peru (Perez et al. 2016). It is delimited by a SW-directed thrust contact with the Cordillera de Carabaya morphostructural domain to the NE and a depositional contact with the Central Andean Backthrust Belt in its SW boundary (Fig. 3; Perez et al. 2016). The Macusani Structural Zone is characterized by an abrupt increase in exposed structural levels relative to the Central Andean Backthrust Belt and faults and folds that are conspicuously oblique or nearly perpendicular to the main Andean trends (Perez et al. 2016). Exposed units include >4 km of Carboniferous–Permian strata and thick, well-preserved Triassic deposits of the Mitu Group (Perez et al. 2016). In the Cordillera de Carabaya, glacial mountain ranges are delineated by mostly Triassic–Jurassic batholiths intruding dominantly Ordovician–Silurian (meta-) sedimentary rocks (Fig. 3). Lithostratigraphic units exposed in both the Macusani Structural Zone and Cordillera de Carabaya are described in the following lines.

The oldest unit is represented by the **Iscaybamba Complex** (Fig. 3), a Neoproterozoic metamorphic complex consisting of gneiss, micaschist, amphibolite, micaceous-quartz schist, quartzite, and metavolcanic rocks (Fig. 8; Sánchez and Zapata 2003). The Macusani Structural

Zone and the Cordillera de Carabaya expose one of the most complete Paleozoic sequences in southern Peru. During the Lower Paleozoic, a very thick (~10 km to 15 km) marine sequence of shale and sandstone was deposited during two periods: Ordovician and Silurian-Devonian (Laubacher 1978). The Ordovician period is recorded by a >7-km-thick sequence represented by the San José and Sandia formations (Fig. 8; Laubacher 1978). The **San José Formation**, which has a variable thickness comprised between 3,500 and 800 m, was deposited during the Middle Ordovician on a shallow anoxic marine environment (Laubacher 1978; Rodriguez et al. 2021). This formation is composed of a series of ampelitic, pyrite-rich, black shale and thin, alternating levels of light sandstone, which gives it a flyschoid appearance (Laubacher 1978). The contact with the overlying Sandia Formation is through reverse faults or angular unconformity (Rodriguez et al. 2021). The **Sandia Formation** covers most of the Upper Ordovician and is a detrital sequence of quartzite with shale intercalations deposited on a shallow shelf environment (Rodriguez et al. 2021). The Silurian-Devonian deposition in the region is recorded by the **Ananea Formation**, which is >2,500 m in thickness and composed of schistose, finely bedded black shale and quartzite beds towards its roof (Laubacher 1978).

During the Upper Paleozoic-Lower Mesozoic, epicontinental, continental, and marine carbonate and detrital facies were deposited (Laubacher 1978). In the Oriental Cordillera, the Upper Paleozoic units rest in strong angular unconformity on the aforementioned Lower Paleozoic units (Laubacher 1978). Newell (1949) and Newell et al. (1953) defined three lithostratigraphic units: the Carboniferous Ambo and Tarma groups, and the Permian Copacabana Group (Fig. 8). The Mississippian **Ambo Group** comprises a continental sequence with marine intercalations embracing detrital (quartzous to grey-green sandstone) and shale beds and the Pennsylvanian **Tarma Group** is made up of epicontinental marine deposits of green sandstone, shale, and fossil-bearing limestone (Newell 1949; Newell et al. 1953; Laubacher 1978; De la Cruz et al. 1996; Rodriguez et al. 2021). The Lower Permian

Copacabana Group comprises epicontinental marine carbonate deposits (Newell 1949; Newell et al. 1953; Laubacher 1978; Rodriguez et al. 2021).

Lower Mesozoic sedimentary deposits in the area are represented by the **Mitu Group**, which is made up of continental siliciclastic and volcanic deposits (Newell 1949; Newell et al. 1953; Laubacher 1978). This lithostratigraphic unit is >2,000 m thick and composed of red, siliciclastic rocks intercalated with basaltic to andesitic alkaline lava flows with an intraplate signature (Kontak et al. 1990a; Spikings et al. 2016; Rodriguez et al. 2021). Geochronological U-Pb zircon data by Spikings et al. (2016) constrain the sedimentation of the Mitu Group between ca. 245 and 220 Ma (i.e., Middle to Late Triassic).

Areally restricted outcrops of Cretaceous sedimentary sequences in the Macusani Structural Zone belong to the Muni, Huancané, Viluyo, Ayabacas, and Vilquechico formations (Fig. 9; Rodriguez et al. 2021). The **Muni Formation**, assigned to the Upper Jurassic – Lower Cretaceous, is made up of 0.1 to 0.5 m strata of fine-grained, reddish-brown sandstone with intercalations of red shale (Rodriguez et al. 2021). The **Huancané Formation**, assigned to the Lower Cretaceous by Rodriguez et al. (2021), is described as a sequence of massive, white sandstone in places intercalated with shale (Newell 1949) and deposited in fluvial (upper section) and eolian (lower section) environments. The **Viluyo Formation**, assigned to the Lower Cretaceous (Rodriguez et al. 2021), is described as a sequence of arkosic or quartz sandstone (López 1996). Its contact with the overlying Ayabacas Formation corresponds to an angular unconformity (Rodriguez et al. 2021). The **Ayabacas Formation**, assigned to the Turonian-Coniacian by Callot (2008), is made up of gray packstone deposited in an unstable shelf marine environment (Rodriguez et al. 2021). The **Vilquechico Formation**, defined as greenish or gray pelitic sequences (Newell 1949) deposited in a fluvial environment with floodplains (Rodriguez et al. 2021). The Eocene **Muñani Formation** is mapped as a very small

outcrop to the south of the Cayconi Volcanic Field in the Macusani Structural Zone. It comprises thinly bedded lacustrine facies of red pelite, limestone, and sandstone (Sempere et al 2004).

In the Cordillera de Carabaya, Late Triassic intrusive plutons include Coasa, Aricoma, Limacpampa, Limbani, and San Gabán, and Early Jurassic intrusive rocks are found in the Allincapac complex (Fig. 3). The Triassic plutons correspond to metaluminous to weakly peraluminous monzogranites and granodiorites (Kontak et al. 1990a). **Allincapac** is a peralkaline complex composed of syenitic plutons (Kontak et al. 1990a, Mišković et al. 2009; Rodriguez et al. 2021).

In the Macusani Structural Zone, a series of intervening intermontane basins, including Macusani, Crucero, and Ananea – Ancocala, are partially filled with Middle Tertiary to Quaternary deposits (Fig. 3; Laubacher et al. 1988; Sandeman et al. 1997). Sandeman et al. (1996) grouped Oligocene and Miocene sedimentary and volcanic rocks in these basins under the Picotani and Quenamari groups of the Crucero Supergroup (Figs. 8-9). The Upper Oligocene-lowermost Miocene **Picotani Group** emplaced over the brief ca. 26-22 Ma interval and is composed of a diverse assemblage of lavic and pyroclastic rocks, including lamprophyres, medium- to high-K-calc-alkaline basalts, shoshonites, and S-type rhyodacites (Sandeman et al. 1997). It was subdivided by Sandeman et al. (1997) into nine formations: Cerro Sumpiruni, Puculacaya, Lago Perhuacarca, Cerro Cancahuine, Jama Jama, Pachachaca, Suratira, Cerro Huancahuancane, and Cerro Queuta. The Lower to Upper Miocene **Quenamari Group** is entirely made up of volcanic and volcano-sedimentary strata emplaced between ca. 17 and 6.5 Ma. It comprises silicic, strongly peraluminous suites of biotite + sillimanite ± muscovite ± andalusite ± tourmaline – bearing pyroclastic units and is subdivided into three formations: Huacchane, Quebrada Escalera, and Macusani (Sandeman et al. 1997). In addition,

Sandeman et al. (1997) grouped cospatial hypabyssal units under the Crucero Intrusive Supersuite. This supersuite includes the Quenamari and the Picotani intrusive suites, which are cogenetic with the homonymous volcanic groups of the Crucero Supergroup.

3.3. Geology of the Macusani Volcanic Field

The Macusani Volcanic Field is situated in southeastern Peru, within the Puno Department. The Macusani Volcanic Field is largely exposed in the Quenamari Meseta, a plateau at an altitude of ~4,400 m.a.s.l. In this volcanic field, rocks of the Crucero Supergroup of Sandeman et al. (1997) are dominated by those of the Quenamari Group, whereas rocks of the Picotani Group are volumetrically subordinate. Intrusive units of the Quenamari Intrusive Suite are also exposed in the Macusani Volcanic Field.

Picotani Group

In the Macusani Volcanic Field, rock units of the Picotani Group include the Cerro Sumpiruni, Puculacaya, and Lago Perhuarcarca formations (Fig. 9), which are described below based in the work of Sandeman et al. (1997).

- The **Cerro Sumpiruni Formation** is a sequence of peraluminous, greyish-green, cordierite and biotite-bearing, rhyodacitic-to-rhyolitic ash-flow tuff. $^{40}\text{Ar}/^{39}\text{Ar}$ step heating analysis yielded total-gas integrated dates of 24.13 ± 0.11 Ma and 24.00 ± 0.25 Ma. A mixed sanidine-plagioclase mineral separate yielded a plateau date of 21.71 ± 1.01 Ma, which is interpreted as the time of eruption of this unit.
- The **Puculacaya Formation** consists of intercalated series of olivine and plagioclase-phyric, high-K calc-alkaline, basaltic andesite flows and peraluminous, cordierite-biotite, rhyodacitic ash-flow tuff. The mafic flows are locally mantled by muscovite-biotite \pm andalusite-phyric rhyolitic ash-flow tuff of the Upper Miocene Macusani

Formation. Whole-rock $^{40}\text{Ar}/^{39}\text{Ar}$ dating on a shoshonite gave an integrated date of 21.90 ± 1.68 Ma, and a plateau date of 22.29 ± 1.43 Ma.

- The **Lago Perhuacarca Formation** embraces flows of intermediate composition interbedded with rhyodacitic-rhyolitic ash-flow tuff. The intermediate lavas are metaluminous to peraluminous and resulted from incomplete mixing of minette and cordierite + biotite-bearing silicic melts (Sandeman and Clark 1993). Whole-rock $^{40}\text{Ar}/^{39}\text{Ar}$ analysis on andesite yielded a plateau date of 23.28 ± 0.50 Ma. Biotite $^{40}\text{Ar}/^{39}\text{Ar}$ analysis yielded a plateau and integrated date of 23.86 ± 0.40 Ma.

Quenamari Group

In the Macusani Volcanic Field, the Quenamari Group is represented by the **Macusani Formation** (Fig. 9), which stands as its youngest unit (Sandeman et al. 1997). The Macusani Formation is exclusively exposed in the Macusani Volcanic Field. It comprises a ~500 m-thick sequence of whitish-grey, poorly-consolidated, crystal-rich (around 45%), ash-flow tuff (Cheilletz et al. 1992; Sandeman et al. 1997). It contains a mixture of ash- and lapilli-size pyroclastic fragments, including juvenile pumice and glass fragments and shards and accidental lithic fragments (Sandeman et al. 1997). The mineralogical composition of the Macusani Formation ash-flow tuff comprises quartz, feldspar, biotite, muscovite, sillimanite, andalusite, and tourmaline (Pichavant et al. 1988). Their major element chemistry is relatively uniform and is characterized by strong felsic and peraluminous signatures (Barnes et al. 1970; Noble et al. 1984; Kontak et al. 1984a, b; Pichavant et al. 1988). Further, it is exceptionally enriched in volatile (B, F, Cl) and incompatible lithophile (Li, P, Sn, W, and U) elements (Cheilletz et al. 1992; Sandeman et al. 1997).

Cheilletz et al. (1992) distinguished a Lower Member and an Upper Member in the Macusani Formation associated to two eruptive cycles at 10 ± 1 Ma and 7 ± 1 Ma as dated by

the $^{40}\text{Ar}/^{39}\text{Ar}$ method. In addition, the combination of $^{40}\text{Ar}/^{39}\text{Ar}$ dates and stratigraphic observations led these authors to define six cooling units: i) a 10.0 ± 0.5 Ma cooling unit, recorded in “large-lapilli ash-flow tuff” and “undifferentiated ash-flow tuff” layers; ii) a 7.8 - 8.0 ± 0.1 Ma iii) and a 7.5 ± 0.1 Ma cooling units in “undifferentiated ash-flow tuff”; and iv) 7.3 ± 0.1 Ma, v) 6.8 - 7.0 ± 0.1 Ma, and vi) 6.7 ± 0.1 Ma cooling units in “large-lapilli ash-flow tuff” and “lapilli ash-flow tuff” (Fig. 13). Epiclastic tuff and erosional surfaces were identified between the 7.3 ± 0.1 Ma and 6.8 - 7.0 ± 0.1 Ma cooling units (Cheilletz et al. 1992).

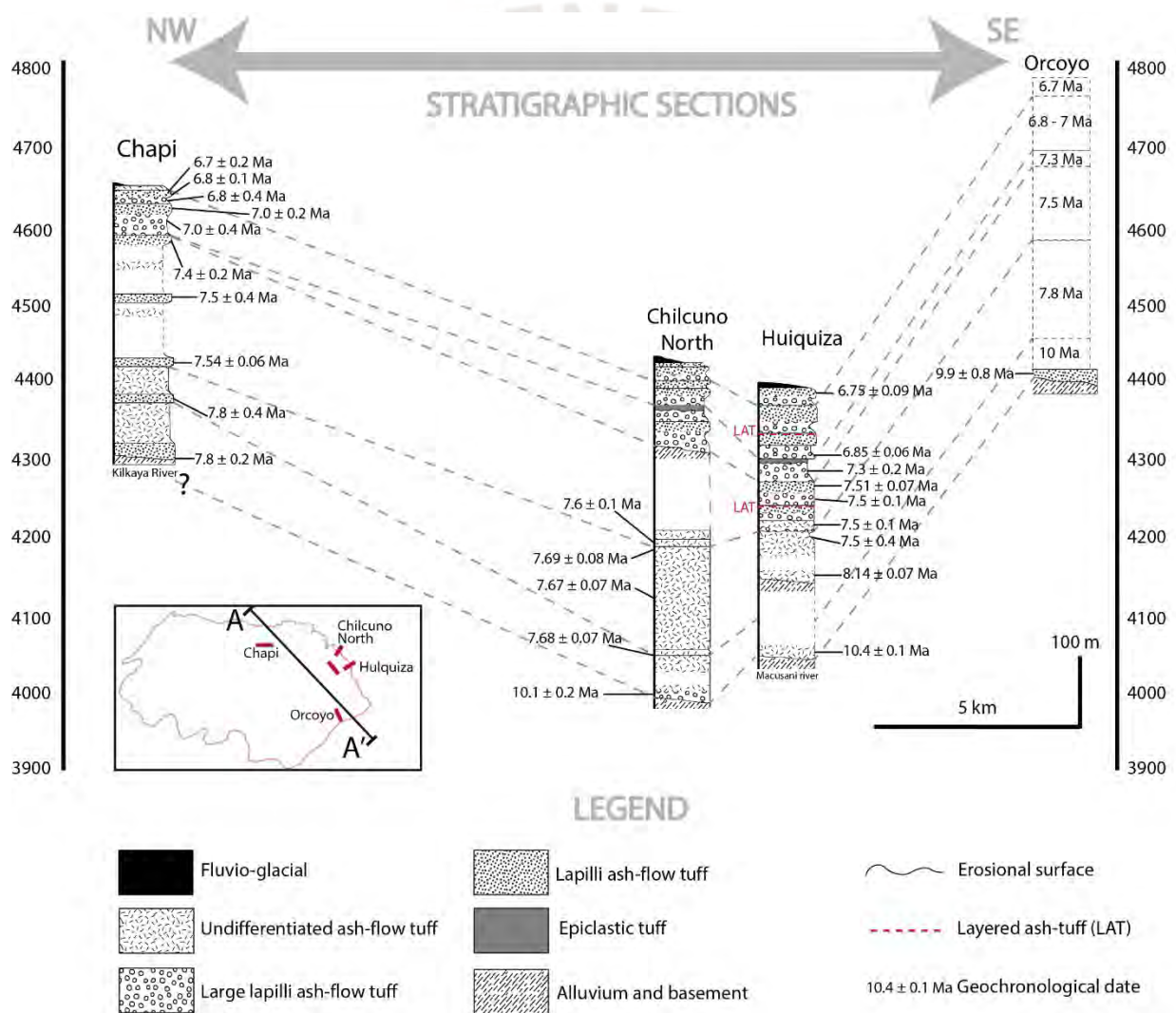


Figure 13. Volcano-stratigraphic correlation chart and $^{40}\text{Ar}/^{39}\text{Ar}$ dates on Macusani Volcanics (Francis, 1959) (equivalent to the later defined Macusani Formation) in Chapi, Chilcuno North, Huiquiza, and Orcoyo sections. Modified from Cheilletz et al. (1992).

López (1996) renamed the Macusani Formation as the Quenamari Formation and subdivided it into the Chacacuniza, Sapanuta, and Yapamayo members based on two intra-formational erosive unconformities and lithomorphostructural characteristics of the tuff levels. The characteristics of these members are described below according to López (1996):

- The **Chacacuniza Member** comprises poorly stratified rhyolitic tuff with lapilli fragments and crystal clasts of quartz, plagioclase, K feldspar, and biotite that appear along with volcanic glass in a crypto-crystalline matrix. The thickness is variable and reaches ~170 m, with individual 50 to 100 cm-thick layers. It overlies in angular unconformity rocks of the Mitu Group and underlies the Sapanuta Member and, in the NE sector of the 29u sheet (Payacucho-Quisco Punco), the Yapamayo Member.
- The **Sapanuta Member** consists of a thick rhyolitic tuff succession with distinctive columnar jointing. It comprises quartz, K feldspar, plagioclase, and biotite crystal clasts and lithic fragments embedded in a crypto-crystalline matrix. Amygdules are filled by calcedony. The Sapanuta Member unconformably overlies the Mitu Group and the Ananea, Muni, Huancané, Viluyo, and Hanchipacha formations, and conformably overlies the Chacacuniza Member.
- The **Yapamayo Member** is considered the last pyroclastic flow event in the sector and comprises a sequence made up of thick (>3 m) layers of white or greyish-white tuff interspersed with some lapilli tuff beds. The rhyolitic tuff contains quartz, albite, orthoclase, sanidine, biotite, muscovite, and andalusite crystal clasts embedded in a crypto-crystalline matrix.

Based on the observation of outcrops and ~2,000 m of drill cores distributed along fourteen holes at five localities in the NE portion of the Macusani Volcanic Field, Li (2016) has subdivided the Macusani Formation into three units:

- The **Unit A** is the oldest unit and has >35 m in thickness. It occurs in the Nuevo Corani area, where it unconformably overlies metapelites and volcanic rocks of the Paleozoic-Mesozoic basement. Its contact with the overlying Unit B is through an erosional surface with strong kaolinitic alteration. Rhyolitic tuff in Unit A is white to grey, poorly consolidated, and strongly affected by argillic alteration. Its crystal content (20-30 vol.%) is lower in comparison with crystal contents in both Unit B and Unit C, and is dominated by quartz and biotite associated with altered lapilli-sized juvenile clasts.
- The **Unit B** is 175 m thick at Nuevo Corani, where it unconformably overlies both the basement rocks and Unit A. This unit contains white to gray, well-consolidated, fine-grained rhyolitic tuff with a 30-45 vol.% crystal content. Crystal clasts are dominantly of quartz, sanidine, biotite, muscovite, and andalusite. Rock fragments include lapilli-size juvenile clasts (0.5 to 10 cm in size) and lithoclasts of limestone, pelite, quartzite, andesite, and rhyolite.
- The **Unit C** is the youngest of the three units. Its thickness varies from 40 m in the Nuevo Corani area to 70 m in the Tantamaco area. It is separated from Unit B by an unconformity marked by an erosional surface. It comprises brown to grey rhyolitic tuff that is weakly to moderately altered to a phyllic assemblage. Its crystal content is 40-50 vol. % including crystal clasts of sanidine, quartz, biotite, and muscovite. The base of this unit is rich in lapilli-sized juvenile clasts and lithoclasts.

Soberon et al. (2022) have recently described the geology of the Corani quadrangle and correlated the members proposed by López (1996) with those recognized by Li (2016) based on mineralogical and lithological characteristics. In the Corani area, Soberon et al. (2022) correlate the Chacacuniza, Sapanuta, and Yapamayo members of López (1996) with the units A, B, and C of Li (2016), respectively. Figure 14 shows schematic stratigraphic columns for the Neogene sedimentary and volcanic rocks in the Macusani Volcanic Field that were

produced according to the descriptions of Cheilletz et al. (1992), Sandeman et al. (1997), López (1996), and Li (2016).

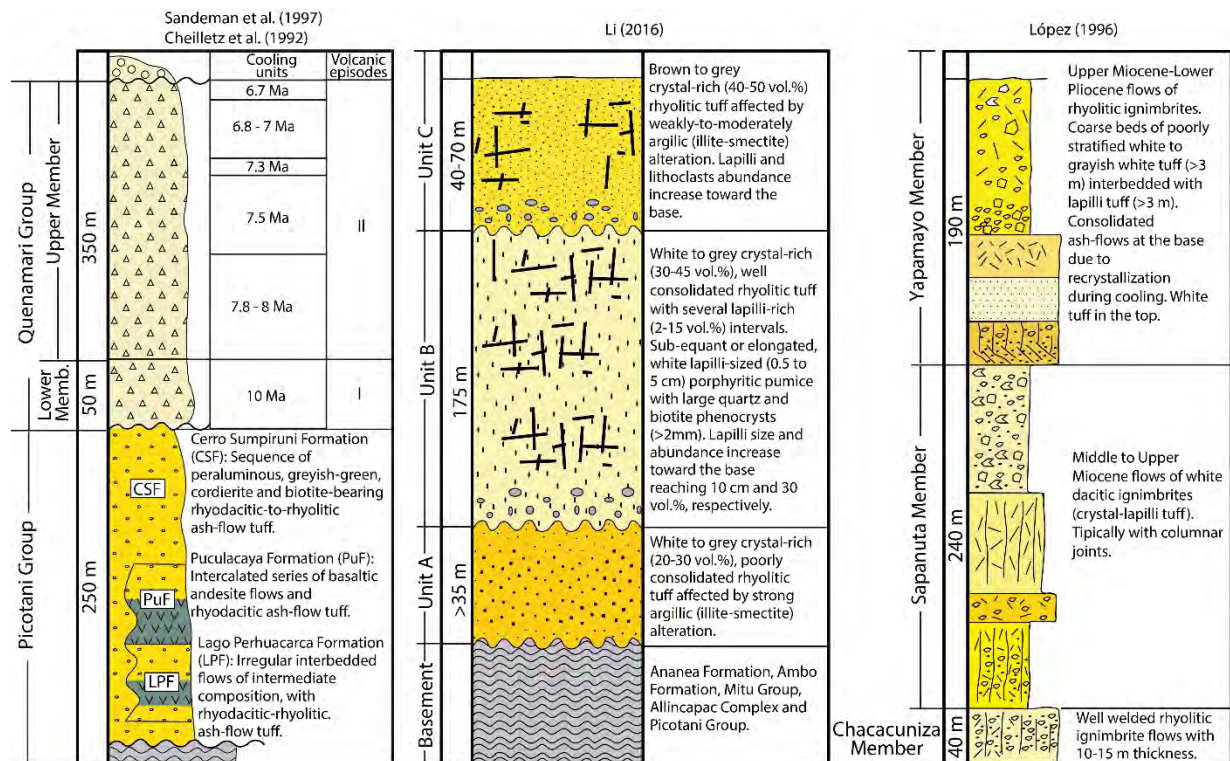


Figure 14. Schematic stratigraphic columns of Neogene volcanic and sedimentary rocks in the Macusani Volcanic Field according to descriptions of Sandeman et al. (1997), Cheilletz et al. (1992), López (1996), and Li (2016).

Quenamari Intrusive Suite

Neogene hypabyssal intrusive rocks exposed in the Macusani Volcanic Field belong to the Quenamari Intrusive Suite of Sandeman et al. (1997) and include the following intrusive bodies:

- The **Quebrada Centilla Stock**, which is a coarsely porphyritic, cordierite-biotite monzogranite that intruded lava flows of the Lago Perhuacarca Formation, and possibly, Cerro Sumpiruni Formation, on the northern and northeastern flanks of Nevado Ollo Quenamari. $^{40}\text{Ar}/^{39}\text{Ar}$ dates (24.09 ± 0.18 Ma and 23.65 ± 0.14 Ma)

support that the Quebrada Centilla Stock is cogenetic with the Lago Perhuacarca Formation (Sandeman et al. 1997).

- The **Ninahuisa Stock**, which is a peraluminous, sanidine-megacrystic, cordierite-biotite monzogranite body exposed over an area of more than 20 km² along the floor of the Ninahuisa valley. ⁴⁰Ar/³⁹Ar dating on sanidine yielded a plateau date of 23.15 ± 0.20 Ma and ⁴⁰Ar/³⁹Ar dating on biotite yielded a plateau date of 23.52 ± 0.58 Ma (Sandeman et al. 1997).
- The **Revancha Dike**, which is ≤ 5 m-wide peraluminous, glassy, cordierite-biotite, rhyodacitic dyke exposed on the southern slope of the Ninahuisa valley. This dike intruded compositionally similar ash-flow tuff and porphyritic granitic rocks and was dated at 24.07 ± 0.09 Ma (⁴⁰Ar/³⁹Ar, biotite; Sandeman et al. 1997).
- The **Chaccaconiza Stock**, which is a syenogranitic body exposed to the eastern part of the rural community of Quelcaya. Magmatic muscovite yielded an ⁴⁰Ar/³⁹Ar date of 7.50 ± 0.50 Ma (Cheilletz et al. 1992), which demonstrates that the Chaccaconiza Stock is coeval with the Upper Member of the Macusani Formation of Sandeman et al. (1997).
- The **Cerro Cayo Orjo Plug**, which is a set of sub-volcanic rhyolitic necks, plugs, and lopoliths exposed to the south of Collpa settlement. Many of these bodies exhibit flow textures, columnar jointing, and display massive rhyolitic cores and sheaths of intrusion breccia containing up to 30% of country-rock xenoliths in a rhyolitic matrix (Sandeman et al. 1997).
- The **Nevado Olló Quenamari Plug**, which is a sanidine-quartz-biotite-phyric intrusion exposed on southern part of Lago Perhuacarca. ⁴⁰Ar/³⁹Ar dating on sanidine yielded a plateau date of 12.14 ± 0.11 Ma (Sandeman et al. 1997).

4. RESULTS

4.1. Textural description of the dated rock samples

The textures of the nine samples selected for this thesis were analyzed macroscopically. The samples of Lithium-rich Tuff can be grouped into two textural groups. The first textural group includes the samples 2021-MAC-08A, 2021-MAC-11B, 2021-MAC-038, and 2021-MAC-048 (Figs. 15a-d) and is characterized by a fine lamination and variable proportions of cavities. The lamination is defined by mm-scale, regularly stacked, white, gray, and orange-beige laminae. Intercalated planar, wavy, and convoluted-slumped levels suggest plastic deformation synchronous to deposition. The cavities are globular to very irregular in shape and have sizes comprised mostly between 2 mm and 2 cm. The long axes of the cavities are parallel to the general rock lamination and their abundance often varies along different sedimentary levels. The second textural group includes the sample 2021-MAC-025 (Fig. 15e), which lacks the characteristic lamination of the first textural group and is rather composed of a massive, white matrix. All the studied samples of Lithium-rich Tuff have a hyalocrystalline, very fine-grained matrix that hosts matrix-supported, unevenly distributed, medium to coarse ash-grained, subhedral, dark brown to black mica crystal clasts. Both textural groups of Lithium-rich Tuff can be classified as tuffaceous mudstone.

The samples of brecciated tuff (2021-MAC-005, 2021-MAC-006, and 2021-MAC-031) comprise clast-supported, hyalocrystalline, angular to sub-rounded, irregularly shaped, internally laminated, mud size grained, pale cream clasts embedded in a darker matrix composed of a mud size hard material (Figs. 15f-h). The size of the clasts range mostly between 2 mm and 1 cm. Mica crystal clasts are present in both the matrix and clasts and are medium ash-sized, subhedral, and dark brown to black.

Finally, the sample of white tuff (2021-MAC-067) from the former San Vicente White concession is a massive, pale, crystal-rich, tuffaceous mudstone (Fig. 15i). The crystal clasts are matrix-supported and comprised mostly of quartz, feldspar, and biotite. Quartz crystal clasts are smoky, euhedral, bipyramidal, coarse ash- to fine lapilli-sized (up to 4.5 mm). Feldspar crystal clasts are white, euhedral, prismatic, and fine lapilli in size. Biotite crystal clasts are euhedral to subhedral, partially or completely oxidized, and show two distinct size populations: fine ash, and medium ash (up to 1.6 mm). This sample also has scarce, subhedral, pinkish, ash-sized (<1 mm) muscovite and black, euhedral, prismatic, ash-sized (<0.1 mm in length) tourmaline crystal-clasts.

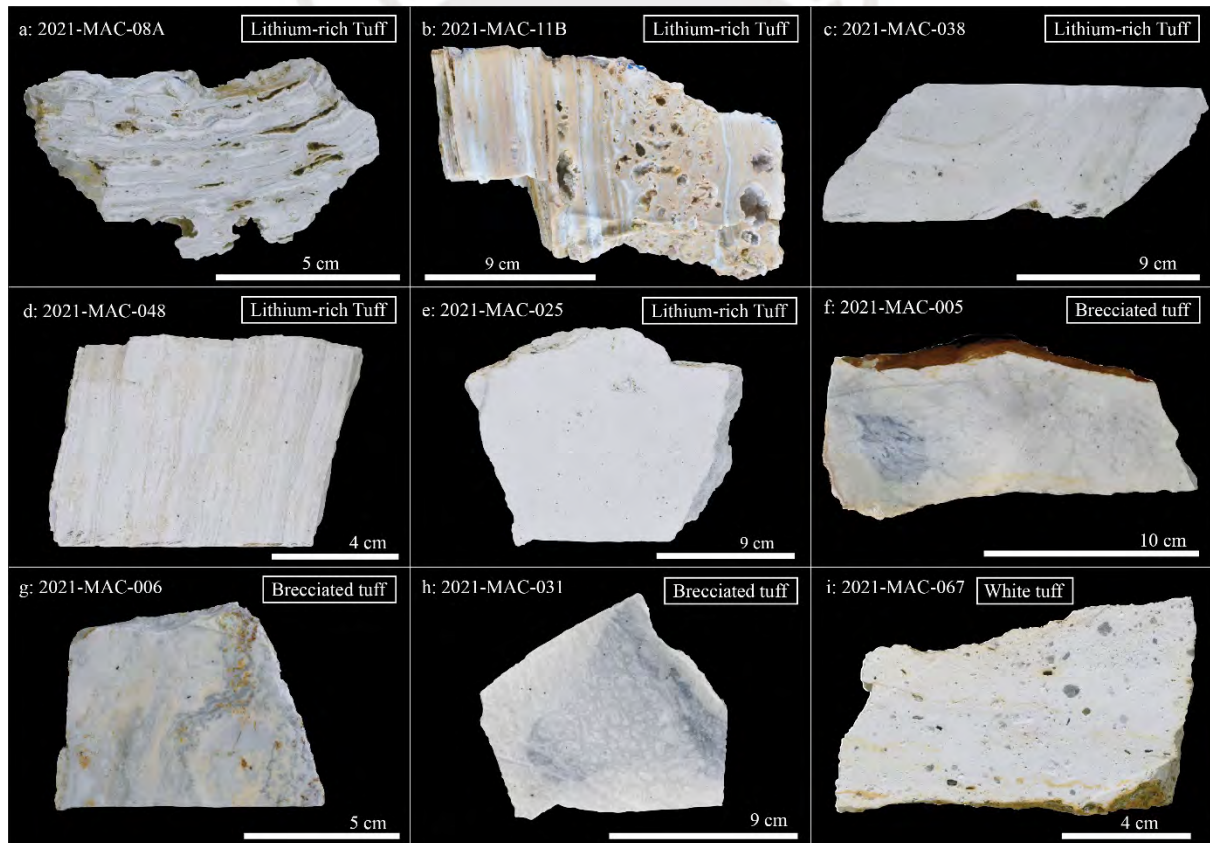


Figure 15. Dated samples of Lithium-rich Tuff (**a-e**) and brecciated tuff (**f-h**) from the Falchani Lithium Project and of white tuff from the former San Vicente White concession (**i**) in the Macusani Volcanic Field.

4.2. $^{40}\text{Ar}/^{39}\text{Ar}$ results

The obtained $^{40}\text{Ar}/^{39}\text{Ar}$ results on micas from Lithium-rich Tuff, brecciated tuff, and white tuff are presented in Appendix D, Table 2, and Figures 16-19. $^{40}\text{Ar}/^{39}\text{Ar}$ analyses of mica from Lithium-rich Tuff yield plateau dates in the range between $8,978 \pm 73$ ka and $8,717 \pm 44$ ka, and inverse isochron dates in the range between $10,327 \pm 612$ ka and $8,743 \pm 52$ ka (Figs. 16). The plateau date for the sample 2021-MAC-048 ($8,978 \pm 73$ ka), which is the oldest among all the analyzed samples, does not overlap with plateau dates for the other samples of Lithium-rich Tuff taking into account their respective analytical errors (Fig. 19). Hence, a time span of ca. 261 kyr between the oldest and the youngest (2021-MAC-038) plateau dates on Lithium-rich Tuff samples can be calculated.

Micas from brecciated tuff yielded plateau dates comprised between $8,823 \pm 9$ ka and $8,815 \pm 16$ ka, and isochrone dates in the range between $9,045 \pm 244$ ka and $8,820 \pm 21$ ka (Fig. 17). These dates overlap with each other considering their analytical errors (Fig. 19).

Finally, micas from the white tuff from the former San Vicente White concession produced an irregular age spectrum, precluding the calculation of plateau or isochrone dates. The lowest-temperature step (500°C) defines a date of 8.93 ± 3.67 Ma, and the highest-temperature step ($1,400^\circ\text{C}$) yields a date of 17.36 ± 1.61 Ma (Fig. 18).

Micas extracted from brecciated tuff yielded systematically younger dates, by ca. 160 kyr, than the oldest micas from Lithium-rich Tuff (i.e., sample 2021-MAC-048). In contrast, the brecciated tuff is generally older (by at least ca. 47 kyr) than the rest of the samples of Lithium-rich Tuff, with the exception of a small overlap with the sample 2021-MAC-11B taking into account the respective analytical errors (Fig. 19).

Table 2. $^{40}\text{Ar}/^{39}\text{Ar}$ analytical data for micas separate on Lithium-rich Tuffs, Macusani Volcanic Field, Oriental Cordillera, Peru

Sample	Results	40(a)/36(a)	$\pm 2\sigma$	40(r)/39(k)	$\pm 2\sigma$	Date (ka)	$\pm 2\sigma$	MSWD	$^{39}\text{Ar}(k)$ (%,n)	K/Ca	$\pm 2\sigma$
2021-MAC-005 (Brecciated tuff)	P.A. ⁽¹⁾			2.88915	0.00691	8,820	21	0.56	60.90, 6	1,676	545
	I.I. ⁽²⁾	321.78	2.03	2.88916	0.01055	8,820	32	0.99			
2021-MAC-006 (Brecciated tuff)	P.A.			2.89384	0.00281	8,823	9	1.64	86.02, 14	861	405
	I.I. ⁽³⁾	297.34	8.47	2.89718	0.02293	8,833	70	1.90			
2021-MAC-08A (Lithium-rich Tuff)	P.A.			2.83469	0.00872	8,767	27	1.22	99.23; 21	2,570	2,468
	I.I.	297.32	1.03	2.84033	0.00919	8,785	29	1.02			
2021-MAC-11B (Lithium-rich Tuff)	P.A.			2.85710	0.00362	8,788	12	1.50	82.40, 17	844	114
	I.I.	297.22	1.27	2.86486	0.00814	8,812	25	1.39			
2021-MAC-025 (Lithium-rich Tuff)	P.A.			2.83342	0.00733	8,741	23	0.92	85.14, 15	347	337
	I.I.	300.87	6.67	2.82878	0.01559	8,727	48	0.96			
2021-MAC-031 (Brecciated tuff)	P.A.			2.87396	0.00522	8,815	16	0.65	53.46, 9	1,745	378
	I.I. ⁽⁴⁾	272.63	27.48	2.94925	0.07984	9,045	244	0.30			
2021-MAC-038 (Lithium-rich Tuff)	P.A.			2.81709	0.01435	8,717	44	1.58	93.55, 19	395	182
	I.I.	297.37	1.44	2.82545	0.01688	8,743	52	1.45			
2021-MAC-048 (Lithium-rich Tuff)	P.A.			2.91453	0.02374	8,978	73	1.60	74.88, 17	557	152
	I.I.	249.57	22.28	3.35346	0.19926	10,327	62	0.63			
2021-MAC-067 ⁽⁵⁾ (White tuff)	T.F.A. ⁽⁶⁾			2.02352	0.01040	6.16 ⁽³⁾	0.03		26	144	6

(1) P.A.: Plateau Age.

(2) I.I.: Inverse Isochron.

(3) Data define an error-chron date (i.e., data possess scatter in excess of experimental error (i.e., geological error); Brooks et al. 1972).

(4) Data define an overestimated error date.

(6) Plateau and isochron dates cannot be calculated for the sample 2021-MAC-067.

(6) T.F.A: Total Fusion Age.

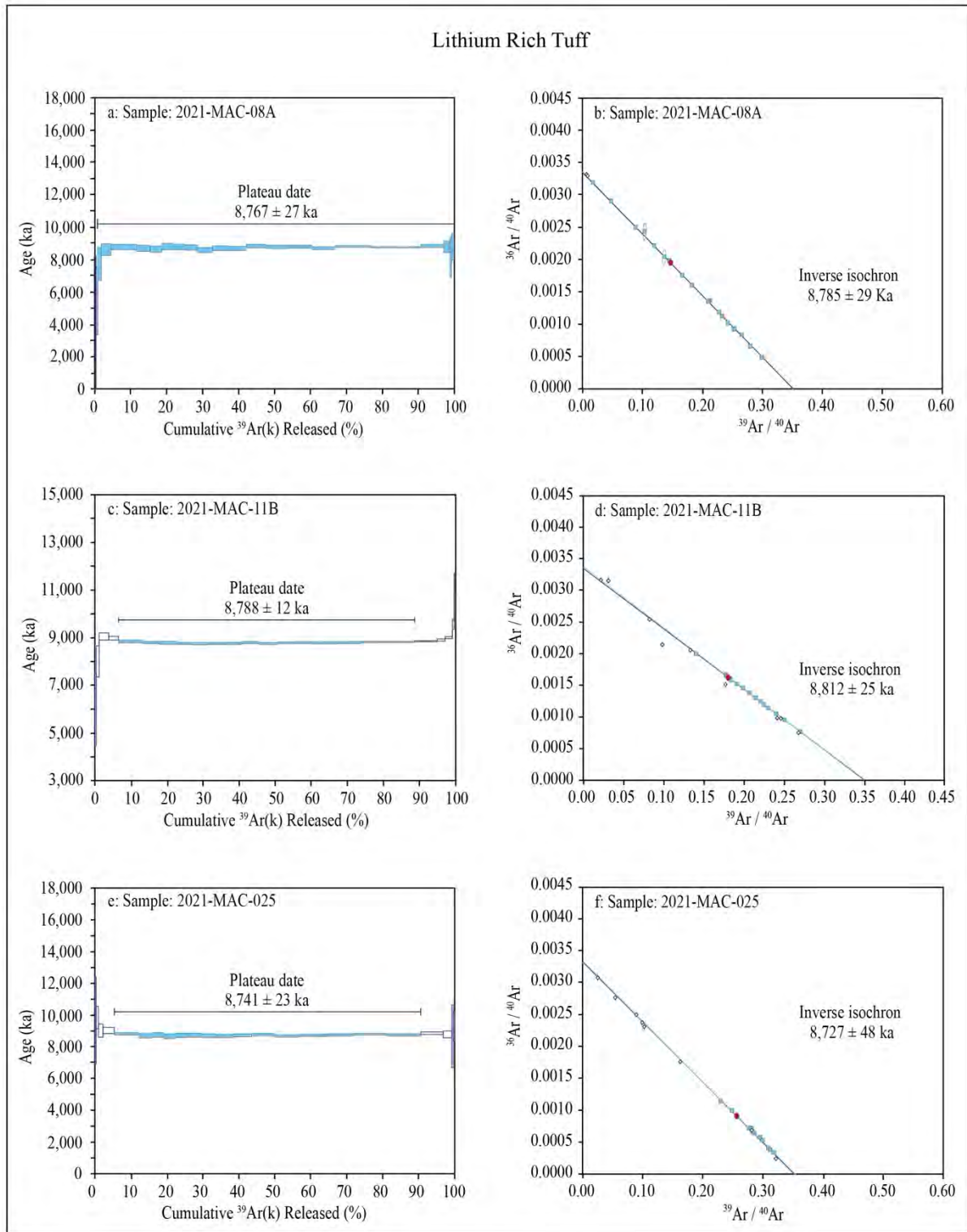


Figure 16. $^{40}\text{Ar}/^{39}\text{Ar}$ step heating profiles and inverse isochron diagrams for Lithium-rich Tuff samples from the Macusani Volcanic Field.

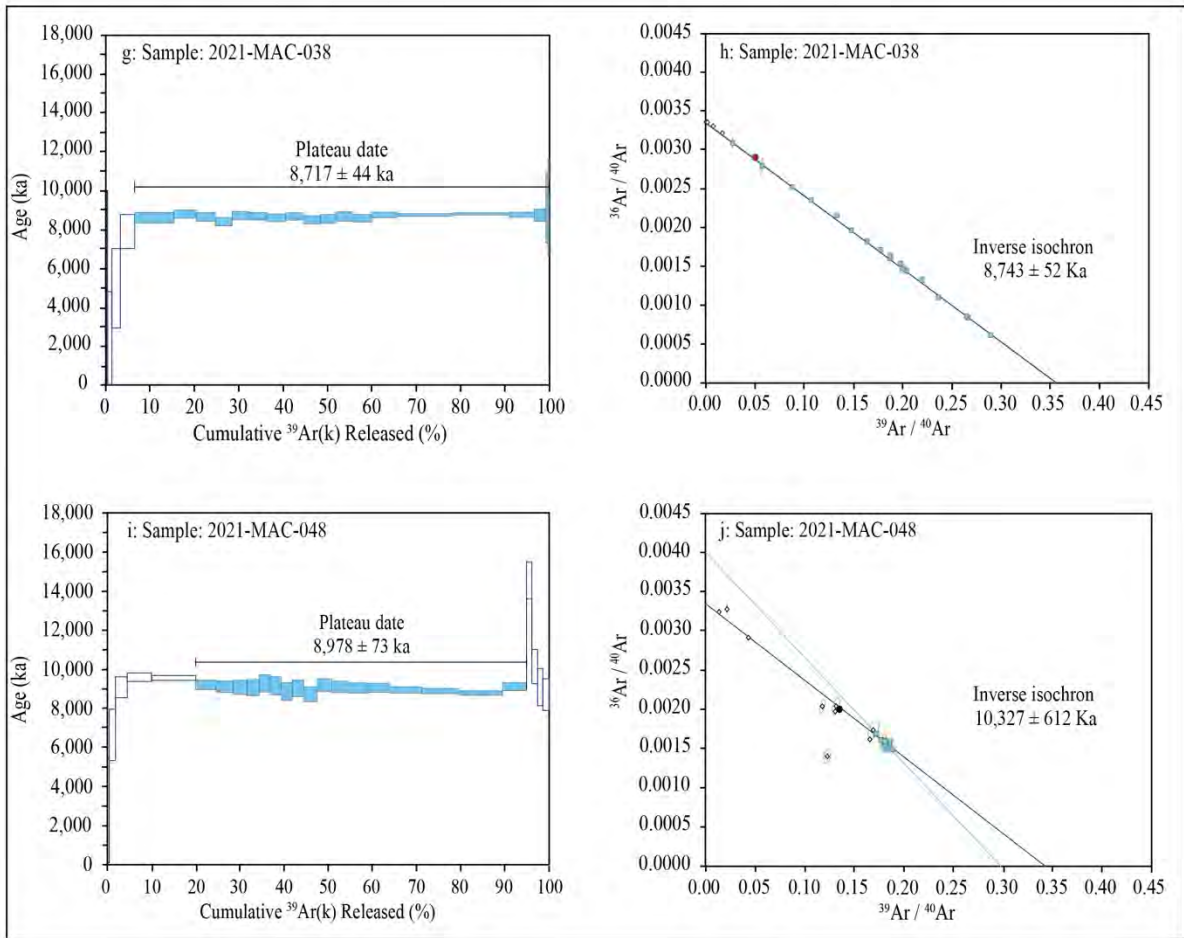


Figure 16. (Continued)

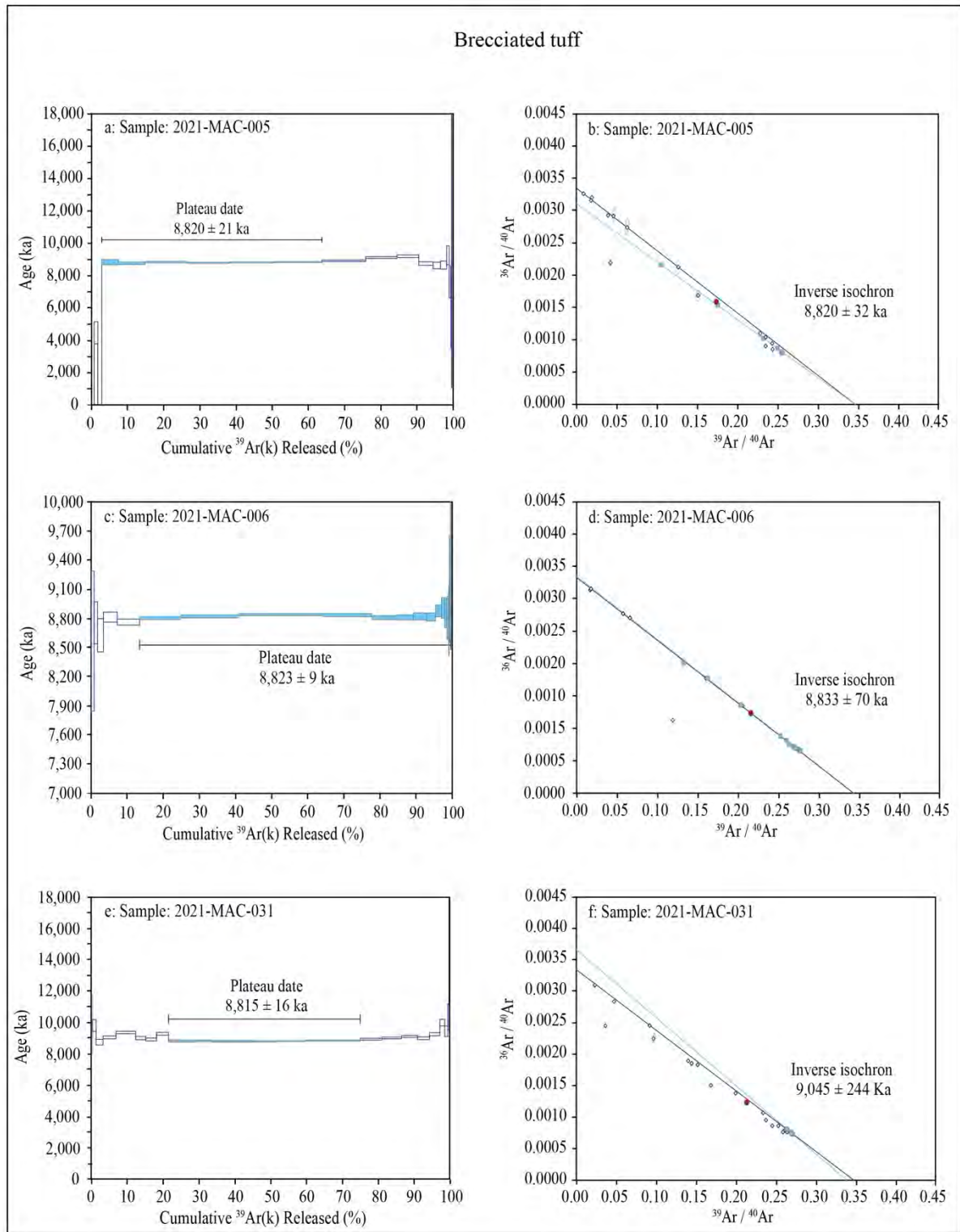


Figure 17. $^{40}\text{Ar}/^{39}\text{Ar}$ step heating profiles and inverse isochron diagrams for brecciated tuff samples from the Macusani Volcanic Field.

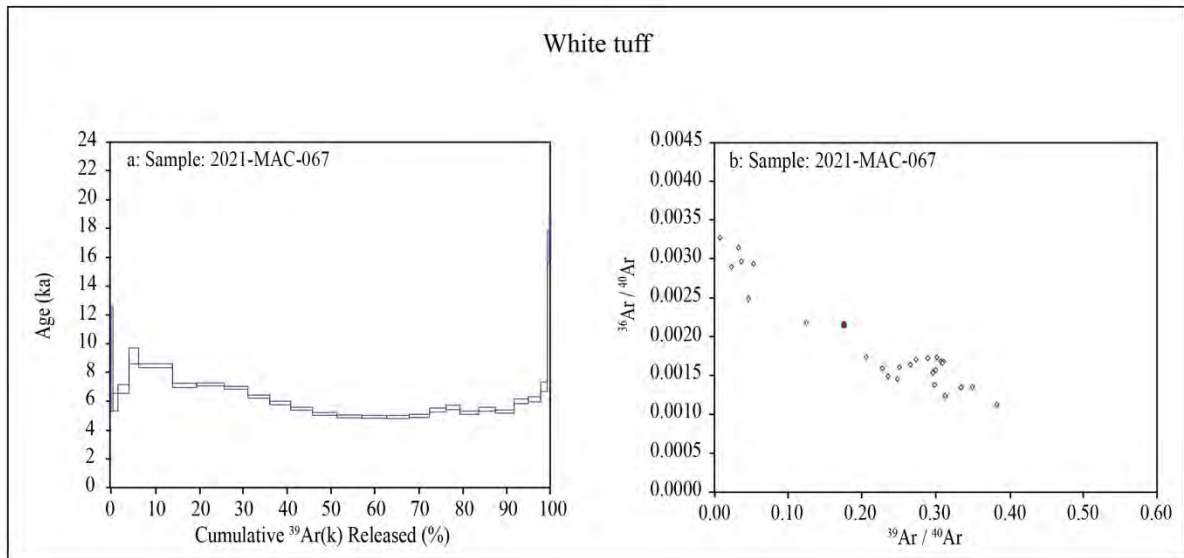


Figure 18. $^{40}\text{Ar}/^{39}\text{Ar}$ step heating profile and inverse isochron diagram for the white tuff from the former San Vicente White concession in the Macusani Volcanic Field.

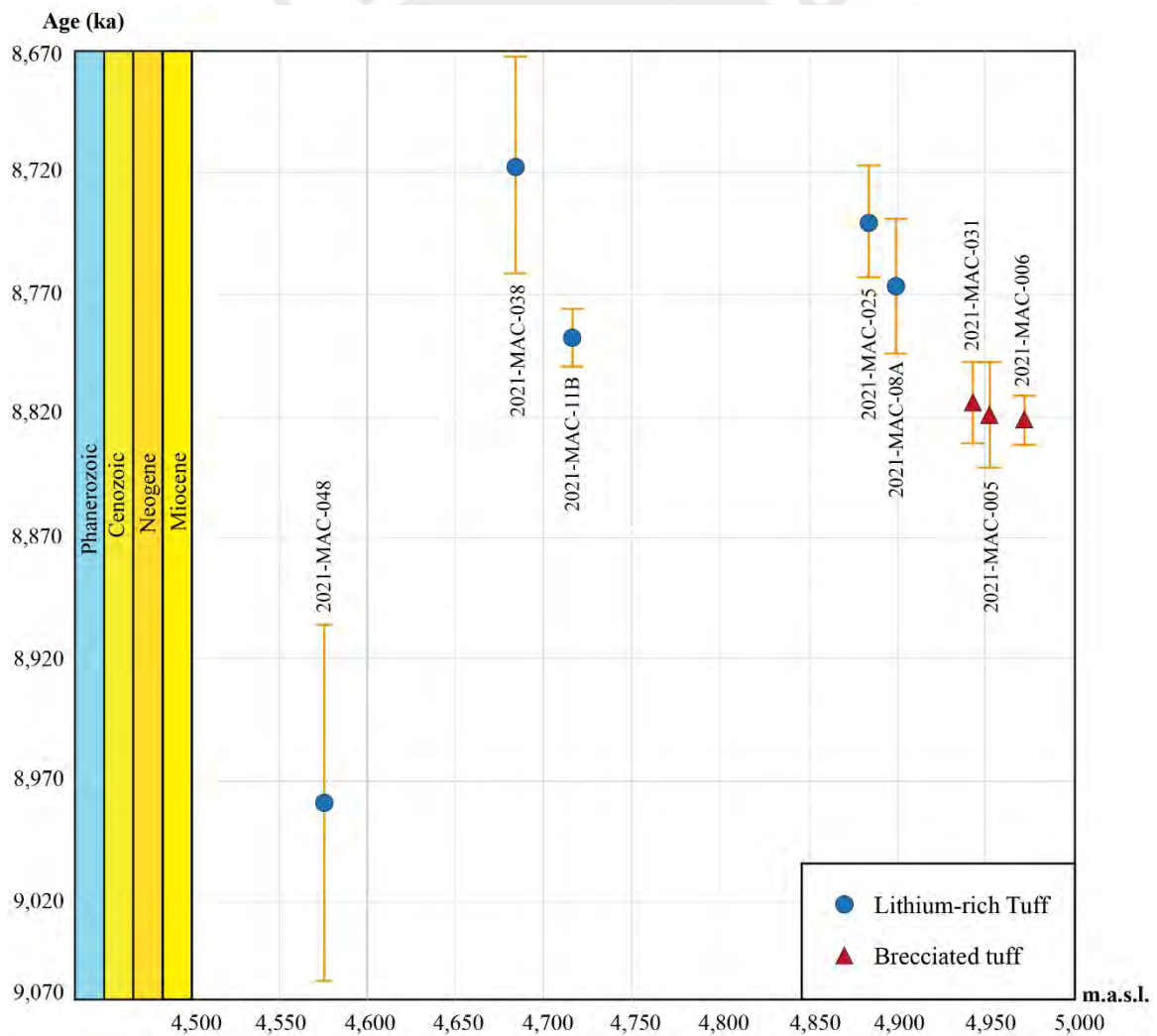


Figure 19. Geochronological chart of $^{40}\text{Ar}/^{39}\text{Ar}$ plateau dates on mica separates from the Macusani Volcanic Field analyzed in this thesis sorted according to their sampling elevation.

5. DISCUSSION

5.1. Deposition duration and rate of the Lithium-rich Tuff

The obtained dates on mica crystal clasts from Lithium-rich Tuff are in the range from $8,978 \pm 73$ ka to $8,717 \pm 44$ ka, with a total difference of 261 kyr. Considering the respective analytical errors, the age difference could be within the range of 144 kyr to 379 kyr (Fig. 19). Since the dated mica grains are crystal clasts in tuffaceous mudstone, the obtained dates constrain the timing of mica formation or cooling, and represent maximum depositional ages of the tuffaceous mudstone.

The oldest mica date in Lithium-rich Tuff was on the sample 2021-MAC-048, which was extracted at an elevation of 4,576 m.a.s.l., i.e., at a lower altitude than the other four samples of Lithium-rich Tuff, which yielded dates in the range between $8,788 \pm 12$ ka and $8,717 \pm 44$ ka (Fig. 19). Amongst these later four samples, the youngest one (2021-MAC-038) was extracted at an altitude of 4,684 m.a.s.l. in the drillhole PCHAC 01-TSW(1), while the others were picked up at surface at altitudes ranging from 4,716 to 4,899 m.a.s.l. In the case of the samples 2021-MAC-038 and 2021-MAC-011B, which were collected from nearby locations (Fig. 11), the $^{40}\text{Ar}/^{39}\text{Ar}$ mica dates exhibit a difference of ca. 71 kyr considering central values and comprised between 15 and 127 kyr considering the analytical errors associated with the data. The fact that the sample 2021-MAC-038 yielded the youngest date despite coming from a lower elevation than the sample 2021-MAC-011B precludes any direct correlation between altitudes and dates. This may be attributed to a number of factors including the paleorelief during sedimentation, sedimentary redistribution of magmatic micas, and/or later tectonic deformation. Tectonic model restitution, currently underway in the context of a Master's thesis (J. Ramirez and L. Torró personal communication), will be necessary to further elucidate this. The aforementioned observations do not permit differentiation at this stage between the

hypotheses that the Lithium-rich Tuff was deposited as a single or multiple volcano-sedimentary events.

The Lithium-rich Tuff unit has a thickness that ranges from 50 to 140 m (The Mineral Corporation 2019). The difference in altitude between the shallowest (4,899 m.a.s.l.) and deepest (4,576 m.a.s.l.) samples of Lithium-rich Tuff is considerably higher, reaching 323 m. This further supports the conclusion that the vertical distribution of the dated Lithium-rich Tuff samples is not a valid constraint of the original thickness of this unit nor their deposition in a single vs. multiple events. The original thickness of the Lithium-rich Tuff is therefore unknown and the best approximation is the constraint made by The Mineral Corporation (2019) based on real thicknesses measured in drill cores (50 to 140 m). Given the aforementioned thickness range, and assuming that the time span between the oldest and youngest dates can be a rough constraint of the deposition duration, a single deposition event would have resulted in a deposition rate between 0.13 mm/year (equivalent to a thickness of 50 m and a maximum time span of 379 kyr) and 0.97 mm/year (equivalent to a thickness of 140 m and a minimum time span of 144 kyr). These rates are comparable to those calculated in recent lakes (e.g., Robbins and Edgington 1975; Patterson et al. 1996; Colman et al. 2004). As the original thickness prior to compaction by burial (load pressure) cannot be calculated with the available data (cf. Riehle et al. 2010), these rates represent minimum values.

It is notable that the dates obtained on micas from brecciated tuff, in the range from $8,823 \pm 9$ ka to $8,815 \pm 16$ ka, are intermediate between the oldest and youngest Lithium-rich Tuff samples, with only a near-negligible overlap of <1 kyr with the date obtained on micas from the sample 2021-MAC-11B (Fig. 19). They are 156 kyr younger and 98 kyr older than the oldest and youngest Lithium-rich Tuff samples, respectively, based on central values. This suggests that the brecciated tuff formed during a brief period between the deposition of more

massive or laminated Lithium-rich Tuff. The brecciated samples are characterized by hosting laminated tuff clasts that exhibit textural similarity to Lithium-rich Tuff. Accordingly, the brecciated tuff could represent a specific stage of deposition in which brecciation of wet tuffaceous mudstone was facilitated. On the other hand, the fact that brecciated tuff samples were collected at the highest altitude amongst all dated rock samples (Fig. 19) could be explained by basin paleorelief features or later tectonic deformation. The lack of stratigraphic correlation between the sampled brecciated tuff and Lithium-rich Tuff precludes constraints on these questions.

5.2. Stratigraphic and tectono-magmatic contextualization of the Lithium-rich Tuff

The formation and/or cooling of mica crystal clasts and their subsequent deposition in tuffaceous mudstone of the Lithium-rich Tuff and other related lithologies, such as brecciated tuff, occurred over a relatively short time span, between $8,978 \pm 73$ ka and $8,717 \pm 44$ ka. As anticipated, this temporal interval coincides with the deposition of the Macusani Formation of the Quenamari Group, which occurred between ca. 10 and 6.5 Ma (Fig. 20; Sandeman et al. 1997). Cheilletz et al. (1992) constrained two eruption episodes on tuff from the "Macusani ignimbrite field" (i.e., prior to the formal definition of the Macusani Formation by Sandeman et al. 1997) at 10 ± 1 Ma and 7 ± 1 Ma (Fig. 14). The newly determined dates for the Lithium-rich Tuff, at ca. 8.9-8.7 Ma, fall between the two identified volcanic cycles. Furthermore, the new dates do not overlap with any of the fundamental cooling units that had been identified by these authors within the Macusani Formation. It is also worth noting that the new dates on mica from the Lithium-rich Tuff do not coincide with dates on macusanite, which were erupted during three episodes at 7 ± 1 Ma, 5.7-5.3 Ma, and 4.8-4.3 Ma (Poupeau et al. 1993), nor intrusive units in the Macusani Volcanic Field (Figs. 20-22).

In the other volcanic fields within the Macusani Structural Zone, no volcanic, volcanoclastic, or intrusive units of equivalent age to the Lithium-rich Tuff, even considering analytical errors, have been reported (Figs. 3, 20, 22). The closest dates were determined on granitic rocks of the Cerro Corimpata stock, which is situated in the Picotani field ~135 km to the southeast of the Falchani Lithium Project (Figs. 20-21).

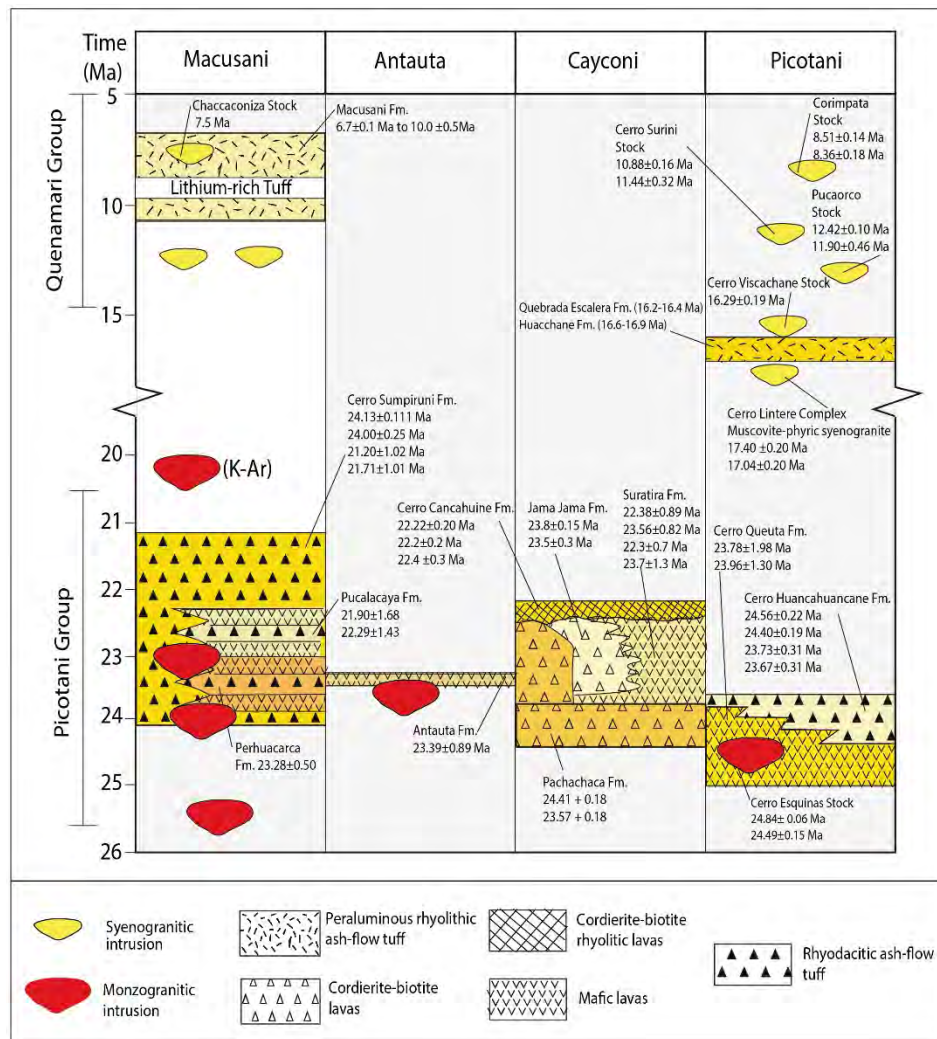


Figure 20. Stratigraphic and geochronological relationships of the volcanic and intrusive rocks in the Quenamari, Antauta, Cayconi, and Picotani fields (modified from Sandeman et al. 1997). The Lithium-rich Tuff has been included in the Macusani Volcanic Field, according to the new dates of 8.8-8.7 Ma.

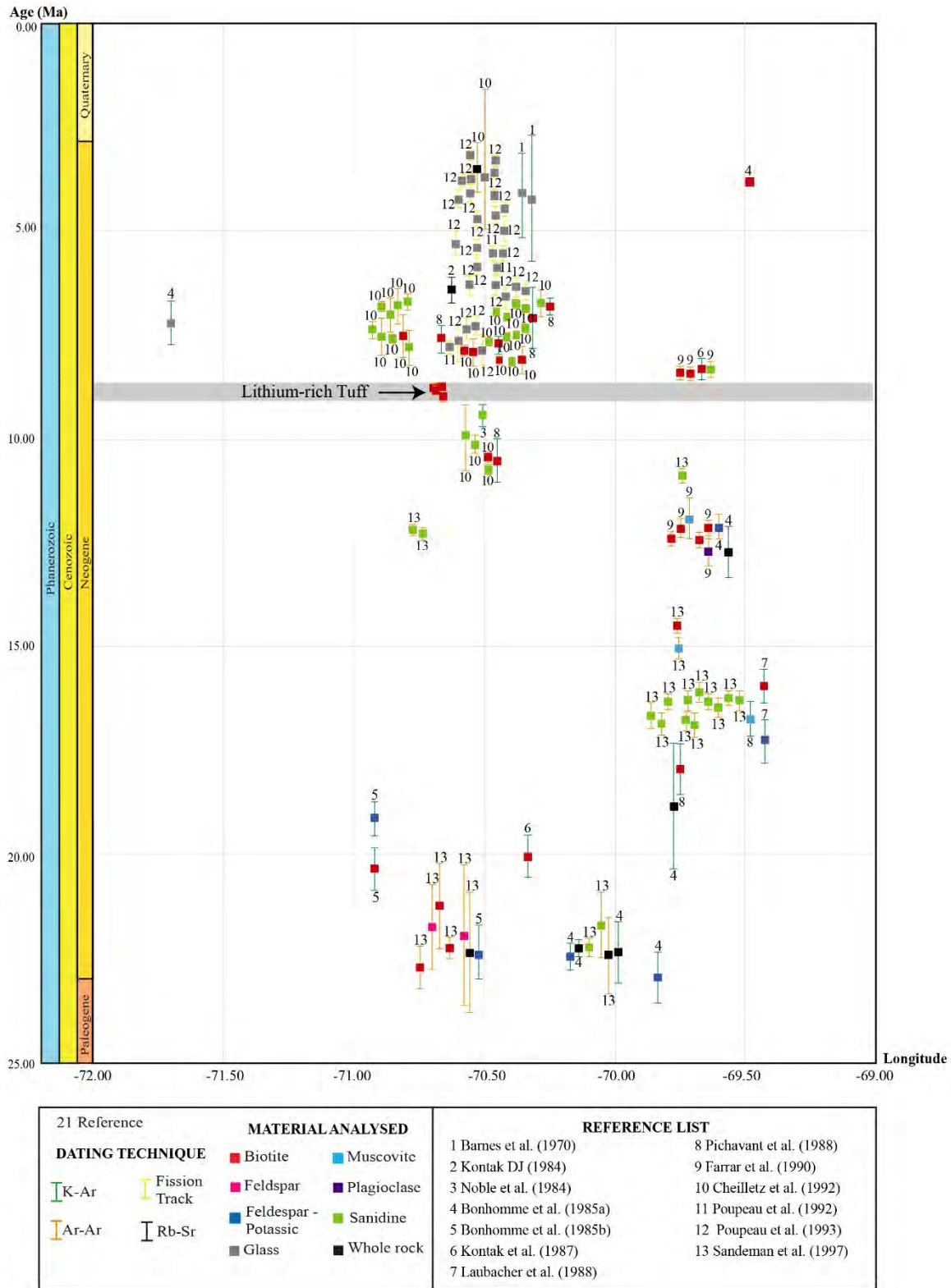


Figure 21. Geochronologic chart of Cenozoic rocks in the Macusani Structural Zone and Cordillera de Carabaya, including the new $^{40}\text{Ar}/^{39}\text{Ar}$ mica dates on Lithium-rich Tuff from the Falchani Lithium Project in the Macusani Volcanic Field.

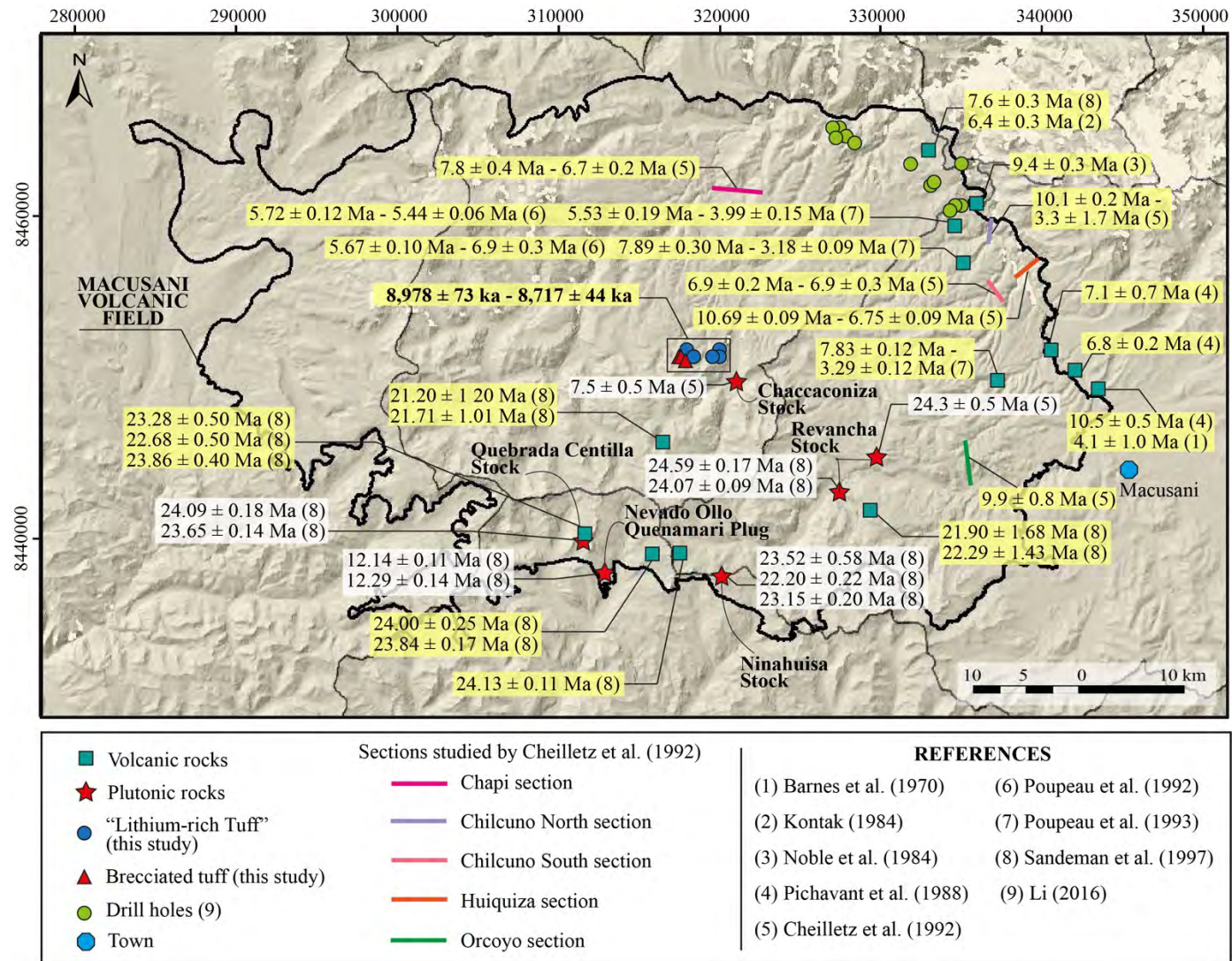


Figure 22. Location of the dated samples of Lithium-rich Tuff and brecciated tuff (this study) and other samples dated by previous authors in the Macusani Volcanic Field. White boxes contain dates on intrusive rocks, and yellow boxes, on volcanic rocks.

Therefore, the new dates demonstrate that the event that was related to the crystallization and/or cooling of mica crystal-clasts found in tuffaceous mudstone of the Lithium-rich Tuff in the Falchani Lithium Project coincided with a generalized magmatic lull in the Macusani Structural Zone and neighboring areas in the Eastern Cordillera of the Central Andes in southern Peru.

6. CONCLUSIONS

In this thesis, geochronological dating of mica crystal-clasts in tuffaceous mudstone of the so-called Lithium-rich Tuff and brecciated tuff was performed through the step-heating $^{40}\text{Ar}/^{39}\text{Ar}$ method. The main conclusions are the following:

- The obtained dates on mica crystal clasts in tuffaceous mudstone of the Lithium-rich Tuff are in the range from $8,978 \pm 73$ ka to $8,717 \pm 44$ ka, with a total difference of 261 kyr between the youngest and oldest dates. The dates on micas from three brecciated tuff samples overlap in the range of $8,823 \pm 9$ ka to $8,815 \pm 16$ ka. These dates represent formation or cooling ages of mica crystal clasts and constrain maximum depositional ages of the Lithium-rich Tuff.
- The new dates fall within the deposition interval of the Macusani Formation in the Macusani Volcanic Field between ca. 10 and 6.5 Ma. However, the dates coincide with a magmatic gap between the two eruptive episodes recorded in this formation at 10 ± 1 Ma and 7 ± 1 Ma.
- There are no reports of volcanic, volcanoclastic, or intrusive units of equivalent age in the Macusani Volcanic Field and in general, in the Macusani Structural Zone and neighboring morphostructural domains.
- The new dates demonstrate that the event related to the formation or cooling of mica crystal clasts in tuffaceous mudstone of the Lithium-rich Tuff occurred during a generalized magmatic lull in the Eastern Cordillera of the Central Andes in southeastern Peru.

7. REFERENCES

- Allmendinger RW, Jordan TE, Kay SM, Isacks BU (1997) The evolution of the Altiplano-Puna plateau of the Central Andes. *Annu Rev Earth Planet Sci* 25:139-174. <https://doi.org/10.1146/annurev.earth.25.1.139>
- American Lithium Corp. (2022a) American Lithium Significantly Extends Falchani Lithium Mineralization with Ongoing Drilling – Latest Results up to 5,025 ppm Lithium and 8,290 ppm Cesium. <https://americanlithiumcorp.com/american-lithium-significantly-extends-falchani-lithium-mineralization-with-ongoing-drilling-latest-results-up-to-5025-ppm-lithium-and-8290-ppm-cesium>. Accessed 15 December 2023
- American Lithium Corp. (2022b) American Lithium Announces 476% Increase in Measured + Indicated Lithium Resources at Falchani – Adds K, Cs and Rb to Block Model. <https://americanlithiumcorp.com/american-lithium-announces-476-increase-in-measured-indicated-lithium-resources-at-falchani-adds-k-cs-and-rb-to-block-model>. Accessed 15 December 2022
- Ausenco (2019) Bear Creek Mining Corani Project – NI 43-101 Technical Report. Available in https://minedocs.com/20/CoraniProject_Technical_Report_12172019.pdf (accessed August 10 2024)
- Baby P, Rochat P, Mascle G, Hérail G (1997) Neogene shortening contribution to crustal thickening in the back arc of the Central Andes. *Geology* 25:883–886. [https://doi.org/10.1130/0091-7613\(1997\)025<0883:NSCTCT>2.3.CO;2](https://doi.org/10.1130/0091-7613(1997)025<0883:NSCTCT>2.3.CO;2)
- Barnes VE, Edwards G, McLaughlin WA, Friedman I, Joensuu O (1970) Macusanite occurrence, age, and composition, Macusani, Peru. *Geol Soc Am Bull* 81:1539–1546. [https://doi.org/https://doi.org/10.1130/0016-7606\(1970\)81\[1539:MOAACM\]2.0.CO;2](https://doi.org/https://doi.org/10.1130/0016-7606(1970)81[1539:MOAACM]2.0.CO;2)
- Bear Creek Mining Corporation (2024) Corani. <https://bearcreekmining.com/projects/corani/> (accessed August 10, 2024)
- Benavides-Cáceres V (1999) Orogenic evolution of the Peruvian Andes: The Andean cycle. In: Skinner BJ (ed) *Geology and mineral deposits of the central Andes*. Society of Economic Geologists Special Publication 7:61–107
- Bibienne T, Magnan J-F, Rupp A, Laroche N (2020) From mine to mind and mobiles: Society’s increasing dependence on lithium. *Elements* 16:265–270. <https://doi.org/10.2138/GSELEMENTS.16.4.265>
- Boekhout F, Spikings R, Sempere T, Chiaradia M, Ulianov A, Schaltegger U (2012) Mesozoic arc magmatism along the southern Peruvian margin during Gondwana breakup and dispersal. *Lithos* 146-147:48–64. <https://doi.org/10.1016/j.lithos.2012.04.015>
- Boekhout F, Sempere T, Spikings R, Schaltegger U (2013) Late Paleozoic to Jurassic characteristic of coastal southern Peru: Temporal evolution of sedimentation along an

Boekhout F, Reitsma MJ, Spikings R, Rodriguez R, Ulianov A, Gerdes A, Schaltegger U (2018)

New age constraints on the paleoenvironmental evolution of the late Paleozoic back-arc basing along the western Gondwana margin of southern Peru. *J South Am Earth Sci* 82:165–180. <https://doi.org/10.1016/j.jsames.2017.12.016>

Bonhomme MG, Fornari M, Laubacher G, Sebrier M, Vivier G (1985a) Nuevas edades K-Ar cenozoicas de rocas volcánicas de la Cordillera de los Andes, sur este del Perú. *Universidad de Chile Comunicaciones* 35:33

Bonhomme MG, Audebaud E, Vivier G (1985b) Edades K-Ar de rocas hercínicas y neógenas de un perfil E-W en el Perú meridional. *Universidad de Chile Comunicaciones* 35:27-30

Bonhomme MG, Fornari M, Laubacher G, Sebrier M, Vivier G (1988) New Cenozoic K-Ar ages on volcanic rocks from the eastern high Andes, southern Peru. *J South Am Earth Sci* 1:179–183. [https://doi.org/10.1016/0895-9811\(88\)90035-1](https://doi.org/10.1016/0895-9811(88)90035-1)

Brooks C, Hart SR, Wendt I (1972) Realistic use of two-error regression treatments as applied to rubidium-strontium data. *Rev Geophys Space Phys* 10:551-577. <https://doi.org/10.1029/RG010i002p00551>

Callot P (2008) La Formation Ayabacas (limite Turonien-Coniacien, Sud-Pérou): collapse sous-marin en réponse à l'amorce de l'orogénèse andine. Thèse Docteur, Université Paul Sabatier - Toulouse III, Toulouse, 251 p

Carlotto V (2013) Paleogeographic and tectonic controls on the evolution of Cenozoic basins in the Altiplano and Western Cordillera of southern Peru. *Tectonophysics* 589:195–219. <http://doi.org/10.1016/j.tecto.2013.01.002>

Carrillo E, Barragán R, Hurtado C, Calderon Y, Martín G, Vázquez-Taset Y, Parra M, Rivera A, Cadena FM, Sarmiento L (2021) Depositional sequences in northern Peru: New insights on the palaeogeographic and palaeotectonic reconstruction of western Gondwana during late Permian and Triassic. *J Geol Soc* 178:1–19

Cheilletz A, Clark AH, Farrar E, Arroyo G, Duncan J, Pichavant M (1990) Stratigraphy and geochronology of the Macusani ignimbrite field: Chronometer of the Mio-Pliocene geodynamic evolution of the Andes of SE Peru. In: Symposium international “Géodynamique andine”: résumés des communications. ORSTOM, Paris, pp 341–344

Cheilletz A, Clark AH, Farrar E, Pauca GA (1992) Volcano-stratigraphy and $^{40}\text{Ar}/^{39}\text{Ar}$ geochronology of the Macusani ignimbrite field: Monitor of the Miocene geodynamic evolution of the Andes of southeast Peru. *Tectonophysics* 205:307–327. [https://doi.org/10.1016/0040-1951\(92\)90433-7](https://doi.org/10.1016/0040-1951(92)90433-7)

Clark AH, Palma VV, Archibald DA, Farrar E, Arenas MJ, Robertson RC (1983) Occurrence and age of tin mineralization in the Oriental Cordillera, Southern Peru. *Econ Geol* 78:514–520

- constraints on the metallogenic evolution of the Andes of southeastern Peru. *Econ Geol* 85:1520–1583. <https://doi.org/10.2113/gsecongeo.85.7.1520>
- Clark AH, Chen Y, Grant JW, Kontak DJ, Wasteneys HA, Sandeman HA, Farrar E, Archibald DE (2000) Delayed inception of ore deposition in major lithophile-metal vein systems: The San Rafael tin and Pasto Bueno tungsten deposits, Peru. *Geological Society of America Abstracts with Programs*, v. 32, no. 7, Reno, Nevada, p. A-279
- Colman SM, Bradbury JP, McGeehin JP, Holmes CW, Edginton D, Sarna-Wojcicki AM (2004) Chronology of sediment deposition in Upper Klamath Lake, Oregon. *J Paleolimnol* 31:139–149. <https://doi.org/10.1023/B:JOPL.0000019234.05899.ea>
- Cóndor J (2019) Lito: Descubren nuevas reservas en yacimiento en Puno. *Gestión*. <https://gestion.pe/economia/empresas/peru-plateau-energy-anuncia-descubrimiento-nueva-area-rica-litio-269047-noticia>. Accessed 22 June 2022
- Correo (2018) Descubren la que podría ser la mina de litio más grande del mundo en Puno. *Correo*. <https://diariocorreo.pe/edicion/puno/puno-25-millones-de-toneladas-de-litio-fueron-descubiertas-en-mina-830474>. Accessed 22 June 2022
- Dalmayrac B, Laubacher G, Marocco R (1977) Géologie des Andes péruviennes: caractères généraux de l'évolution géologique des andes péruviennes. Dissertation, Université des Sciences et Techniques du Languedoc
- De la Cruz J, López J, León W, Lara M (1996) Geología del cuadrángulo de Macusani. Hoja 29-v. Instituto Geológico, Minero y Metalúrgico, 197p
- European Commission (2020) Study on the EU's list of Critical Raw Materials. European Commission, Brussels, Belgium, 158 p
- Evernden JF, Kistler RW (1970) Chronology of emplacement of Mesozoic batholithic complexes in California and Western Nevada. *USGS Professional Paper* 623
- Farrar E, Yamamura BK, Clark AH, Taibe AJ (1990) $^{40}\text{Ar}/^{39}\text{Ar}$ ages of magmatism and tungsten-polymetallic mineralization, Palca 11, Choquene District, southeastern Peru. *Econ Geol* 85:1669–1676. <https://doi.org/10.2113/gsecongeo.85.7.1669>
- Fleischer RL, Price PB (1964) Fission track evidence for the simultaneous origin of tektites and other natural glasses. *Geochim Cosmoch Acta* 28:755-760. [https://doi.org/10.1016/0016-7037\(64\)90029-8](https://doi.org/10.1016/0016-7037(64)90029-8)
- Francis GH (1959) Ignimbritas (Sillar) de la Cordillera Oriental del sur del Peru. Instituto Nacional de Investigación y Fomento Minero, pp13-32
- French BM, Meyer HOA (1970) Andalusite and " β -quartz" in Macusani glass, Peru. *Carnegie Inst. Wash. Year Book* 68:339-342

- Gillis R, Horton B, Grove M (2006) Thermochronology, geochronology, and upper crustal structure of the Cordillera Real: Implications for Cenozoic exhumation of the central Andean plateau. *Tectonics* 25:TC6007. <https://doi.org/10.1029/2005TC001887>
- Harlaux M, Kouzmanov K, Gialli S, Clark AH, Laurent O, Corthay G, Flores EP, Dini A, Chauvet A, Ulianov A, Chiaradia M, Menzies A, Durand GV, Kalinaj M, Fontboté L (2021) The upper Oligocene San Rafael intrusive complex (Oriental Cordillera, southeast Peru), host of the largest-known high-grade tin deposit. *Lithos* 400–401:106409. <https://doi.org/10.1016/j.lithos.2021.106409>
- Harlaux M, Kontak DJ, Clark AH, Kouzmanov K, Holm-Denoma CS, Gialli S, Laurent O, Spikings R, Chauvet A, Dini A, Kalinaj M, Fontboté L (2023) Depositing >1.5 Mt of tin within <1 m.y. of initial granitic intrusion in the San Rafael tin (-copper) Deposit, southeastern Peru. *Econ Geol* 118:1371–1396. <https://doi.org/10.5382/econgeo.5021>
- IIMP (2024) A fines de 2024 empezarán obras del proyecto Corani. <https://www.iimp.org.pe/mineria-en-el-peru/a-fines-del-2024-empezarian-obras-del-proyecto-corani> (accessed August 10 2024)
- INGEMMET (2023) Carta Geológica Nacional – Escala 1:50,000. Ministerio de Energía y Minas. <https://portal.ingemmet.gob.pe/web/guest/mapa-geologico-50-000>
- Jäger E (1979) Introduction to Geochronology. In: Jäger E, Hunziker JC (eds) *Lectures in Isotope Geology*. Springer Berlin, Heidelberg. https://doi.org/10.1007/978-3-642-67161-6_1
- Jiménez M, López-Velásquez S (2008) Magmatism in the Huarina belt, Bolivia, and its geotectonic implications. *Tectonophysics* 459:85–106. <https://doi.org/10.1016/j.tecto.2007.10.012>
- Kay S, Mpodozis C (2021) The Andes. In: Alderton D, Elias SA (eds) *Encyclopedia of Geology*, 2nd edn. Academic Press, Cambridge, pp 1-15. <https://doi.org/10.1016/B978-0-08-102908-4.00173-9>
- Kontak DJ (1984) The magmatic and metallogenetic evolution of a craton-orogen interface: the Cordillera de Carabaya, central Andes, SE Peru. Dissertation, Queen's University
- Kontak DJ, Clark AH (2002) Genesis of the giant, bonanza San Rafael lode tin deposit, Peru: Origin and significance of pervasive alteration. *Econ Geol* 97, 1741-1777. <https://doi.org/10.2113/gsecongeo.97.8.1741>
- Kontak DJ, Clark AH, Farrar E (1984a) The magmatic evolution of the Oriental Cordillera, southeastern Peru. In: Harmon RS, Barreiro BA (eds) *Andean Magmatism*. Birkhäuser Boston, Boston, pp 203–219. https://doi.org/10.1007/978-1-4684-7335-3_15
- Kontak DJ, Pichavant M, Clark AH (1984b) Petrology of the Pliocene peraluminous volcanics

- Cobbing J, Beckinsale RD (eds) *Magmatism at a plate edge: The Peruvian Andes*. Wiley, New York, pp 36–44
- Kontak DJ, Clark AH, Farrar E, Pearce TH, Strong DF, Baadsgaard H (1986) Petrogenesis of a Neogene shoshonite suite, Cerro Moromoroni, Puno, southeastern Peru. *Can Mineral* 24:117–135
- Kontak DJ, Clark AH, Farrar E, Archibald DA (1987) Geochronological data for Tertiary granites of the Southeast Peru segment of the Central Andean tin belt. *Econ Geol* 82:1611–1618. <https://doi.org/10.2113/gsecongeo.82.6.1611>
- Kontak DJ, Clark AH, Farrar E, Archibald DA, Baadsgaard H (1990a) Late Paleozoic-early Mesozoic magmatism in the Cordillera de Carabaya, Puno, southeastern Peru: Geochronology and petrochemistry. *J South Am Earth Sci* 3:213–230. [https://doi.org/10.1016/0895-9811\(90\)90004-K](https://doi.org/10.1016/0895-9811(90)90004-K)
- Kontak DJ, Farrar E, Clark AH, Archibald DA (1990b) Eocene tectono-thermal rejuvenation of an upper Paleozoic-lower Mesozoic terrane in the Cordillera de Carabaya, Puno, southeastern Peru, revealed by K-Ar and $^{40}\text{Ar}/^{39}\text{Ar}$ dating. *J South Am Earth Sci* 3:231–246. [https://doi.org/10.1016/0895-9811\(90\)90005-L](https://doi.org/10.1016/0895-9811(90)90005-L)
- Koppers AA (2002) ArArCALC-software for $^{40}\text{Ar}/^{39}\text{Ar}$ age calculations. *Comput Geosci* 28:605–619. [https://doi.org/10.1016/s0098-3004\(01\)00095-4](https://doi.org/10.1016/s0098-3004(01)00095-4)
- Kuiper KF, Deino A, Hilgen FJ, Krijgsman W, Renne PR, Wijbrans JR (2008) Synchronizing rock clocks. *Science* 320:500–504. <https://doi.org/10.1126/science.1154339>
- Lancelot JR, Laubacher G, Marocco R, Renaud U (1978) U/Pb radiochronology of two granitic plutons from the eastern Cordillera (Peru) - Extent of Permian magmatic activity and consequences. *Geol Rundschau* 67:236–243. <https://doi.org/10.1007/BF01803263>
- Laubacher G (1978) *Estudio geológico de la región Norte del lago Titicaca*. Instituto Geológico, Minero y Metalúrgico, 120 p
- Laubacher G, Sebrier M, Fornari M, Carlier G (1988) Oligocene and Miocene continental sedimentation, tectonics, and S-type magmatism in the southeastern Andes of Peru (Crucero Basin): Geodynamic implications. *J South Am Earth Sci* 1:225–238. [https://doi.org/10.1016/0895-9811\(88\)90001-6](https://doi.org/10.1016/0895-9811(88)90001-6)
- Lee JKW (2015) Ar–Ar and K–Ar Dating. In Jack Rink W, Thompson JW (ed) *Encyclopedia of Scientific Dating Methods*. Encyclopedia of Earth Sciences Series. Springer, Dordrecht, pp 58-73. https://doi.org/10.1007/978-94-007-6304-3_40
- Lee JY, Marti K, Severinghaus JP, Kawamura K, Yoo HS, Book J, Seog J (2006) A redetermination of the isotopic abundances of atmospheric Ar. *Geochim Cosmochim Acta*

- London D (2015) Reading pegmatites: What beryl says. *Rocks Miner* 90:138-149. <https://doi.org/10.1080/00357529.2014.949173>
- London D, Hervig RL, Morgan GB (1988) Melt-vapor solubilities and elemental partitioning in peraluminous granite-pegmatite systems: Experimental results with Macusani glass at 200 MPa. *Contrib Mineral Petrol* 99:360–373. <https://doi.org/10.1007/BF00375368>
- López-Gamundí OR, Rossello EA (1993) Devonian-Carboniferous unconformity in Argentina and its relation to the Eo-Hercynian orogeny in southern South America. *Geol Rundschau* 82:136–147. <https://doi.org/10.1007/BF00563276>
- López JC (1996) Geología del cuadrángulo de Nuñoa. Hoja 29-u. Instituto Geológico, Minero y Metalúrgico, 171p
- McBride SL, Robertson RCR, Clark AH, Farrar E (1983) Magmatic and metallogenetic episodes in the northern tin belt, cordillera real, Bolivia. *Geol Rundschau* 72:685–713. <https://doi.org/10.1007/BF01822089>
- McQuarrie N, Decelles P (2001) Geometry and structural evolution of the central Andean backthrust belt, Bolivia. *Tectonics* 20:669–692. <https://doi.org/10.1029/2000TC001232>
- Min K, Mundil R, Renne PR, Ludwig KR (2000) A test for systematic errors in $^{40}\text{Ar}/^{39}\text{Ar}$ geochronology through comparison with U/Pb analysis of a 1.1-Ga rhyolite. *Geochim Cosmochim Acta* 64:73–98
- Mišković A, Spikings RA, Chew DM, Košler J, Ulianov A (2009) Tectonomagmatic evolution of Western Amazonia: Geochemical characterization and zircon U-Pb geochronologic constraints from the Peruvian Oriental Cordilleran granitoids. *Geol Soc Am Bull* 121:1298–1324. <https://doi.org/10.1130/B26488.1>
- Mlynarczyk MSJ, Williams-Jones AE (2005) The role of collisional tectonics in the metallogeny of the Central Andean tin belt. *Earth Planet Sci Lett* 240:656-667. <https://doi.org/10.1016/j.epsl.2005.09.047>
- Mukasa SB (1986) Zircon U-Pb ages of super-units in the Coastal batholith, Peru: Implications for magmatic and tectonic processes. *Geol Soc Am Bull* 97:241–254. [https://doi.org/10.1130/0016-7606\(1986\)97<241:ZUAOSI>2.0.CO;2](https://doi.org/10.1130/0016-7606(1986)97<241:ZUAOSI>2.0.CO;2)
- Newell ND (1949) Geology of the Lake Titicaca region, Peru and Bolivia. In: *Geological Society of America Memoirs*, Geological Society of America, Baltimore, 111 p
- Newell ND, Chronic J, Roberts TG (1953) Upper Paleozoic of Peru. In: *Geological Society of America Memoirs*, Geological Society of America, Baltimore, 276 p
- Noble DC, Vogel TA, Peterson PS, Landis GP, Grant NK, Jezek PA, McKee EH (1984) Rare-element-enriched, S-type ash-flow tuffs containing phenocrysts of muscovite, andalusite, and

- Perez ND, Horton BK, McQuarrie N, Stübner K, Ehlers TA (2016) Andean shortening, inversion and exhumation associated with thin- and thick-skinned deformation in southern Peru. *Geol Mag* 153:1013–1041. <https://doi.org/10.1017/S0016756816000121>
- Pitcher WS (1985) A multiple and composite batholith. In: Pitcher WS, Atherton MP, Cobbing EJ, Beckinsale RD (eds) *Magmatism at a Plate Edge: The Peruvian Andes*. Blackie, London and Glasgow, pp.93-101
- Pichavant M, Valencia Herrera J, Boulmier S, Briquieu L, Joron JL, Juteau M, Marin L, Michard A, Sheppard AMF, Treuil M, Vernet M (1987) The Macusani glasses, SE Peru: Evidence of chemical fractionation in peraluminous magmas. In: Mysen BO (ed) *Magmatic processes, physicochemical principles*. *Geochem Soc Special Publ* 1:359-373
- Pichavant M, Kontak DJ, Herrera JV, Clark AH (1988) The Miocene-Pliocene Macusani Volcanics, I. Mineralogy and magmatic evolution of a two-mica aluminosilicate-bearing ignimbrite suite SE Peru. *Contrib Mineral Petrol* 100:300–324
- Pichavant M, Villaros A, Michaud J, Scaillet B (2024a) Granite magmatism and mantle filiation. *Eur J Mineral* 36:225–246. <https://doi.org/10.5194/ejm-36-225-2024>
- Pichavant M, Erdmann S, Kontak DJ, Michaud J, Villaros A (2024b) Trace element partitioning in strongly peraluminous rare-metal silicic magmas – Implications for fractionation processes and for the origin of the Macusani Volcanics (SE Peru). *Geochim Cosmochim Acta* 365:229–252. <https://doi.org/10.1016/j.gca.2023.11.021>
- Poupeau G, Sabil N, Villa IM, Bigazzi G, Vatin-Perignon N, Flores P, Pereyra P, Salas G, Arroyo G (1992) Fission-track and K-Ar ages of “macusanite” obsidian glasses, (SE Peru): Geodynamic implications. *Tectonophysics* 205:295–305. [https://doi.org/10.1016/0040-1951\(92\)90432-6](https://doi.org/10.1016/0040-1951(92)90432-6)
- Poupeau G, Labrin E, Sabil N, Bigazzi G, Arroyo G, Vatin-Pérignon N (1993) Fission-track dating of 15 macusanite glass pebbles from the Macusani volcanic field (SE Peru). *Nucl Tracks Radiat Meas* 21:499–506. [https://doi.org/10.1016/1359-0189\(93\)90189-G](https://doi.org/10.1016/1359-0189(93)90189-G)
- Ramos VA (2018) Tectonic evolution of the Central Andes: From terrane accretion to crustal delamination. *AAPG Mem* 117:1–34. <https://doi.org/10.1306/13622115M1172855>
- Redacción Gestión (2023) Costos de American Lithium para proyecto Falchani aumentan a US\$ 700 millones. *Gestión*. <https://gestion.pe/economia/empresas/proyecto-de-litio-peru-mineria-costos-de-american-lithium-para-proyecto-falchani-aumentan-a-us-700-millones-noticia>. Accessed 12 October 2023
- Reiners PW, Carlson RW, Renne PR, Cooper KM, Granger DE, McLean NM, Schoene B (2017) The K-Ar and $^{40}\text{Ar}/^{39}\text{Ar}$ systems. In: *Geochronology and Thermochronology*, 1st edn. American Geophysical Union, John Wiley & Sons, pp. 221–257

- Robbins JA, Edgington DN (1975) Determination of recent sedimentation rates in Lake Michigan using Pb-210 and Cs-137. *Geochim Cosmochim Acta* 39:285–304. [https://doi.org/10.1016/0016-7037\(75\)90198-2](https://doi.org/10.1016/0016-7037(75)90198-2)
- Rochat P, Hérial G, Baby P, Mascle G, Aranibar O (1998) Geometric analysis and tectonosedimentary model of the northern Bolivian Altiplano. *Earth Planet Sci Lett, Series IIA* 327:769-775
- Rodriguez R, Choquehuanca S, Sánchez E, Fabián C, del Castillo B (2021). Geología de los cuadrángulos de Macusani (hojas 29v1, 29v2, 29v3, 29v4) y Limbani (hojas 29x1, 29x2, 29x3, 29x4). Instituto Geológico, Minero y Metalúrgico, 82 p
- Rollinson HR (1993) *Using Geochemical Data: Evaluation, Presentation, Interpretation*, 1st edn. Longman Scientific & Technical, England
- Rutherford E, Soddy F (1903) LX. Radioactive Change. *The London, Edinburgh, and Dublin Philosophical Magazine and Journal of Science* 5:576-591. <http://doi.org/10.1080/14786440309462960>
- Saldarriaga J (2021) Proyecto de litio en Puno cambia de manos y pertenece ahora a American Lithium. *El Comercio*. <https://elcomercio.pe/economia/dia-1/litio-proyecto-de-litio-en-puno-cambia-de-manos-y-pertenece-ahora-a-american-lithium-uranio-noticia/>. Accessed 25 November 2022
- Sánchez AW, Zapata AA (2003) Memoria descriptiva de la revisión y actualización de los cuadrángulos de Río Picha (25-p), Timpia (25-q), Chuanquiri (26-p), Quillabamba (26-q), Quebrada Honda (26-r), Parobamba (26-s), Pacaypata (27-p), Machupicchu (27-q), Urubamba (27-r), Calca (27-s), Chotachaca (27-t), Quincemil (27-u), Ocongate (28-t), Corani (28-u) y Ayapata (28-v). Instituto Geológico, Minero y Metalúrgico, 51 p.
- Sandeman HA, Clark AH (1993) Mingling and mixing of minette and S-type, anatectic, rhyodacitic magmas. Crucero Supergroup, Puno, SE Peru. *Geological Association of Canada-Mineralogical Association of Canada, Program with Abstracts* 18:A-92
- Sandeman HA, Clark AH, Farrar E (1995) An integrated tectono-magmatic model for the evolution of the southern Peruvian Andes (13–20°S) since 55 Ma. *Int Geol Rev* 37:1039–1073. <https://doi.org/10.1080/00206819509465439>
- Sandeman HA, Clark AH, Farrar E, Arroyo-Pauca G (1996) A critical appraisal of the Cayconi Formation, Crucero Basin, southeastern Peru. *J South Am Earth Sci* 9:381–392. [https://doi.org/10.1016/s0895-9811\(96\)00021-1](https://doi.org/10.1016/s0895-9811(96)00021-1)
- Sandeman HA, Clark AH, Farrar E, Arroyo GA (1997) Lithostratigraphy, petrology and $^{40}\text{Ar}/^{39}\text{Ar}$ geochronology of the Crucero Supergroup, Puno department, SE Peru. *J South Am Earth Sci* 10:223–245. [https://doi.org/10.1016/s0895-9811\(97\)00023-0](https://doi.org/10.1016/s0895-9811(97)00023-0)

- Sempere T, Hérail G, Oller J, Bonhomme MG (1990) Late Oligocene-early Miocene major tectonic crisis and related basins in Bolivia. *Geology* 18:946. [https://doi.org/10.1130/0091-7613\(1990\)018<0946:LOEMMT>2.3.CO;2](https://doi.org/10.1130/0091-7613(1990)018<0946:LOEMMT>2.3.CO;2)
- Sempere T (1995) Phanerozoic evolution of Bolivia and adjacent regions. In: American Association of Petroleum Geologists (eds) *Petroleum Basins of South America*. American Association of Petroleum Geologists, Tulsa, pp 207-230
- Sempere T, Carlier G, Soler P, Fornari M, Carlotto V, Jacay J, Arispe O, Néraudeau D, Cárdenas J, Rosas S, Jiménez N (2002) Late Permian-Middle Jurassic lithospheric thinning in Peru and Bolivia, and its bearing on Andean-age tectonics. *Tectonophysics* 345:153–181. [https://doi.org/10.1016/S0040-1951\(01\)00211-6](https://doi.org/10.1016/S0040-1951(01)00211-6)
- Sempere T, Acosta H, Carlotto V (2004) Estratigrafía del Mesozoico y Paleógeno al norte del Lago Titicaca. *Sociedad Geológica del Perú, Publicación Especial* 5:81-103
- SIDEMCAT (2024) Consulta al Sistema de Derechos Mineros y Catastro. In: INGEMMET. <https://digital.ingemmet.gob.pe/serviciosdigitales/app/sidemcat/consulta>. Accessed 5 Ene 2024
- Soberon D, Rodriguez R, Choquehuanca S, Gómez W (2002) Geología del cuadrángulo de Corani. Hoja 29u1, 28u2, 28u3, 28u4. Instituto Geológico, Minero y Metalúrgico, 111 p
- Spikings R, Reitsma MJ, Boekhout F, Mišković A, Ulianov A, Chiaradia M, Gerdes A, Schaltegger U (2016) Characterization of Triassic rifting in Peru and implications for the early disassembly of western Pangaea. *Gondwana Res* 35:124–143. <https://doi.org/10.1016/j.gr.2016.02.008>
- Stein HJ (2014) Dating and tracing the history of ore formation. In: Holland HD, Turekian KK (eds) *Treatise on Geochemistry*, 2nd edn, 13:87-118, Elsevier, Oxford
- Stewart JW, Evernden JF, Snelling NJ (1974) Age determinations from Andean Peru: A reconnaissance survey. *Geol Soc Am Bull* 85:1107–1116. [https://doi.org/10.1130/0016-7606\(1974\)85<1107:ADFAPA>2.0.CO;2](https://doi.org/10.1130/0016-7606(1974)85<1107:ADFAPA>2.0.CO;2)
- Swarthout A, Leduc M, Rios C (2010) The Discovery History and Geology of Corani: A Significant New Ag-Pb-Zn Epithermal Deposit, Puno Department, Peru". In: Goldfarb RJ, Marsh EE, Monecke T, *The Challenge of Finding New Mineral Resources: Global Metallogeny, Innovative Exploration, and New Discoveries*. Special Publication of the Society of Economic Geologists, 15. <https://doi.org/10.5382/SP.15.1.10>
- The Mineral Corporation (2019) Mineral Resource Estimates for the Falchani Lithium Project in the Puno District of Peru. Bryanston, pp 1-72.
- Ullrich TD (2006) Report on $^{40}\text{Ar}/^{39}\text{Ar}$ geochronological analysis: Unpublished report to Bear

Vilca Arpasi PC (2020) El proyecto de explotación de litio en Puno. Asociación Servicios Educativos Rurales, Lima. Available online: https://sinia.minam.gob.pe/sites/default/files/siar-puno/archivos/public/docs/informe_litio_en_puno_online.pdf

White WM (2015) Isotope Geochemistry. Wiley-Blackwell, New York

Wörner G, Schildgen TF, Reich M (2018) The Central Andes: Elements of an extreme land. *Elements* 14:225–230. <https://doi.org/10.2138/gselements.14.4.225>





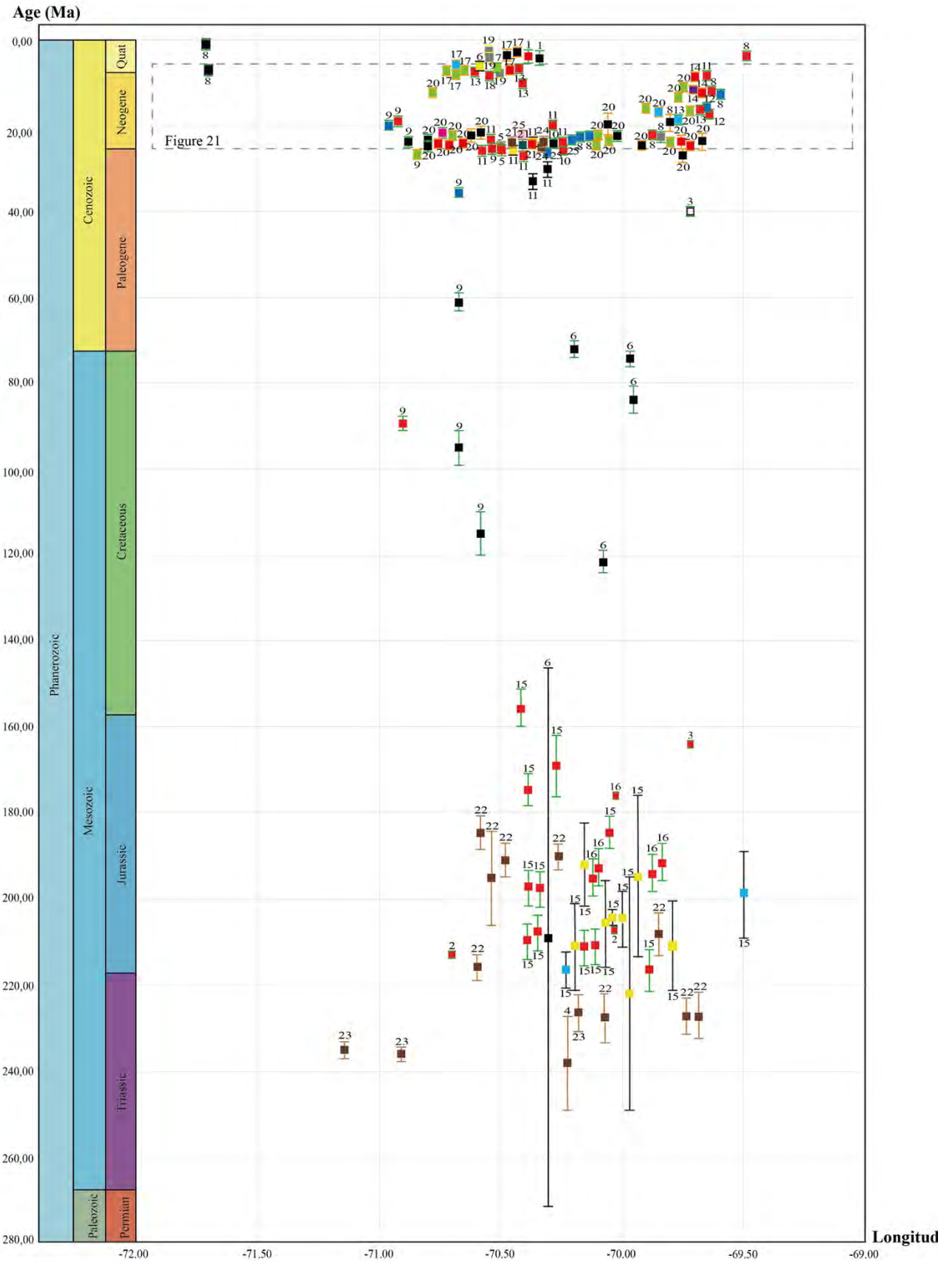
APPENDICES

APPENDIX A: Compilation of previous radiometric dates on rocks from the Macusani Structural Zone and surrounding morphostructural zones available from the following link:

<https://docs.google.com/spreadsheets/d/1pglRuHtx184rDfBk-hIEa4z6mIC8nYPf/edit#gid=1401339546>



APPENDIX B: General geochronological chart showing previous radiometric dates on rocks from the Macusani Structural Zone and surrounding morphostructural zones.



DATING TECHNIQUE		MATERIAL ANALYZED	
K-Ar	Rb-Sr	Biotite	K-Feldspar
U-Pb	Ar-Ar	Biotite - Whole rock	Sanidine
Fission Track		Glass	Unspecified
		Monazite	Whole rock
		Cassiterite	Muscovite
		Feldspar	Zircon
		Plagioclase	

REFERENCES		
1 Barnes et al. (1970)	10 Kontak et al. (1986)	18 Poupeau et al. (1992)
2 Evernden et al. (1970)	11 Kontak et al. (1987)	19 Poupeau et al. (1993)
3 Stewart et al. (1974)	12 Laubacher et al. (1988)	20 Sandeman et al. (1997)
4 Lancelot et al. (1978)	13 Pichavant et al. (1988)	21 Clark et al. (2000)
5 Clark et al. (1983)	14 Farrar et al. (1990)	22 Mišković et al. (2009)
6 Kontak (1984)	15 Kontak et al. (1990a)	23 Spikings et al. (2016)
7 Noble et al. (1984)	16 Kontak et al. (1990b)	24 Harlaux et al. (2021)
8 Bonhomme et al. (1985a)	17 Cheilletz et al. (1992)	25 Harlaux et al. (2023)
9 Bonhomme et al. (1985b)		

APPENDIX C. Code of the analyzed samples and their location (geographic coordinates), concession of provenance, and macroscopic description.

Sample	Latitude (S)	Longitude (W)	Elevation (m.a.s.l.)	Drill core*	Concession	Description
2021-MAC-005	14° 00' 10.5"	70° 41' 14.2"	4,950	-	Falchani	Oligomictic cemented floatbreccia with darker matrix and lighter sub-rounded to angular clasts with sizes in the range from 1 to 10 mm. Bluish-black and gray patches are overprinted over the aforementioned rock components. Surface-impregnate ferric oxides and hydroxides exhibit a highlighting brownish-orange color.
2021-MAC-006	14° 00' 11.9"	70° 41' 14.5"	4,972	-	Falchani	Oligomictic cemented floatbreccia with irregular lamination defined by contorted and discontinuous alternate brighter and darker mm-scale laminae. Both the matrix and clasts are composed of a mud-sized hard material that host sporadic, unevenly distributed, medium ash-sized biotite crystal clasts. The matrix is slightly darker than the clasts. Some clasts present a beige rim. Surface-impregnate ferric oxides and hydroxides exhibit brownish-orange colors.
2021-MAC-08A	14° 00' 1.1"	70° 41' 10.4"	4,899	-	Falchani	Finely laminated tuffaceous mudstone with relatively abundant and coarse cavities after concretion dissolution. Alternating gray/light laminae are irregularly stacked and include wavy and convoluted

Sample	Latitude (S)	Longitude (W)	Elevation (m.a.s.l.)	Drill core*	Concession	Description
						<p>levels. Medium ash-sized biotite crystal clasts are unevenly distributed and bedded within the laminae. Cavities exhibit two morphology types: moderate-sphericity (1-2 length/thickness ratios, with 1-16 mm length parallel to the laminated microstructure); and flattened- to planar-voids with irregular shape. Concretions relicts consist of fine concentric bands. The surfaces of cavity walls and concretion relicts are covered with very fine aggregates of euhedral, tabular, brownish-orange crystals and very fine to fine (up to 0.5 mm), acicular, radiating translucent, colorless crystal aggregates druses.</p>
2021-MAC-11B	14° 00' 8.3"	70° 40' 18.3"	4,716	-	Falchani	<p>Finely laminated, tuffaceous mudstone with abundant irregular cavities. Alternating orange-beige/white laminae are irregularly stacked and make up planar and slightly wavy levels that host unevenly distributed, matrix-supported, very fine to medium-grained biotite crystal fragments. Cavities exhibit two main morphology-types: high- to moderate-sphericity (1-7 mm long parallel to the laminated microstructure); and irregular, flattened ovoid. Adjacent spherical cavities may join together within a given sedimentary level. There is an extremely convoluted level (4.5 cm in thickness) that hosts closed packaged ovoid cavities with high sphericity up to 5 mm in size. Cavity walls are generally coated by very fine-grained druses.</p>

Sample	Latitude (S)	Longitude (W)	Elevation (m.a.s.l.)	Drill core*	Concession	Description
2021-MAC-025	14° 00' 12.4"	70° 40' 53.3"	4,884	-	Falchani	Massive, white to slightly gray, tuffaceous mudstone. Scarce matrix-supported, medium ash-size biotite crystals fragments are observed.
2021-MAC-031	14° 00' 17.8"	70° 41' 6.4"	4,943	-	Falchani	Oligomictic cemented floatbreccia with darker matrix and brighter sub-rounded to angular with sizes comprised between 1 and 10 mm. Matrix and clasts are composed of a mud-sized hard material, and both host sporadic, unevenly distributed, medium ash-sized biotite crystal fragments. Clasts exhibit internal fine (mm-scale) bedding.
2021-MAC-038	14° 00' 8.6"	70° 40' 8.9"	4,684	PCHAC 01-TSW(1)	Falchani	Cohesive, finely laminated, foliated, tuffaceous mudstone. Alternating white/gray laminae are regularly stacked, and make up planar to gently wavy levels that host unevenly distributed fine ash- to medium ash-grained (up to 1.5 mm) biotite crystals fragments.
2021-MAC-048	13° 59' 59.9"	70° 40' 8.2"	4,576	PCHAC 04-TV	Falchani	Cohesive, finely laminated, tuffaceous mudstone. Alternating white, gray, and orange-beige laminae are regularly stacked and make up planar to slightly wavy levels. Fine to medium ash-sized (up to 1 mm), matrix-supported biotite crystal fragments are unevenly distributed and tend to be oriented parallel to the laminated microstructure.

Sample	Latitude (S)	Longitude (W)	Elevation (m.a.s.l.)	Drill core*	Concession	Description
2021- MAC-067	14° 07' 32"	70° 40' 24.9"	5,031	-	San Vicente White	Massive, pale pink, crystal-rich, tuffaceous mudstone. The crystal clasts are matrix-supported and include mostly smoky, euhedral, bipyramidal, coarse ash to extremely fine lapilli-sized (up to 4.5 mm) quartz and white, euhedral, prismatic K feldspar fragments. K feldspar clasts show two distinct size populations: medium lapilli (5 to 7.5 mm long), and fine lapilli (1.2 to 3.3 mm long). Biotite crystal clasts are partially or completely oxidized, and show two distinct size populations: fine ash, and medium ash (up to 1.6 mm). Molds of plagioclase crystals are up to 1 mm in length and have been pseudomorphically replaced by a very fine-grained, soft material. Scarce, subhedral, pinkish muscovite crystal clasts are fine-grained (<1 mm). Scarce, black, euhedral-prismatic tourmaline crystal-clasts are <0.1 mm in length.

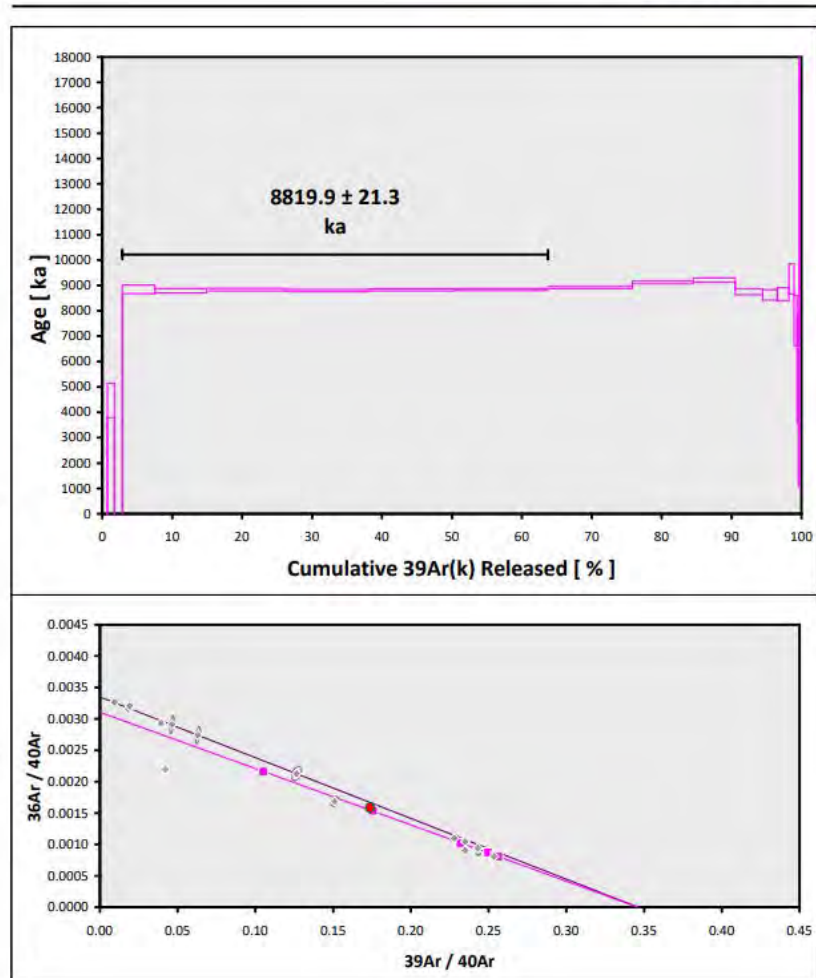
* For drill core samples, coordinates of the respective drill core collars are provided.

APPENDIX D. $^{40}\text{Ar}/^{39}\text{Ar}$ results

2021-MAC-005

Information on Analysis and Constants Used in Calculations	Results	$^{40}\text{Ar}/^{36}\text{Ar} \pm 2\sigma$	$^{40}\text{Ar}/^{39}\text{Ar}(k) \pm 2\sigma$	Age $\pm 2\sigma$ (ka)	MSWD	$^{39}\text{Ar}(k)$ (%), n	K/Ca $\pm 2\sigma$
Project = Sample = 2021-MAC-5 Material = Biotite Location = Peru Region = Peru Analyst = Kevin Konrad Irradiation = UNLV-128-1 Position = X: 0 Y: 0 Z/H: 23 mm FCT Age = 28.201 \pm 0.023 Ma FCT Reference = Kuiper et al. (2008) FCT $^{40}\text{Ar}/^{39}\text{Ar}$ Ratio = FCT J-value = 0.00169230 \pm 0.00000034 Air Shot $^{40}\text{Ar}/^{36}\text{Ar}$ = 306.8400 \pm 0.4418 Air Shot MDF = 0.99324509 \pm 0.00043265 (LIN) Experiment Type = Sample Extraction Method = Furnace Heating Heating = 840 sec Isolation = 20.00 min Instrument = NGX Preferred Age = Plateau Age Age Classification = Crystallization Age IGSN = Undefined Rock Class = Undefined Lithology = Unknown Lat-Lon = Undefined - Undefined Age Equations = Min et al. (2000) Negative Intensities = Allowed Collector Calibrations = 36Ar Decay ^{40}K (total) = 5.530 \pm 0.048 E-10 1/a Decay Activity ^{40}K (EC, β^-) = 3.310 \pm 0.040 1/g Decay Activity ^{40}K (β^-) = 28.270 \pm 0.050 1/g Decay ^{39}Ar = 2.940 \pm 0.016 E-07 1/h Decay ^{37}Ar = 8.230 \pm 0.012 E-04 1/h Decay ^{36}Cl = 2.257 \pm 0.015 E-06 1/a Production $^{39}\text{Ar}/^{37}\text{Ar}$ (ca) = 0.0006858 \pm 0.0000029 Production $^{38}\text{Ar}/^{37}\text{Ar}$ (ca) = 0.0000247 \pm 0.0000047 Production $^{36}\text{Ar}/^{37}\text{Ar}$ (ca) = 0.0002643 \pm 0.0000291 Production $^{38}\text{Ar}/^{39}\text{Ar}(k)$ = 0.012135 \pm 0.000066 Production $^{36}\text{Ar}/^{38}\text{Ar}(cl)$ = 262.80 \pm 1.71 Scaling Ratio K/Ca = 0.430 Abundance Ratio $^{40}\text{K}/\text{K}$ = 1.1700 \pm 0.0100 E-04 Atomic Weight K = 39.0983 \pm 0.0001 g Trapped $^{40}\text{Ar}/^{36}\text{Ar}$ = 321.78 \pm 1.01 Trapped $^{38}\text{Ar}/^{36}\text{Ar}$ = 0.1885 \pm 0.0003 Standard MDF $^{40}\text{Ar}/^{36}\text{Ar}$ = 298.56 \pm 0.31 Standard MDF Reference = Lee et al 2006	Age Plateau 2.88915 \pm 0.00691 \pm 0.24% Full External Error \pm 147.3 Analytical Error \pm 21.1 8819.9 \pm 21.3 \pm 0.24% Full External Error \pm 147.3 Analytical Error \pm 21.1	321.76 \pm 2.03 \pm 0.63%	2.88921 \pm 0.01055 \pm 0.37%	8820.1 \pm 32.3 \pm 0.37% Full External Error \pm 149.3 Analytical Error \pm 32.1	0.56 73% 2.26 1.0000	60.90 6 2a Confidence Limit Error Magnification	1676 \pm 545
	Total Fusion Age 2.81704 \pm 0.00918 \pm 0.33% Full External Error \pm 144.9 Analytical Error \pm 28.0 8600.3 \pm 28.2 \pm 0.33% Full External Error \pm 144.9 Analytical Error \pm 28.0					21 170 \pm 2	
	Normal Isochron 321.76 \pm 2.03 \pm 0.63%	2.88921 \pm 0.01055 \pm 0.37%	8820.1 \pm 32.3 \pm 0.37% Full External Error \pm 149.3 Analytical Error \pm 32.1	0.99 41% 2.41 1.0000	60.90 6 2a Confidence Limit Error Magnification		
	Inverse Isochron 321.78 \pm 2.03 \pm 0.63%	2.88916 \pm 0.01055 \pm 0.37%	8819.9 \pm 32.3 \pm 0.37% Full External Error \pm 149.3 Analytical Error \pm 32.1	0.99 41% 2.41 1.0000	60.90 6 2a Confidence Limit Error Magnification	44% Spreading Factor	

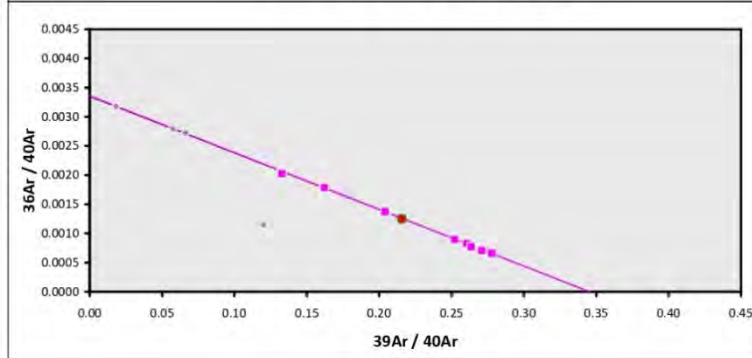
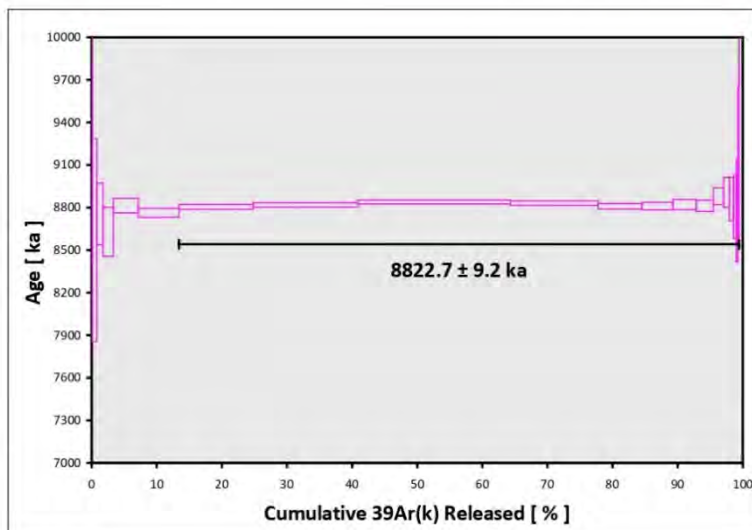
Excess $^{40}\text{Ar}/^{36}\text{Ar}$ = 321.78 \pm 0.32 (%SD).



Information on Analysis and Constants Used in Calculations

Project =
 Sample = **2021-MAC-6**
 Material = **Biotite**
 Location = **Peru**
 Region = **Peru**
 Analyst = **Kevin Konrad**
 Irradiation = **UNLV-128-1**
 Position = **X: 0 | Y: 0 | Z/H: 22 mm**
 FCT-NM Age = **28.201 ± 0.023 Ma**
 FCT-NM Reference = **Kulper et al. (2008)**
 FCT-NM 40Ar/39Ar Ratio =
 FCT-NM J-value = **0.00169010 ± 0.00000034**
 Air Shot 40Ar/36Ar = **305.9440 ± 0.4528**
 Air Shot MDF = **0.99395842 ± 0.00044187 (LIN)**
 Experiment Type = **Sample**
 Extraction Method = **Furnace Heating**
 Heating = **840 sec**
 Isolation = **20.00 min**
 Instrument = **NGX**
 Preferred Age = **Plateau Age**
 Age Classification = **Crystallization Age**
 IGSN = **Undefined**
 Rock Class = **Undefined**
 Lithology = **Undefined**
 Lat-Lon = **Undefined - Undefined**
 Age Equations = **Min et al. (2000)**
 Negative Intensities = **Allowed**
 Collector Calibrations = **36Ar**
 Decay 40K(total) = **5.530 ± 0.048 E-10 1/a**
 Decay Activity 40K(ϵ , β^+) = **3.310 ± 0.040 1/g**
 Decay Activity 40K(β^-) = **28.270 ± 0.050 1/g**
 Decay 39Ar = **2.940 ± 0.016 E-07 1/h**
 Decay 37Ar = **8.230 ± 0.012 E-04 1/h**
 Decay 36Cl = **2.257 ± 0.015 E-06 1/a**
 Production 39/37(ca) = **0.0006858 ± 0.0000029**
 Production 38/37(ca) = **0.0000247 ± 0.0000047**
 Production 36/37(ca) = **0.0002643 ± 0.0000291**
 Production 38/39(k) = **0.012135 ± 0.000066**
 Production 36/38(d) = **262.80 ± 1.71**
 Scaling Ratio K/Ca = **0.430**
 Abundance Ratio 40K/K = **1.1700 ± 0.0100 E-04**
 Atomic Weight K = **39.0983 ± 0.0001 g**
 Trapped 40/36(a) = **298.56 ± 0.31**
 Trapped 38/36(a) = **0.1885 ± 0.0003**
 Standard MDF 40/36(a) = **298.56 ± 0.31**
 Standard MDF Reference = **Lee et al 2006**

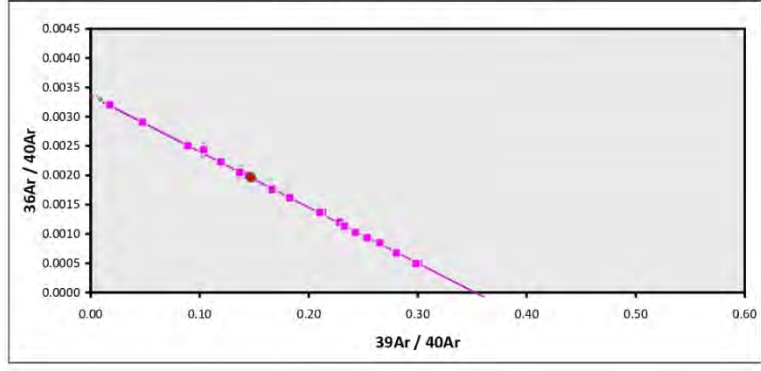
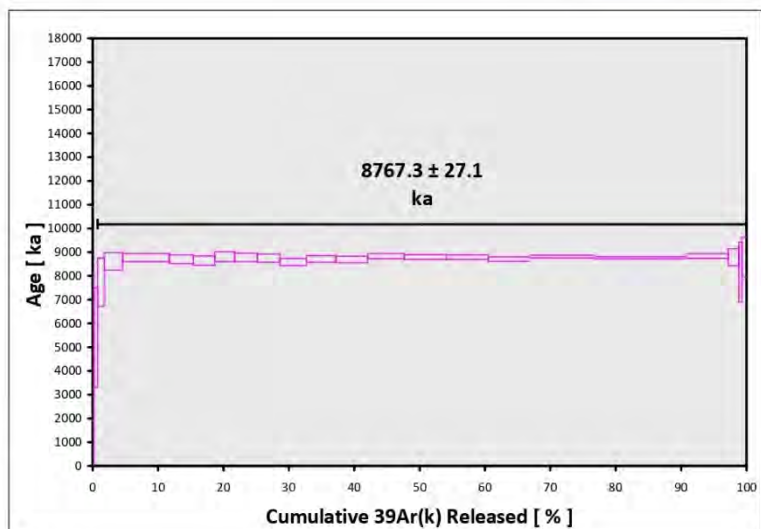
Results	40(a)/36(a) ± 2σ	40(r)/39(k) ± 2σ	Age ± 2σ (ka)	MSWD	39Ar(k) (%n)	K/Ca ± 2σ
Age Plateau		2.89384 ± 0.00281 ± 0.10%	8822.7 ± 9.2 ± 0.10% Full External Error ± 146.1 Analytical Error ± 8.5	1.64 7% 1.2795	86.02 14 2σ Confidence Limit Error Magnification	861 ± 405
Total Fusion Age		2.90691 ± 0.00301 ± 0.10%	8862.4 ± 9.8 ± 0.11% Full External Error ± 146.8 Analytical Error ± 9.1		21	337 ± 8
Normal Isochron Error Chron	297.30 ± 8.44 ± 2.84%	2.89725 ± 0.02285 ± 0.79%	8833.1 ± 69.6 ± 0.79% Full External Error ± 161.7 Analytical Error ± 69.5	1.88 3% 1.82 1.3708	86.02 14 2σ Confidence Limit Error Magnification	
Inverse Isochron Error Chron	297.34 ± 8.47 ± 2.85%	2.89718 ± 0.02293 ± 0.79%	8832.9 ± 69.8 ± 0.79% Full External Error ± 161.9 Analytical Error ± 69.8	1.90 3% 1.82 1.3782	86.02 14 2σ Confidence Limit Error Magnification	
					42%	Spreading Factor



Information on Analysis and Constants Used in Calculations

Project =
 Sample = 2021-MAC-8A
 Material = Biotite
 Location = Peru
 Region = Peru
 Analyst = Kevin Konrad
 Irradiation = UNLV-128-1
 Position = X: 0 | Y: 0 | Z/H: 40 mm
 FCT-NM Age = 28.201 ± 0.023 Ma
 FCT-NM Reference = Kuiper et al (2008)
 FCT-NM 40Ar/39Ar Ratio =
 FCT-NM J-value = 0.00171450 ± 0.00000034
 Air Shot 40Ar/36Ar = 308.3970 ± 0.5705
 Air Shot MDF = 0.99201539 ± 0.00051431 (LIN)
 Experiment Type = Sample
 Extraction Method = Furnace Heating
 Heating = 840 sec
 Isolation = 20.00 min
 Instrument = NGX
 Preferred Age = Plateau Age
 Age Classification = Crystallization Age
 IGSN = Undefined
 Rock Class = Undefined
 Lithology = Unknown
 Lat-Lon = Undefined - Undefined
 Age Equations = Min et al. (2000)
 Negative Intensities = Allowed
 Collector Calibrations = 36Ar
 Decay 40K(total) = 5.530 ± 0.048 E-10 1/a
 Decay Activity 40K(EC,β⁺) = 3.310 ± 0.040 1/gs
 Decay Activity 40K(β⁻) = 28.270 ± 0.050 1/gs
 Decay 39Ar = 2.940 ± 0.016 E-07 1/h
 Decay 37Ar = 8.230 ± 0.012 E-04 1/h
 Decay 36Cl = 2.257 ± 0.015 E-06 1/a
 Production 39/37(ca) = 0.0006858 ± 0.0000029
 Production 38/37(ca) = 0.0000247 ± 0.0000047
 Production 36/37(ca) = 0.0002643 ± 0.0000291
 Production 38/39(k) = 0.012135 ± 0.000066
 Production 36/38(c) = 262.80 ± 1.71
 Scaling Ratio K/Ca = 0.430
 Abundance Ratio 40K/K = 1.1700 ± 0.0100 E-04
 Atomic Weight K = 39.0983 ± 0.0001 g
 Trapped 40/36(a) = 298.56 ± 0.31
 Trapped 38/36(a) = 0.1885 ± 0.0003
 Standard MDF 40/36(a) = 298.56 ± 0.31
 Standard MDF Reference = Lee et al 2006

Results	40(a)/36(a) ± 2σ	40(r)/39(k) ± 2σ	Age ± 2σ (ka)	MSWD	39Ar(k) (%n)	K/Ca ± 2σ
Age Plateau		2.83469 ± 0.00872 ± 0.31%	8767.3 ± 27.1 ± 0.31%	1.22	99.23	2570 ± 2468
			Full External Error ± 147.4	23%	21	
			Analytical Error ± 26.9	1.63	2σ Confidence Limit	
				1.1046	Error Magnification	
Total Fusion Age		2.81704 ± 0.01153 ± 0.41%	8712.8 ± 35.7 ± 0.41%		23	377 ± 49
			Full External Error ± 148.4			
			Analytical Error ± 35.6			
Normal Isochron	297.29 ± 1.04 ± 0.35%	2.84018 ± 0.00925 ± 0.33%	8784.2 ± 28.8 ± 0.33%	1.03	99.23	
			Full External Error ± 148.0	42%	21	
			Analytical Error ± 28.6	1.65	2σ Confidence Limit	
				1.0144	Error Magnification	
Inverse Isochron	297.32 ± 1.03 ± 0.35%	2.84033 ± 0.00919 ± 0.32%	8784.7 ± 28.6 ± 0.33%	1.02	99.23	
			Full External Error ± 148.0	44%	21	
			Analytical Error ± 28.3	1.65	2σ Confidence Limit	
				1.0076	Error Magnification	
				80%	Spreading Factor	

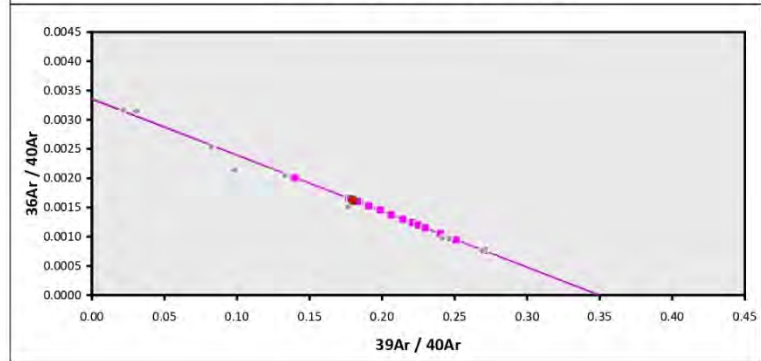
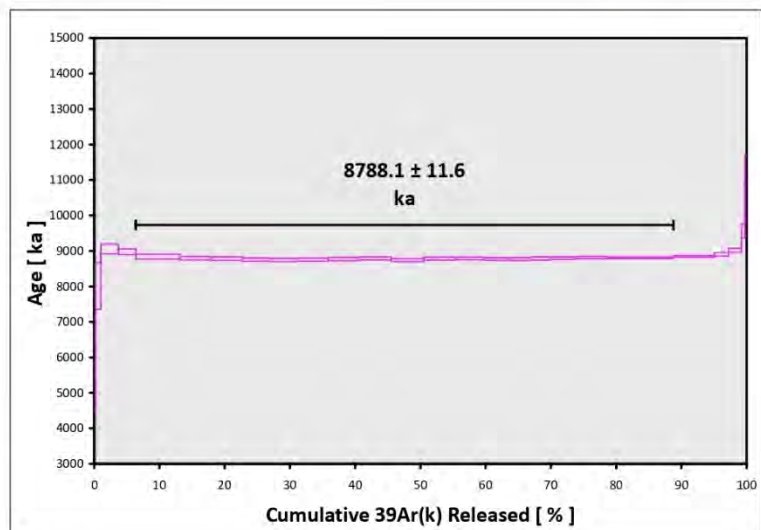


2021-MAC-11B

Information on Analysis and Constants Used in Calculations

Project =
 Sample = 2021-MAC-11B
 Material = Biotite
 Location = Peru
 Region = Peru
 Analyst = Kevin Konrad
 Irradiation = UINLV-128-1
 Position = X: 0 | Y: 0 | Z/H: 30 mm
 FCT-NM Age = 28.201 ± 0.023 Ma
 FCT-NM Reference = Kuiper et al. (2008)
 FCT-NM 40Ar/39Ar Ratio =
 FCT-NM J-value = 0.00170510 ± 0.00000034
 Air Shot 40Ar/36Ar = 307.2780 ± 0.5500
 Air Shot MDF = 0.99289791 ± 0.00050351 (LIN)
 Experiment Type = Sample
 Extraction Method = Furnace Heating
 Heating = 840 sec
 Isolation = 20.00 min
 Instrument = NGX
 Preferred Age = Undefined
 Age Classification = Undefined
 IGSN = Undefined
 Rock Class = Undefined
 Lithology = Unknown
 Lat-Lon = Undefined - Undefined
 Age Equations = Min et al. (2000)
 Negative Intensities = Allowed
 Collector Calibrations = 36Ar
 Decay 40K (total) = 5.530 ± 0.048 E-10 1/a
 Decay Activity 40K(εC,β⁺) = 3.310 ± 0.040 1/gs
 Decay Activity 40K(β⁻) = 28.270 ± 0.050 1/gs
 Decay 39Ar = 2.940 ± 0.016 E-07 1/h
 Decay 37Ar = 8.230 ± 0.012 E-04 1/h
 Decay 36Cl = 2.257 ± 0.015 E-06 1/a
 Production 39/37(ca) = 0.0006858 ± 0.0000029
 Production 38/37(ca) = 0.0000247 ± 0.0000047
 Production 36/37(ca) = 0.0002643 ± 0.0000291
 Production 38/39(k) = 0.012135 ± 0.000066
 Production 36/38(d) = 262.80 ± 1.71
 Scaling Ratio K/Ca = 0.430
 Abundance Ratio 40K/K = 1.1700 ± 0.0100 E-04
 Atomic Weight K = 39.0983 ± 0.0001 g
 Trapped 40/36(a) = 298.56 ± 0.31
 Trapped 38/36(a) = 0.1885 ± 0.0003
 Standard MDF 40/36(a) = 298.56 ± 0.31
 Standard MDF Reference = Lee et al 2006

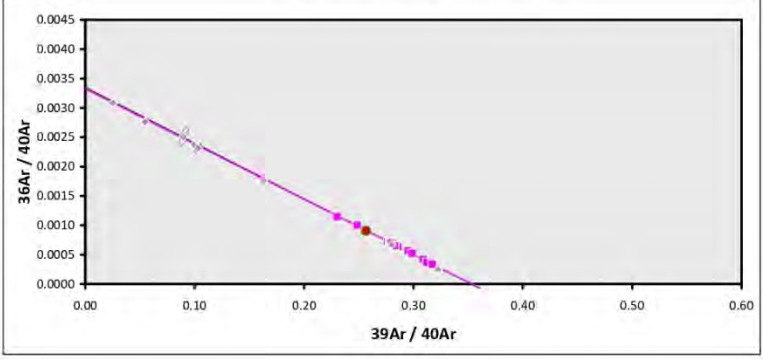
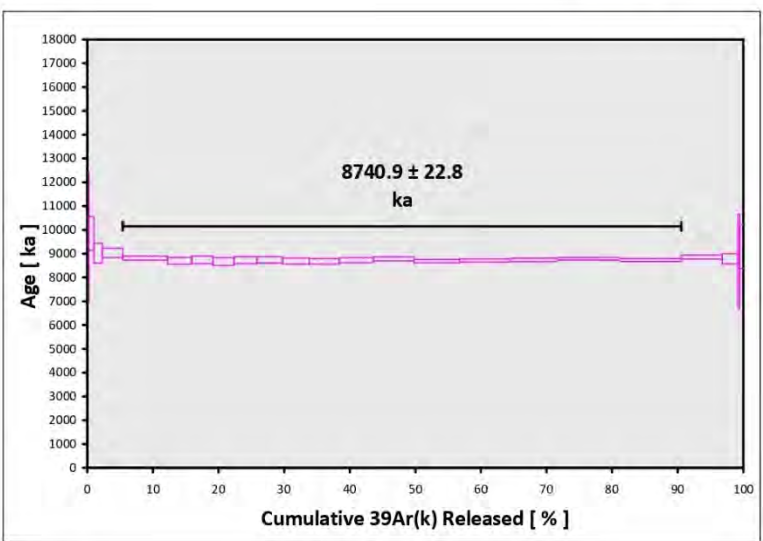
Results	40(a)/36(a) ± 2σ	40(r)/39(k) ± 2σ	Age ± 2σ (ka)	MSWD	39Ar(k) (%),n	K/Ca ± 2σ
Age Plateau		2.85710 ± 0.00362 ± 0.13%	8788.1 ± 11.6 ± 0.13% Full External Error ± 145.7 Analytical Error ± 11.1	1.50 9%	82.40 17	844 ± 114 2σ Confidence Limit Error Magnification
Total Fusion Age		2.86370 ± 0.00383 ± 0.13%	8808.3 ± 12.3 ± 0.14% Full External Error ± 146.1 Analytical Error ± 11.8		26	286 ± 4
Normal Isochron	297.18 ± 1.27 ± 0.43%	2.86508 ± 0.00814 ± 0.28%	8812.6 ± 25.2 ± 0.29% Full External Error ± 147.8 Analytical Error ± 25.0	1.38 14%	82.40 17	1.73 2σ Confidence Limit 1.1765 Error Magnification
Inverse Isochron	297.22 ± 1.27 ± 0.43%	2.86486 ± 0.00814 ± 0.28%	8811.9 ± 25.2 ± 0.29% Full External Error ± 147.8 Analytical Error ± 25.0	1.39 14%	82.40 17	1.776 Error Magnification 37% Spreading Factor



Information on Analysis and Constants Used in Calculations

Project =
 Sample = **2021-MAC-25**
 Material = **Biotite**
 Location = **Peru**
 Region = **Peru**
 Analyst = **Kevin Konrad**
 Irradiation = **UNLV-128-1**
 Position = **X: 0 | Y: 0 | Z/H: 34 mm**
 FCT-NM Age = **28.201 ± 0.023 Ma**
 FCT-NM Reference = **Kuiper et al. (2008)**
 FCT-NM 40Ar/39Ar Ratio =
 FCT-NM J-value = **0.00171010 ± 0.00000034**
 Air Shot 40Ar/36Ar = **308.2810 ± 0.5827**
 Air Shot MDF = **0.99210658 ± 0.00052298 (LIN)**
 Experiment Type = **Sample**
 Extraction Method = **Furnace Heating**
 Heating = **840 sec**
 Isolation = **20.00 min**
 Instrument = **NGX**
 Preferred Age = **Plateau Age**
 Age Classification = **Crystallization Age**
 IGSN = **Undefined**
 Rock Class = **Undefined**
 Lithology = **Undefined**
 Lat-Lon = **Undefined - Undefined**
 Age Equations = **Min et al. (2000)**
 Negative Intensities = **Allowed**
 Collector Calibrations = **36Ar**
 Decay 40K(total) = **5.530 ± 0.048 E-10 1/a**
 Decay Activity 40K(ϵ_C, β^+) = **3.310 ± 0.040 1/gs**
 Decay Activity 40K(β^-) = **28.270 ± 0.050 1/gs**
 Decay 39Ar = **2.940 ± 0.016 E-07 1/h**
 Decay 37Ar = **8.230 ± 0.012 E-04 1/h**
 Decay 36Cl = **2.257 ± 0.015 E-06 1/a**
 Production 39/37(ca) = **0.0006858 ± 0.0000029**
 Production 38/37(ca) = **0.0000247 ± 0.0000047**
 Production 36/37(ca) = **0.0002643 ± 0.0000291**
 Production 38/39(k) = **0.012135 ± 0.000066**
 Production 36/38(cl) = **262.80 ± 1.71**
 Scaling Ratio K/Ca = **0.430**
 Abundance Ratio 40K/K = **1.1700 ± 0.0100 E-04**
 Atomic Weight K = **39.0983 ± 0.0001 g**
 Trapped 40/36(a) = **298.56 ± 0.31**
 Trapped 38/36(a) = **0.1885 ± 0.0003**
 Standard MDF 40/36(a) = **298.56 ± 0.31**
 Standard MDF Reference = **Lee et al 2006**

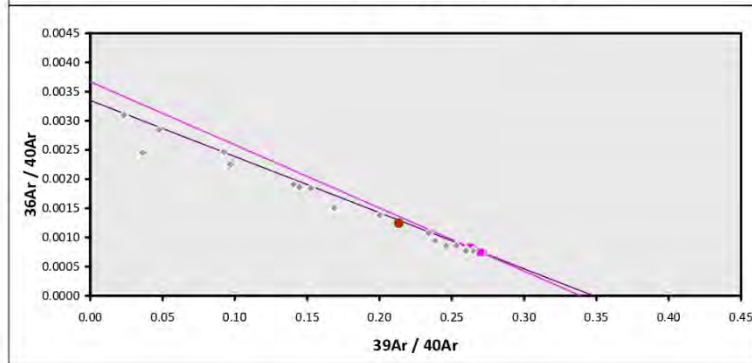
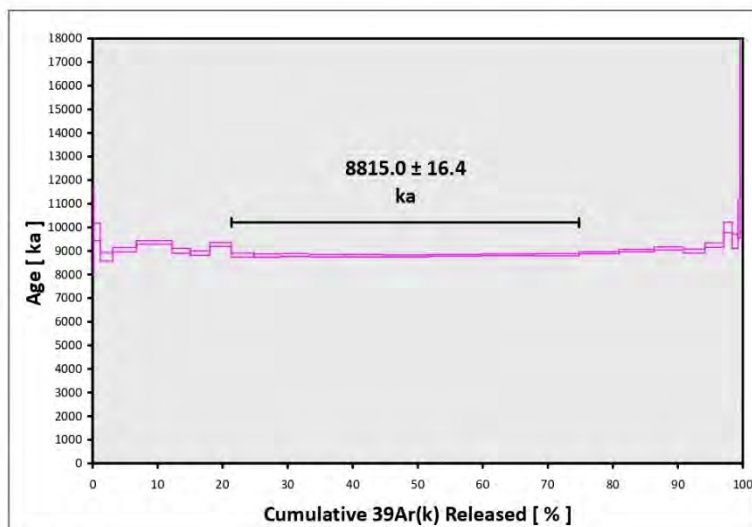
Results	40(a)/36(a) ± 2σ	40(r)/39(k) ± 2σ	Age ± 2σ (ka)	MSWD	39Ar(k) (%n)	K/Ca ± 2σ
Age Plateau		2.83342 ± 0.00733 ± 0.26%	8740.9 ± 22.8 Full External Error ± 146.3 Analytical Error ± 22.6	0.92 53%	85.14 15	347 ± 337 2σ Confidence Limit Error Magnification
Total Fusion Age		2.84304 ± 0.00835 ± 0.29%	8770.5 ± 25.9 Full External Error ± 147.3 Analytical Error ± 25.7		23	214 ± 25
Normal Isochron	300.72 ± 6.70 ± 2.23%	2.82878 ± 0.01567 ± 0.55%	8726.6 ± 48.4 Full External Error ± 152.1 Analytical Error ± 48.2	0.96 49%	85.14 15	1.78 2σ Confidence Limit Error Magnification
Inverse Isochron	300.87 ± 6.67 ± 2.22%	2.82878 ± 0.01559 ± 0.55%	8726.6 ± 48.1 Full External Error ± 152.1 Analytical Error ± 48.0	0.96 49%	85.14 15	1.78 2σ Confidence Limit Error Magnification 25% Spreading Factor



Information on Analysis and Constants Used in Calculations

Project =
 Sample = **2021-MAC-31**
 Material = **Biotite**
 Location = **Peru**
 Region = **Peru**
 Analyst = **Kevin Konrad**
 Irradiation = **UNLV-128-1**
 Position = X: 0 | Y: 0 | Z/H: 27 mm
 FCT-NM Age = **28.201 ± 0.023 Ma**
 FCT-NM Reference = **Kuiper et al. (2008)**
 FCT-NM 40Ar/39Ar Ratio =
 FCT-NM J-value = **0.00170030 ± 0.00000034**
 Air Shot 40Ar/36Ar = **307.0500 ± 0.5097**
 Air Shot MDF = **0.99307851 ± 0.00047679 (LIN)**
 Experiment Type = **Sample**
 Extraction Method = **Undefined**
 Heating = **840 sec**
 Isolation = **20.00 min**
 Instrument = **NGX**
 Preferred Age = **Undefined**
 Age Classification = **Undefined**
 IGSN = **Undefined**
 Rock Class = **Undefined**
 Lithology = **Undefined**
 Lat-Lon = **Undefined - Undefined**
 Age Equations = **Min et al. (2000)**
 Negative Intensities = **Allowed**
 Collector Calibrations = **36Ar**
 Decay 40K(total) = **5.530 ± 0.048 E-10 1/a**
 Decay Activity 40K(EC,β⁺) = **3.310 ± 0.040 1/gs**
 Decay Activity 40K(β⁻) = **28.270 ± 0.050 1/gs**
 Decay 39Ar = **2.940 ± 0.016 E-07 1/h**
 Decay 37Ar = **8.230 ± 0.012 E-04 1/h**
 Decay 36Cl = **2.257 ± 0.015 E-06 1/a**
 Production 39/37(ca) = **0.0006858 ± 0.0000029**
 Production 38/37(ca) = **0.0000247 ± 0.0000047**
 Production 36/37(ca) = **0.0002643 ± 0.0000291**
 Production 38/39(k) = **0.012135 ± 0.000066**
 Production 36/38(c) = **262.80 ± 1.71**
 Scaling Ratio K/Ca = **0.430**
 Abundance Ratio 40K/K = **1.1700 ± 0.0100 E-04**
 Atomic Weight K = **39.0983 ± 0.0001 g**
 Trapped 40/36(a) = **298.56 ± 0.31**
 Trapped 38/36(a) = **0.1885 ± 0.0003**
 Standard MDF 40/36(a) = **298.56 ± 0.31**
 Standard MDF Reference = **Lee et al 2006**

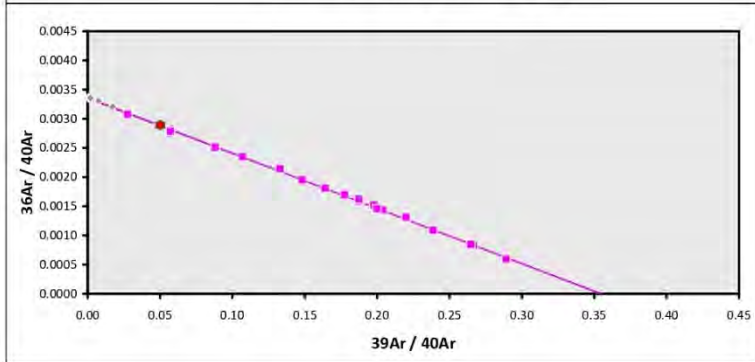
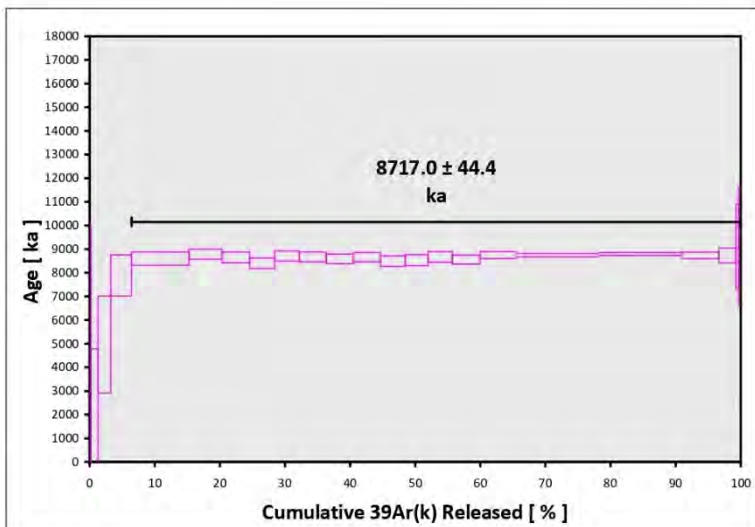
Results	40(a)/36(a) ± 2σ	40(r)/39(k) ± 2σ	Age ± 2σ (ka)	MSWD	39Ar(k) (%n)	K/Ca ± 2σ
Age Plateau		2.87396 ± 0.00522 ± 0.18%	8815.0 ± 16.4 ± 0.19% Full External Error ± 146.6 Analytical Error ± 16.0	0.65 74%	53.46 9	1745 ± 378
Total Fusion Age		2.94072 ± 0.00505 ± 0.17%	9019.3 ± 15.9 ± 0.18% Full External Error ± 149.9 Analytical Error ± 15.4		26	329 ± 6
Normal Isochron <i>Overestimated</i>	272.77 ± 27.50 ± 10.08%	2.94885 ± 0.08000 ± 2.71%	9044.1 ± 244.8 ± 2.71% Full External Error ± 286.8 Analytical Error ± 244.7	0.30 96%	53.46 9	2.07 2σ Confidence Limit 1.0000 Error Magnification
Inverse Isochron <i>Overestimated</i>	272.63 ± 27.48 ± 10.08%	2.94925 ± 0.07984 ± 2.71%	9045.3 ± 244.3 ± 2.70% Full External Error ± 286.4 Analytical Error ± 244.3	0.30 96%	53.46 9	2.07 2σ Confidence Limit 1.0000 Error Magnification 3% Spreading Factor



Information on Analysis and Constants Used in Calculations

Project =
 Sample = 2021-MAC-38
 Material = Biotite
 Location = Peru
 Region = Peru
 Analyst = Kevin Konrad
 Irradiation = UNLV-128-1
 Position = X: 0 | Y: 0 | Z/H: 43 mm
 FCT-NM Age = 28.201 ± 0.023 Ma
 FCT-NM Reference = Kuiper et al. (2008)
 FCT-NM 40Ar/39Ar Ratio =
 FCT-NM J-value = 0.00171530 ± 0.00000034
 Air Shot 40Ar/36Ar = 308.2400 ± 0.5733
 Air Shot MDF = 0.99213883 ± 0.00051669 (LIN)
 Experiment Type = Sample
 Extraction Method = Furnace Heating
 Heating = 840 sec
 Isolation = 20.00 min
 Instrument = NGX
 Preferred Age = Plateau Age
 Age Classification = Crystallization Age
 IGSN = Undefined
 Rock Class = Undefined
 Lithology = Unknown
 Lat-Lon = Undefined - Undefined
 Age Equations = Min et al. (2000)
 Negative Intensities = Allowed
 Collector Calibrations = 36Ar
 Decay 40K(total) = 5.530 ± 0.048 E-10 1/a
 Decay Activity 40K(EC,β⁺) = 3.310 ± 0.040 1/g^s
 Decay Activity 40K(β⁻) = 28.270 ± 0.050 1/g^s
 Decay 39Ar = 2.940 ± 0.016 E-07 1/h
 Decay 37Ar = 8.290 ± 0.012 E-04 1/h
 Decay 36Cl = 2.257 ± 0.015 E-06 1/a
 Production 39/37(ca) = 0.0006858 ± 0.0000029
 Production 38/37(ca) = 0.0000247 ± 0.0000047
 Production 36/37(ca) = 0.0002643 ± 0.0000291
 Production 38/39(k) = 0.012135 ± 0.000066
 Production 36/38(c1) = 262.80 ± 1.71
 Scaling Ratio K/Ca = 0.430
 Abundance Ratio 40K/K = 1.1700 ± 0.0100 E-04
 Atomic Weight K = 39.0983 ± 0.0001 g
 Trapped 40/36(a) = 298.56 ± 0.31
 Trapped 38/36(a) = 0.1885 ± 0.0003
 Standard MDF 40/36(a) = 298.56 ± 0.31
 Standard MDF Reference = Lee et al 2006

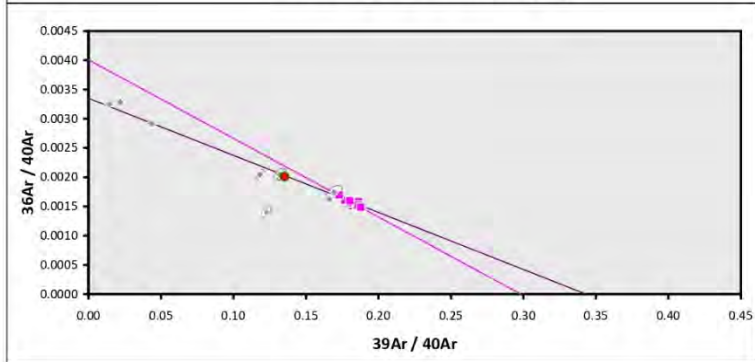
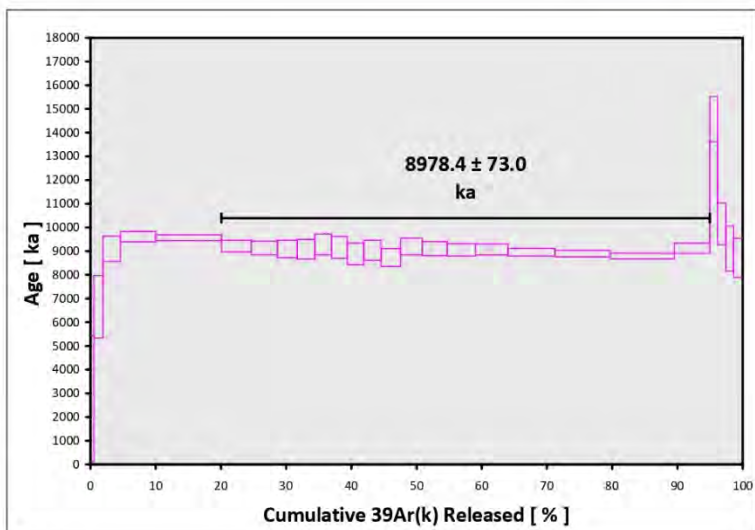
Results	40(a)/36(a) ± 2σ	40(r)/39(k) ± 2σ	Age ± 2σ (ka)	MSWD	39Ar(k) (%n)	K/Ca ± 2σ
Age Plateau		2.81709 ± 0.01435 ± 0.51%	8717.0 ± 44.4 ± 0.51%	1.58	93.55	395 ± 182
			Full External Error ± 150.8	6%	19	2σ Confidence Limit
			Analytical Error ± 44.3	1.2580		Error Magnification
Total Fusion Age		2.71630 ± 0.03822 ± 1.41%	8405.9 ± 118.1 ± 1.40%		23	208 ± 17
			Full External Error ± 182.3			
			Analytical Error ± 118.0			
Normal Isochron	297.35 ± 1.45 ± 0.49%	2.82488 ± 0.01712 ± 0.61%	8741.1 ± 59.0 ± 0.61%	1.48	93.55	
			Full External Error ± 153.9	9%	19	2σ Confidence Limit
			Analytical Error ± 52.9	1.1257		Error Magnification
Inverse Isochron	297.37 ± 1.44 ± 0.48%	2.82545 ± 0.01688 ± 0.60%	8742.8 ± 52.2 ± 0.60%	1.45	93.55	
			Full External Error ± 153.7	10%	19	2σ Confidence Limit
			Analytical Error ± 52.1	1.2057		Error Magnification
				74%		Spreading Factor



Information on Analysis and Constants Used in Calculations

Project =
 Sample = 2021-MAC-48
 Material = Biotite
 Location = Peru
 Region = Peru
 Analyst = Kevin Konrad
 Irradiation = UNLV-128-1
 Position = X: 0 | Y: 0 | Z/H: 32 mm
 FCT-NM Age = 28.201 ± 0.023 Ma
 FCT-NM Reference = Kuiper et al. (2008)
 FCT-NM 40Ar/39Ar Ratio =
 FCT-NM J-value = 0.00170780 ± 0.00000034
 Air Shot 40Ar/36Ar = 308.1790 ± 0.5701
 Air Shot MDF = 0.99218682 ± 0.00051468 (LIN)
 Experiment Type = Sample
 Extraction Method = Furnace Heating
 Heating = 840 sec
 Isolation = 20.00 min
 Instrument = NGX
 Preferred Age = Plateau Age
 Age Classification = Crystallization Age
 IGSN = Undefined
 Rock Class = Undefined
 Lithology = Unknown
 Lat-Lon = Undefined - Undefined
 Age Equations = Min et al. (2000)
 Negative Intensities = Allowed
 Collector Calibrations = 36Ar
 Decay 40K(total) = 5.530 ± 0.048 E-10 1/a
 Decay Activity 40K(EC,β⁺) = 3.310 ± 0.040 1/g
 Decay Activity 40K(β⁻) = 28.270 ± 0.050 1/g
 Decay 39Ar = 2.940 ± 0.016 E-07 1/h
 Decay 37Ar = 8.230 ± 0.012 E-04 1/h
 Decay 36Cl = 2.257 ± 0.015 E-06 1/a
 Production 39/37(ca) = 0.0006858 ± 0.00000029
 Production 38/37(ca) = 0.0000247 ± 0.00000047
 Production 36/37(ca) = 0.0002643 ± 0.00000291
 Production 38/39(k) = 0.012135 ± 0.000066
 Production 36/38(cl) = 262.80 ± 1.71
 Scaling Ratio K/Ca = 0.430
 Abundance Ratio 40K/K = 1.1700 ± 0.0100 E-04
 Atomic Weight K = 39.0983 ± 0.0001 g
 Trapped 40/36(a) = 298.56 ± 0.31
 Trapped 38/36(a) = 0.1885 ± 0.0003
 Standard MDF 40/36(a) = 298.56 ± 0.31
 Standard MDF Reference = Lee et al 2006

Results	40(a)/36(a) ± 2σ	40(r)/39(k) ± 2σ	Age ± 2σ (ka)	MSWD	39Ar(k) (%n)	K/Ca ± 2σ
Age Plateau		2.91453 ± 0.02374 ± 0.81%	8978.4 ± 73.0 ± 0.81%	1.60	74.88	557 ± 152
			Full External Error ± 165.4	6%	17	2σ Confidence Limit
			Analytical Error ± 72.9	1.2638		Error Magnification
Total Fusion Age		2.95992 ± 0.01995 ± 0.67%	9117.9 ± 61.4 ± 0.67%		26	233 ± 37
			Full External Error ± 162.7			
			Analytical Error ± 61.3			
Normal Isochron	249.85 ± 22.35 ± 8.94%	3.35033 ± 0.20113 ± 6.00%	10317.2 ± 617.6 ± 5.99%	0.64	74.88	
			Full External Error ± 640.7	84%	17	2σ Confidence Limit
			Analytical Error ± 617.6	1.0000		Error Magnification
Inverse Isochron	249.57 ± 22.28 ± 8.93%	3.35346 ± 0.19926 ± 5.94%	10326.8 ± 611.9 ± 5.93%	0.63	74.88	
			Full External Error ± 635.2	85%	17	2σ Confidence Limit
			Analytical Error ± 611.9	1.0000		Error Magnification
				6%		Spreading Factor



Information on Analysis and Constants Used in Calculations

Project =
 Sample = **2021-MAC-67**
 Material = **Biotite**
 Location = **Peru**
 Region = **Peru**
 Analyst = **Kevin Konrad**
 Irradiation = **UNLV-128-1**
 Position = **X: 0 | Y: 0 | Z/H: 20 mm**
 FCT-NM Age = **28.201 ± 0.023 Ma**
 FCT-NM Reference = **Kuiper et al. (2008)**
 FCT-NM 40Ar/39Ar Ratio =
 FCT-NM J-value = **0.00168530 ± 0.00000034**
 Air Shot 40Ar/36Ar = **307.2520 ± 0.4486**
 Air Shot MDF = **0.99291849 ± 0.00043602 (LIN)**
 Experiment Type = **Sample**
 Extraction Method = **Furnace Heating**
 Heating = **840 sec**
 Isolation = **20.00 min**
 Instrument = **NGX**
 Preferred Age = **No Age**
 Age Classification = **Undefined**
 IGSN = **Undefined**
 Rock Class = **Undefined**
 Lithology = **Unknown**
 Lat-Lon = **Undefined - Undefined**
 Age Equations = **Min et al. (2000)**
 Negative Intensities = **Allowed**
 Collector Calibrations = **36Ar**
 Decay 40K(total) = **5.530 ± 0.048 E-10 1/a**
 Decay Activity 40K(ε,β⁻) = **3.310 ± 0.040 1/gs**
 Decay Activity 40K(β⁻) = **28.270 ± 0.050 1/gs**
 Decay 39Ar = **2.940 ± 0.016 E-07 1/h**
 Decay 37Ar = **8.230 ± 0.012 E-04 1/h**
 Decay 36Cl = **2.257 ± 0.015 E-06 1/a**
 Production 39/37(ca) = **0.0006858 ± 0.0000029**
 Production 38/37(ca) = **0.0000247 ± 0.0000047**
 Production 36/37(ca) = **0.0002643 ± 0.0000291**
 Production 38/39(k) = **0.012135 ± 0.000066**
 Production 36/38(c) = **262.80 ± 1.71**
 Scaling Ratio K/Ca = **0.430**
 Abundance Ratio 40K/K = **1.1700 ± 0.0100 E-04**
 Atomic Weight K = **39.0983 ± 0.0001 g**
 Trapped 40/36(a) = **298.56 ± 0.31**
 Trapped 38/36(a) = **0.1885 ± 0.0003**
 Standard MDF 40/36(a) = **298.56 ± 0.31**
 Standard MDF Reference = **Lee et al 2006**

Results	40(a)/36(a) ± 2σ	40(r)/39(k) ± 2σ	Age ± 2σ (Ma)	MSWD	39Ar(k) (%n)	K/Ca ± 2σ
---------	------------------	------------------	---------------	------	--------------	-----------

Age Plateau	Cannot Calculate					
Total Fusion Age		2.02352 ± 0.01040 ± 0.51%	6.16 ± 0.03 ± 0.51%		26	144 ± 6
			Full External Error ± 0.11			
			Analytical Error ± 0.03			
Normal Isochron	Cannot Calculate					
Inverse Isochron	Cannot Calculate					

